Development of high surface area attrition-resistant spray-dried iron catalysts for Fischer-Tropsch Synthesis

AMANDA SAMORA BUTHELEZI

21707285

SUBMITTED IN FULFILMENT OF THE REQUIREMENTS OF THE DEGREE OF MASTER OF APPLIED SCIENCE IN CHEMISTRY IN THE FACULTY OF APPLIED SCIENCES AT THE DURBAN UNIVERSITY OF TECHNOLOGY

December 2024

DECLARATION

I declare in this thesis, that all the work was done by myself, working under the supervision of Dr P. Ntola, Professor H. J. Herees and Dr C. L. Tucker. This thesis is being submitted for the degree of Master of Applied Science in Chemistry at Durban University of Technology. It has not been submitted before for any other degree.

Student Name: Amanda Samora Buthelezi

Signature Date: 21/05/2025

Supervisor Name: Dr P. Ntola

Signature: Date: 21/05/2025

Co-Supervisor Name: Prof. H. J. Herees

Signature Date: 21/05/2025

Co-Supervisor Name: Dr C. L. Tucker

Signature Date: 21/05/2025

DEDICATION

This research work is dedicated to the Almighty God. I dedicate this work to my family and everyone who assisted me.

ACKNOWLEDGEMENTS

I would like to thank the Lord God Almighty for giving me the strength and wisdom to conduct this research work. Special thanks to Henk van de Bovenkamp for supervising me in the laboratory and for his assistance in conducting the research while at the University of Groningen, in the Netherlands. He taught me to become an independent researcher by learning how to design and operate the reactor by myself. Special thanks go to my supervisor, Dr. P. Ntola for the assistance, support, and guidance since the beginning of this research. I was motivated to be under her supervision, and it made me realize that I could do more by putting effort into research, and that built my confidence. I would like to give special thanks to my co-supervisors, Dr. C.L. Tucker, and Prof. H. J. Herees, for their support and guidance in doing this research. I have learned from them that research is doable through reading, especially finding relevant information from literature that is related to my research topic. Special thanks to the library staff from DUT for teaching me about literature search, including different research tools and how to find relevant information using library resources.

I would like to thank the University of KwaZulu Natal (UKZN) for access to characterization instruments. Special thanks go to Prof M. L. Shozi for his assistance and contribution in characterizing samples. Furthermore, I would like to thank the University of Groningen, Netherlands, for giving me the opportunity to conduct research in the laboratory and my home institution, DUT. I would also like to give thanks to the funding received from the Study Fund for the South African student scholarship. Special thanks to the UTT Bursary for funding support.

PUBLICATION CONTRIBUTIONS

1. **Amanda S.** Buthelezi, Chelsea L. Tucker, Hero J. Herees, Mzamo L. Shozi, Hendrik H. van de Bovenkamp and Pinkie Ntola, Fischer-Tropsch Synthesis using promoted, unsupported, supported, bimetallic and spray-dried iron catalysts: A review. *Results in Chemistry*, (2024), 101623.

CONFERENCE CONTRIBUTIONS

Poster Presentations

Amanda S. Buthelezi, Chelsea L. Tucker, Hero J. Herees, Mzamo L. Shozi, Hendrik H. van de Bovenkamp and Pinkie Ntola, Development of high surface area attrition-resistant spray-dried iron catalysts for Fischer-Tropsch Synthesis, SACI-KZN Postgraduate Colloquium 2023, University of KwaZulu Natal, Durban, South Africa.

Amanda S. Buthelezi, Chelsea L. Tucker, Hero J. Herees, Hendrik H. van de Bovenkamp and Pinkie Ntola, Spray-dried attrition-resistant iron-based catalysts for advancing Fischer-Tropsch Synthesis, CATSA 2024, Champagne sports resort, Drakensberg, KwaZulu Natal, South Africa.

Oral Presentations

Amanda S. Buthelezi, Chelsea L. Tucker, Hero J. Herees, Hendrik H. van de Bovenkamp and Pinkie Ntola, Development of High surface area attrition-resistant spray-dried iron catalysts for Fischer-Tropsch Synthesis, Applied Science Faculty Research Day 2023, Musgrave Hotel, Durban, South Africa.

Amanda S. Buthelezi, Chelsea L. Tucker, Hero J. Herees, Hendrik H. van de Bovenkamp and Pinkie Ntola, Iron-based, spray-dried and attrition resistant iron catalysts for Fischer-Tropsch Synthesis, SACI-KZN Postgraduate Colloquium 2024, University of Zululand, KwaDlangezwa Campus, Empangeni, South Africa.

.

LIST OF ABBREVIATIONS

ASF: Anderson-Schulz-Flory

ASTM: American Society for Testing and Materials

BET: Brunauer-Emmet-Teller

CO: Carbon monoxide

CO_2: Carbon dioxide

EDX: Energy-dispersive X-ray

FBR: Fixed Bed Reactor

FFB: Fluidized Bed Reactor

FID: Flame Ionization Detector

F-TS: Fischer-Tropsch Synthesis

FTY: Fischer-Tropsch Activity

GC: Gas Chromatography

GHSV: Gas Hourly Space Velocity

GTL: Gas to Liquid Technology

H_2: hydrogen

H_2O: Water

HTFS: High Temperature Fischer-Tropsch Synthesis

LTFS: Low Temperature Fischer-Tropsch Synthesis

Rxn: Reaction

SBR: Slurry Bed Reactor

SEM: Scanning Electron Microscopy

STP: Standard Temperature and Pressure

TCD: Thermal Conductivity Detector

TEM: Transmission Electron Microscopy

WGS: Water-gas-shift

WHSV: Weight Hourly Space velocity

Wt%: Weight percent

XRD: X-ray Diffraction

Greek Letters

@:at

α: alpha

ABSTRACT

Iron is used as catalyst in the industrial process Fischer-Tropsch Synthesis (F-TS), which is a catalytic chemical reaction that transforms synthesis gas ($CO + H_2$) to create paraffins and olefins for fuels and chemicals. This study aimed to design iron catalysts with a high surface area and attrition resistance for F-TS. The following catalysts: α-Fe_2O_3, K/Cu/Fe and 0.367 M K/Cu/Fe spray-dried at 200 °C were prepared using the co-precipitation, impregnation and spray-drying methods. The catalysts were then characterized using various characterization techniques including thermogravimetric analysis (TGA), Brunauer-Emmett-Teller (BET) analysis, scanning electron microscopy (SEM), X-ray diffraction (XRD), and X-ray fluorescence (XRF). Attrition resistance comprised physical tests with the accredited standard method of testing materials (ASTM). The results showed that the 0.367 M K/Cu/Fe spray-dried at 200 °C catalyst has a large surface area of 39 m^2/g and this could be attributed to the small particle size and the catalyst being obtained in a powder form. The α- Fe_2O_3 catalyst was found to have more physical attrition resistance with a value of 2.2 wt%/h. This was attributed to the small fines produced during the physical attrition test, meaning that the catalyst has a high mechanical strength as compared to other catalysts. The α-Fe_2O_3 catalyst was also found to have more chemical attrition resistance. This was attributed to the minimum phase change that occurred during the reduction or activation with CO as compared to other catalysts. All the catalysts including α-Fe_2O_3, K/Cu/Fe and 0.367 M K/Cu/Fe spray-dried at 200 °C demonstrated good selectivity characteristics (low methane and high C_{5+}) hydrocarbons. This was ascribed to the iron carbide (χ-Fe_5C_2) active phase or site, which increased the chain growth and favoured the production of C_{5+} hydrocarbons while decreasing methane selectivity. The α-Fe_2O_3 catalyst showed high activity and stability, as there was minimal loss of catalytic activity as compared to other catalysts. This was as a result of less CO_2 selectivity produced by the catalyst, meaning that there was low water-gas shift activity (WGS) and the active sites were less affected by the presence of water, which causes high loss of catalytic activity. The activity and selectivity of the catalysts need to be improved before the industrial application.

TABLE OF CONTENTS

LIST OF TABLES

LIST OF FIGURES

CHAPTER 1: INTRODUCTION

1.1 Introduction and Background

Public awareness of sustainability, carbon neutrality, and the circular economy has reached an all-time high throughout the past ten years. Due to increased awareness, market dynamics have shifted in favour of more environmentally friendly items, and there is currently a need for plastic products created from waste materials by advanced mechanical or complex recycling. This pushes the chemical sector to use pyrolysis and gasification to create solutions for monomers derived from waste plastics (Buthelezi et al., 2024). One technique for creating monomers is the F-TS. F-TS is a catalyzed chemical reaction that generates hydrocarbons for chemicals and fuels (Gholami et al., 2021). During fuel research at the Kaiser Wilhelm Institute for coal research laboratories in the 1920s, German scientists Franz Fischer and Hans Tropsch produced the first discovery of the Fischer-Tropsch Synthesis (Fischer and Tropsch, 1922). Hans Fischer and Franz Tropsch implemented this process to create gasoline during World War II. They tried to increase the hydrocarbon supply in the following years. The development of F-TS has received considerable attention due to the abundance of natural gas, environmental regulations that limit the manufacture of fuels made from carbon dioxide, and the advancement of F-TS capabilities in catalyst synthesis to make liquid fuels. Four active metals are used as catalysts in the F-TS: iron (Fe), cobalt (Co), nickel (Ni), and ruthenium (Ru). While Ru and Ni exhibit significant activity for F-TS, they are often not suitable as catalysts for use in commercial processes due to several drawbacks, including their high methane selectivity and restricted availability, respectively. For industrial purposes, iron and cobalt catalysts are mostly used.

Utilizing cobalt as a catalyst at low temperatures, Ruchrchemie AG set up the first industrial F-TS plant in 1936 at Obserhausen, Germany (Yanga et al., 2014). In the 1950s, Sasol built the next generation of iron-based catalysts focused on F-T plants in South Africa (Gholami et al., 2021). Over the past century, many industrial enterprises have actively participated in this prospective energy industry, including Shell, Statoil, BP, ExxonMobil, PetroSA, Ras Laffan Qatar, Velocys, and Rentech (Loseva et al., 2019).

1.2 Problem statement

Currently, Sasol in South Africa uses a slurry bubble column reactor (SBCR) to produce fuel and gasoline through the F-TS process. However, the synthesis of convenient iron catalysts for use in SBCR is still a challenge. Various studies have been published in this regard, however, there has been minimum progress (Teimouri et al., 2021; Lin et al., 2021). The challenge is that iron catalysts are affected by attrition, which then results in catalyst particles with sizes ranging from 30 to 90 μm becoming stuck in a SBCR. This decreases their performance in F-TS. Furthermore, after the F-TS reaction is complete the catalyst must be recovered, and Sasol requires stable, highly attrition resistant iron catalyst to achieve this. This study was motivated by the need to improve iron catalysts attrition resistance. The F-TS process involves several steps prior to the creation of value-added products such as gasoline and diesel fractions.

1.3 The Fischer-Tropsch Synthesis process

The entire F-TS process including the feed stock, natural gas and coal is shown in Figure 1.1. The syngas is generated in the first step from coal or natural gas. In step 2, the syngas is cleaned. In step 3, different hydrocarbons are produced by the F-TS in a reaction between purified syngas and the catalyst. Other products such as diesel, pentene/hexene, naphtha, and wax are produced from the hydrocarbons generated in step 3.

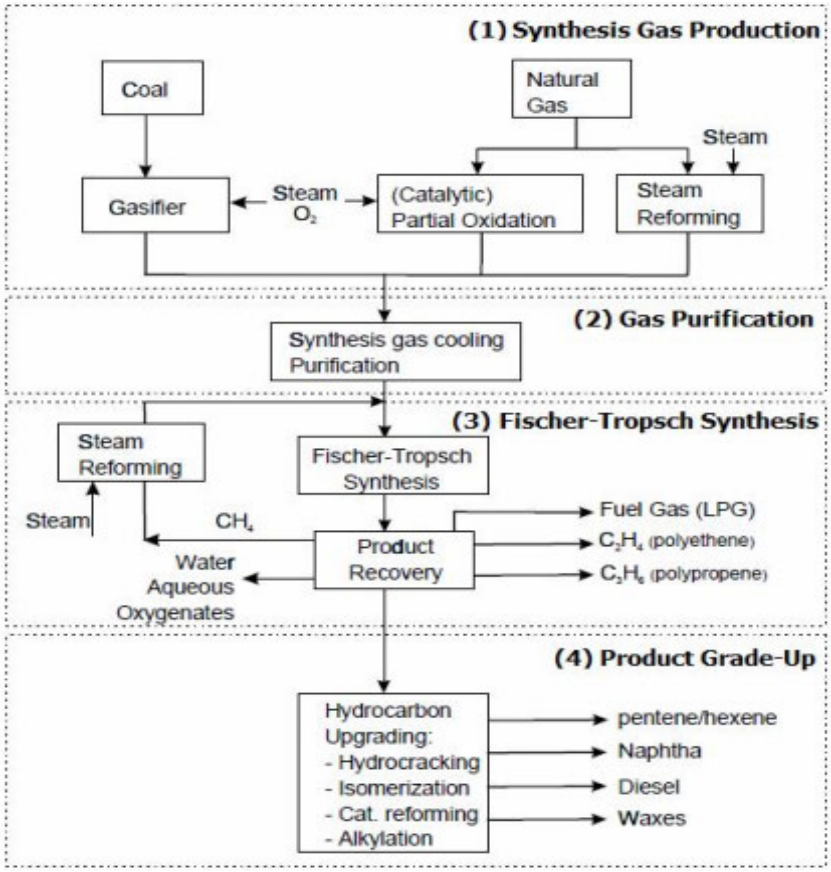

Figure 1.1: The F-TS entire process, reprinted with permission from (Arsalanfara et al., 2014)

Gas-to-liquid, coal-to-liquid, and biomass-to-liquid technologies are amongst the advancements in F-TS feedstock that have been made thus far. Research on F-TS typically focuses on either reactor design, F-TS feedstock technology advancement, or catalytic properties improvement (Cheng et al., 2017). This study focused on improving catalytic properties by enhancing the physiochemical, mechanical (strength and attrition), and catalytic properties of iron catalysts using spray-drying technology, the co-precipitation and impregnation synthesis methods.

1.4 Spray-drying technology

Using a gaseous hot drying medium, the spray-dying process turns liquid material or a slurry solution into dried particles (Santos et al., 2018). Before the fine powder is created, three steps must be completed including atomization, drying, and separation. Figure 1.2 illustrates how hot gas atomizes the slurry solution before it falls as droplets into the drying chamber, where it is transformed into granules and get separated from the cyclone and fine powder get collected in the

last step. Detailed information including the spray-drying operational factors influencing the morphology of spray-dried products is explained in Chapter Two.

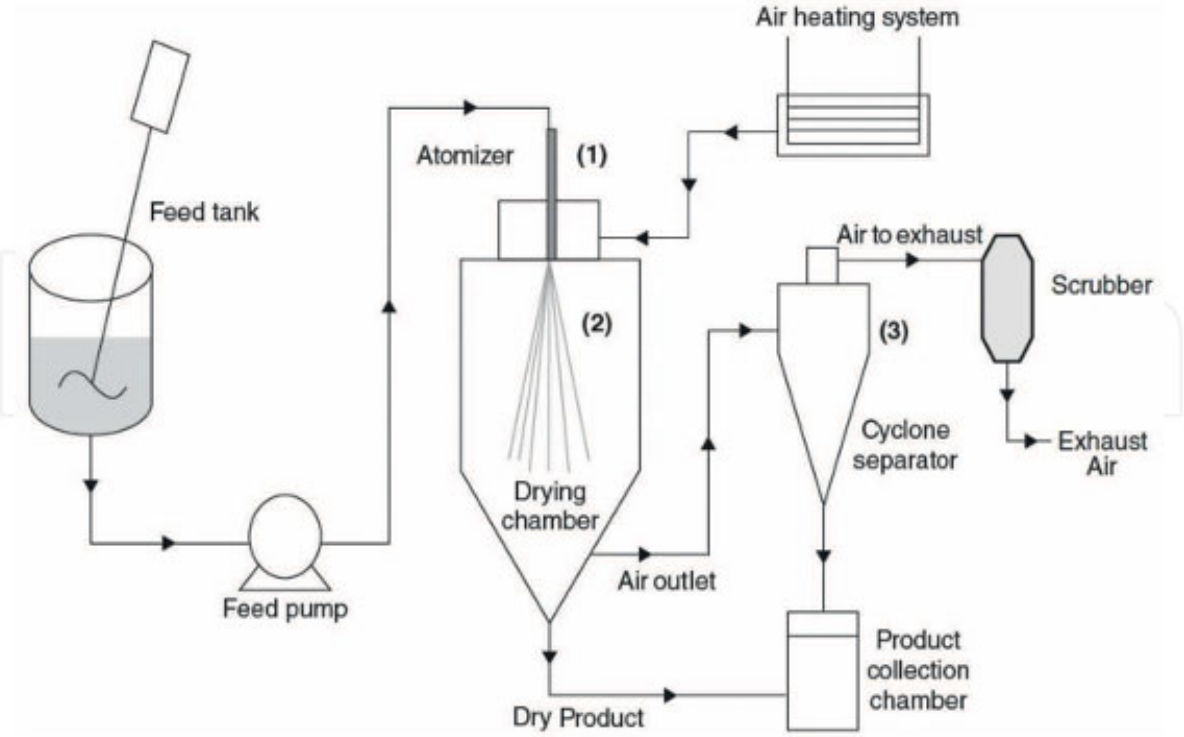

Figure 1.2: Spray-drying method, reprinted with permission from (Santos et al., 2018)

1.5 Co-precipitation synthesis method

The co-precipitation synthesis method is the most common method used to prepare nanoparticles. The catalyst is prepared by mixing salts of metal precipitates in hydroxide form in the presence of water. The diagram in Figure 1.3 shows all the steps involved in the preparation of iron catalysts using the precipitation method. The challenge with the catalysts prepared by this method is that they are easily affected by attrition, which causes a loss of catalyst activity and performance in F-TS (Bajaj and Joshi, 2021).

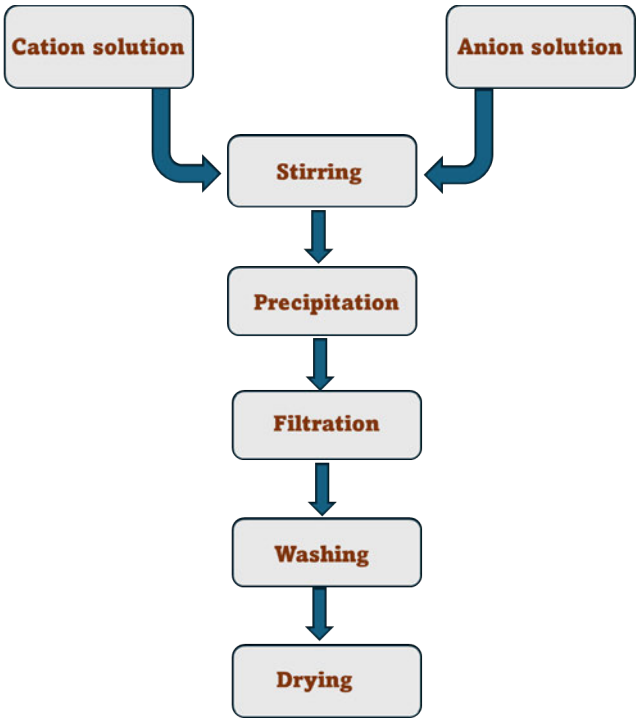

Figure 1.3: The flow chart for the co-precipitation method

1.6 Attrition of catalysts

According to Amblard et al. (2015), attrition is the process by which fragments of fine particles are created from solid pieces as they strike the reactor walls after being under pressure. Attrition causes challenges in the advancement of convenient F-TS reactors. The loss of catalytic activity, difficulties in the separation of the final products with a catalyst, and changes in the characteristics of the bulk are examples of problems associated with the attrition of catalysts. Catalysts can either undergo physical or chemical attrition (Kukade et al., 2016).

1.6.1 Physical Attrition of catalysts

The collisions occurring between catalyst particles and the wall of the reactor are called physical attrition. The larger catalyst particles can collapse into smaller particles when a certain pressure is applied. The process by which more fines are produced while the size of the particles moves to a smaller distribution is referred to as abrasion (Chang et al., 2022).

1.6.2 Chemical Attrition of catalysts

When phase transition occurs, it results in the cracking of the particles of the catalyst, which is caused by inherent stress. The catalyst breaks up to produce small fines (nanometer range) when chemical attrition occurs (Kukade et al., 2016). The phase transition of iron occurs as follows: $Fe_2O_3 \rightarrow Fe_3O_4 \rightarrow FeO \rightarrow Fe$.

1.6.3 Measuring attrition of catalysts

The solids that break are calculated by gathering the size of the particles. The catalyst breakup can be enhanced in a test in which samples collide on a hard surface (Kukade et al., 2016). The fluidized ASTM and jet cup methods are mostly utilized to perform attrition resistance measurements. The amount of catalysts is measured and transferred into the attrition tube, and the catalysts are subjected to a certain pressure. After some hours, the fines are collected and measured. The initial mass of the catalyst weighed, the mass of the fines collected, and the time taken to complete the test are used to calculate the rate of attrition towards that sample or catalyst. A higher rate of attrition means that the catalyst has less attrition resistance. On the other hand, a lower rate of attrition means the catalyst is more attrition-resistant (Lin et al., 2021). Figure 1.4 shows the two commonly used attrition test methods, the Jet Cup (A) and ASTM (B) test methods.

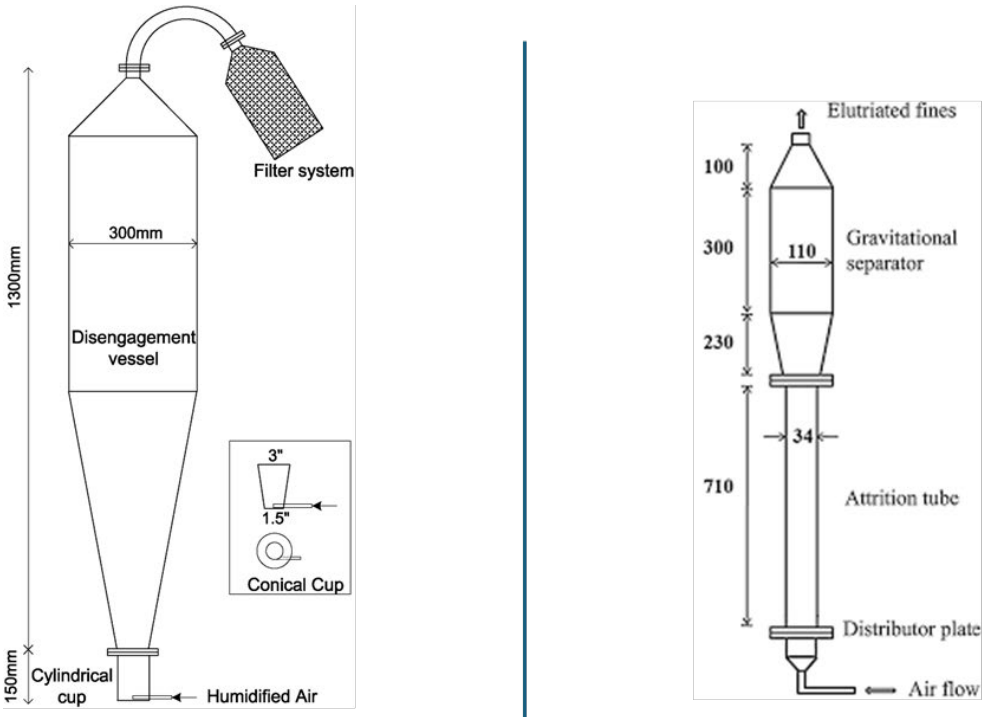

Figure 1.4: (A) Jet Cup attrition apparatus and (B) ASTM Fluidized Bed Attrition apparatus, reprinted with permission from (Kukade et al., 2016; Cocco et al., 2010)

1.7 Attrition Testing Methods

Various techniques, including the Davison jet cup, Hot attrition test, roller test, air jest test, ASTM D 5757, ultrasonic test, and uniaxial compaction test, are used to evaluate the attrition resistance of materials (Kukade et al., 2016).

1.7.1 Uniaxial Compaction Method

The strength and attrition of a material are tested using a cylindrical machine. In this test, the powder of material is compacted into the rigid die by using pressure in the direction of the axial in a punch rigid (Wilson et al., 2019).

1.7.2 Ultrasonic Test Method

In this test, the stress in solid particles inside a liquid experience some pressure when the ultrasonic forces are applied to them, and the attrition resistance is measured. The frequency and amplitude

of the suspension of solid particles in a liquid at medium temperature control ultrasonic forces (Alkassar et al., 2021).

1.7.3 Jet-cup Test Method

In this test, before attrition is measured, the rapid flow of air gets started, and particles begin to move around. In a small cup, particles move around and further go to the cyclone, like a chamber. The collision between the walls and particles caused by the high airflow velocity that transports particles causes attrition (Amblard et al., 2015).

1.7.4 ASTM Standard Fluidized Test Method

The test is performed in a fluidized bed under certain conditions. The sample amount is weighed out, and mass gets recorded. The weighed samples are transferred to the attrition tube for measurement. The airflow is started, and then particles are subjected to pressure. The fines are collected after a certain period, and the mass of the fines is recorded. The mass of the fines collected and weighed out, the mass of the sample weighed initially, and the time taken for the test are used to calculate the attrition resistance of the material. The attrition test behavior of the sample is dependent on the size of the particle, time, and temperature (Wu et al., 2016).

1.8 Aim and objectives

Aim

To design high surface area and attrition-resistant iron catalysts for F-TS.

Objectives

1) To synthesize iron catalysts using the co-precipitation, impregnation methods and spray drying technology.
2) To characterize the prepared catalysts using XRF, XRD, SEM, BET analysis and TGA.
3) To determine the activity and selectivity of the catalysts on F-TS.
4) To evaluate the recovery of the catalysts.

1.9 Hypothesis

The potassium promoter will donate electrons to the active metal (iron), and this will promote the formation of iron carbides (χ-Fe_5C_2) on the catalyst surface. The iron carbides (active sites for a

reaction) increase the chain growth, and this will favour the formation of long-chain hydrocarbons (C_{5+}).

1.10 Research Questions

The study was directed by the following important research questions.

1) Are the spray-drying, impregnation, and co-precipitation methods efficient for the preparation of iron catalysts?
2) Which catalyst will show high surface area and more attrition resistance?
3) Which catalyst will show good selectivity characteristics (low methane and high C_{5+} selectivity)?
4) Which catalyst will show high activity and stability in F-TS?

1.11 Anticipated contributions of the research project

This research project is anticipated to have an impact on the techniques currently utilized to evaluate iron catalysts attrition resistance. Various studies have been established for the development of attrition resistance iron F-TS catalyst and there is little progress. The lack of development of stable and attrition-resistant iron F-TS catalysts for use in a SBCR served as the basis for this study. Analyzing and reviewing relevant literature on different approaches taken by other researchers to enhance attrition resistance and catalyst deactivation could lead to insightful conclusions. The research project's primary contribution is to design an iron F-TS catalyst with a high surface area, stability, and attrition resistance to satisfy the demands of the industries, so it can be utilized in a slurry bubble column reactor. The results may direct future research efforts towards enhancing attrition resistance, stability, surface area and reducing catalyst deactivation through the application of the spray-drying technique. Spray-drying could be used by many to prepare a wide range of catalysts.

1.12 Thesis structure

This thesis consists of five chapters, starting with the first chapter, which introduces the background to the research, the problem statement, the highlights of the research methods that were used to conduct the research project, the aim and objectives of the research, hypothesis, research questions and the contribution of the research project.

In Chapter Two, F-TS reactions and mechanisms are explained in detail. The different catalysts that are usually used in F-TS are explained. Furthermore, the iron catalyst preparation methods are reviewed, including co-precipitation, microwave and impregnation. These are compared to the spray-drying technique. The support and promoters of iron catalysts are also explained in detail, followed by various studies conducted in the literature. The studies conducted on the mechanical strength of the materials are reviewed. The impact of process variables, such as temperature, pressure, and H_2/CO syngas ratio of on F-TS performance is reviewed. Lastly, various reactors using F-TS are explained in detail.

Chapter Three describes the experimental procedures for the preparation of iron catalysts. Furthermore, different characterization techniques, catalysts testing method are explained in detail, and the method for measuring the attrition resistance of the prepared iron catalysts.

Chapter Four consists of both experimental results and a discussion of the results obtained from the catalysts' testing and characterization.

The conclusion of this study and recommendations for future investigations are included in Chapter Five

References

Alkassar, Y., Agarwal, V.K., Pandey, R.K. and Behera, N. 2021. Influence of particle attrition on erosive wear of bends in dilute phase pneumatic conveying. *Wear*, 476: 203-209.

Amblard, B., Bertholin, S., Bobin, C. and Gauthier, T. 2015. Development of an attrition evaluation method using a Jet Cup rig. *Powder Technology*, 274: 455–465.

Bajaj, N.S. and Joshi, R.A. 2021. Energy materials and characterization techniques. *Energy Materials,* 202: 304-307.

Cheng, K., Kang, J., King, D.L., Subramanian, V., Zhou., Zhang, Q. and Wang, Y. 2017. Advances in catalysis for syngas conversion to hydrocarbon. *Advances in Catalysis*, 60: 125-208.

Gholami, Z., Tisler, Z. and Rubas, V. 2021. Recent advances in Fischer-Tropsch synthesis using cobalt-based catalysts: a review on supports, promoters, and reactors. *Catalysis Review,* 63: 45-48.

Cocco, R., Arrington, Y., Hays, R., Findlay, J., Karri, S. B. R. and Knowlton, T. M. 2010. Jet cup attrition testing. *Powder Technology*, 200: 224-233.

Kukade, S., Kumar, P., Rao, V.C.P and Choudary. V. 2016. Comparative study of attrition measurements of commercial FCC catalysts by ASTM fluidized bed and jet cup test methods. *Powder Technology,* 301: 472–477.

Loseva, N.I., Niyazbakiev, I.I. and Silman, A.V. 2019. Fisher–Tropsch Synthesis technology evolution. *IOP Conference Series: Material Science and Engineering*, 663: 88-95.

Santos, D., Mauricio, A.C., Sencada, V., Santos, D., Fernandes, M.A. and Gomes, P.S. 2018. Spray drying an overview. *Biomaterials Physics and Chemistry New Edition*. 1-9.

Wilson, D., Roberts, R. and Blyth, J. 2019. Powder compaction: process design and understanding. In: *Chemical Engineering in the Pharmaceutical Industry: Drug Product Design, Development, and Modeling*, 2nd ed., 203-225.

Wu, D., Wu, F. and Gu, Z. 2016. Catalyst attrition in an ASTM fluidized bed. *Catalysis Today,* 264: 70–74.

Yanga, J., Ma, W., Chena, D., Holmena, A. and Davis, B.H. 2014. Fischer–Tropsch Synthesis: A review of the effect of CO conversion on methane selectivity. *Applied Catalysis A: General,* 470: 250–260.

CHAPTER 2: LITERATURE REVIEW

This chapter focuses on reviewing the currently used iron catalysts and their performance in the Fischer-Tropsch Synthesis. The chapter further reviews and analyzes the published information on the performance of iron catalysts. The published review forms part of the dissertation and should be examined. Part of the published review that was selected for the dissertation includes the introduction and background, mechanisms for the F-TS, catalysts for F-TS, influence of reaction conditions on the F-TS process, promoters for iron catalysts and their effects on F-TS product selectivity, effect of unsupported iron catalysts on F-TS product selectivity, effects of supported catalysts on the F-TS product selectivity, effects of the various synthesis methods on the catalytic performance, spray-drying technology and mechanism, effects of iron catalysts prepared by spray-drying on the product selectivity, attrition of catalysts, and various iron catalysts evaluated on the attrition resistance.

There is a demand in industry for catalysts that can result in high selectivity, such as low-C_1 and high-C_{5+} hydrocarbons (Teimouri et al., 2021). Various studies were established to improve selectivity with the addition of promoters, supports, and various preparation methods (Table 2.2). The currently used catalysts are affected by deactivation (loss of catalytic activity) under F-TS conditions and stability. The spray-dying technique was reported to have the potential to decrease the deactivation of iron catalysts (Lin et al., 2021). In this study, the spray-dying technique is used to design suitable iron catalysts that would improve the selectivity characteristics of F-TS. There are several reactions involved in F-TS, demonstrating how various products can be generated.

2.1 F-TS reactions

In a F-TS reactor, the catalyst surface may experience multiple reactions. Below is a list of possible reactions in a F-TS reactor. The equations 2.1 to 2.8 illustrate how the chemical reactions occurring in F-TS can be further separated into [A] main reactions, [B] side reactions, and [C] catalyst modification reactions (James et al., 2012).

[A.] Main reactions:

Paraffin formation: $nCO + (2n + 1) H_2 \rightarrow CnH_{2n+2}\ nH_2O$ Equation 2.1

Olefin formation:

$nCO + 2nH_2 \rightarrow CnH_{2n} + nH_2O$ Equation 2.2

Water-gas shift (WGS) reaction:

$CO + H_2O \leftrightarrow CO_2 + H_2$ Equation 2.3

[B.] Side reactions:

Alcohol production:

$nCO + 2nH_2 \rightarrow CnH_{2n+1}OH + (n - 1) H_2O$ Equation 2.4

Boudouard reaction:

$2CO \rightarrow C + CO_2$ Equation 2.5

[C.] Catalyst modifications:

Catalyst oxidation/ reduction:

a. $MxOy + yH_2 \leftrightarrow yH_2O + xM$ Equation 2.6

b. $MxOy + yCO \leftrightarrow yCO_2 + xM$ Equation 2.7

Bulk carbide formation:

$yC + xM \leftrightarrow MxCy$ Equation 2.8

Where the number of carbon is n, based on several variables, especially H_2/CO ratio and type of the catalyst. M is the active metal (Fe), x and y in MO and MC in equation 2.6 and 2.8 are subscripts on the active metal used to show the number of carbon atoms of each element in the compound e.g. (Fe_2O_3, Fe_5C_2). From equations 2.6, 2.7 and 2.8; the subscripts y in front of H_2O, CO, CO_2, C and subscript x in M, are the coefficient of numbers added to balance the equations.

The α-olefin (equation 2.2) and linear (straight chain) paraffin (equation 2.1) are the principal by-products of F-TS. Water is a primary product in F-TS in addition to hydrocarbons, however, it is undesirable (James et al., 2012). The catalyst deactivates when there is water present in the product stream, which lowers the amount of CO converted and the selectivity to hydrocarbons. Therefore, to increase the F-TS activity, the amount of water produced must be reduced. This can be accomplished in a water-gas shift reaction (equation 2.3). A low H_2/CO ratio of less than one can only be converted using iron catalysts. In F-TS, alcohol and oxygenate products are produced in addition to linear hydrocarbons and water (equation 2.4). Another possible reaction is when CO separates on a surface and combines with another molecule of CO to generate CO_2 and C (equation 2.5) (Chen et al., 2018). The activation for F-TS can be done using H_2 (equation 2.6), CO

(equations 2.7 and 2.8), or syngas. The F-TS mechanism shows how carbon monoxide (CO) is converted to produce various hydrocarbons (Iris et al., 2021).

2.2 The F-TS mechanism

Different F-TS mechanisms, including carbide, CO insertion, and enol mechanisms, have been suggested. However, F-TS reaction using iron catalysts in this study follows the carbide mechanism where surface carbides are the active phase (χ-Fe_5C_2) for producing the C_{5+} hydrocarbons. Chain formation, chain development, and chain closing are the three fundamental steps in which the processes operate (Figure 2.1) (Van Santen et al., 2013). The hydrogenation of carbon atoms and CHx polymerisation promote chain formation, whereas the carbide process presumes the separation of CO and H_2 in carbide mechanism. The addition of a hydrogen atom to the chain results in the closing of a chain. Jacobs and Davis, (2014) suggested that the CO insertion mechanism is comprised of CO adsorption and surface hydrogenation reaction that results in the formation of an aldehyde (CHO) group. Adding CO causes the chain to extend, while adding hydrogen atoms causes the chain to close (Jacobs and Davis, 2014). Finally, the enol mechanism takes place when CO is adsorbed and hydrogen is added, resulting in the formation of an Enol group (CHOH). Chain development occurs during the loss of water through condensation polymerization. When hydrogen is incorporated, the chain closes (Iris et al., 2021). A critical step in F-TS is catalyst selection because these reactions primarily take place on the catalysts' surfaces. Typically, the catalysts are chosen according to their characteristics, cost, and accessibility.

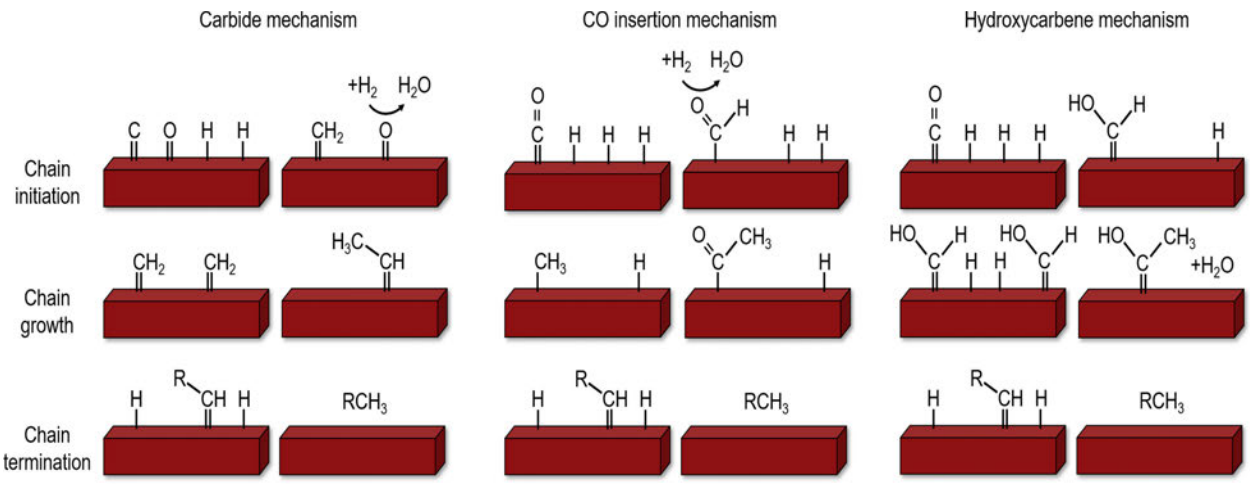

Figure 2.1: The F-TS mechanism, reprinted with permission from (Iris et al., 2021)

2.3 Choice of the active metal in F-TS

Iron (Fe), cobalt (Co), nickel (Ni), and ruthenium (Ru) are four active metals utilized as catalysts in F-TS. The relationship between these four active metals and F-TS product distribution is exhibited in Table 2.1 (Chai et al., 2023; Shafer et al., 2019). The active metals that show high activity in F-TS are those with better dissociative adsorption of CO and H_2 and the easy reducibility of the metal oxide as shown in Table 2.1 (Hussian et al., 2023; Shafer et al., 2019). Despite their maximum activity in the F-TS reaction, Ru and Ni are typically not appropriate for use as catalysts in industrial process due to several disadvantages such as their high methane selectivity and limited availability, respectively. For industrial applications, iron and cobalt are regarded as catalysts. Iron has several benefits that make it the catalyst of choice for F-TS, such as less sensitivity to toxins, greater flexibility in feed stocks with $H_2 < 1$ or higher, and better activity for F-TS (Shafer et al., 2019). In contrast, cobalt provides greater selectivity for each individual product, however, its use is restricted to high molar feed ratios of $H_2/CO > 1$. Cobalt is typically used for low-temperature F-TS (LTFT), with its main product being wax, while iron can be utilized for both high and low temperature F-TS and produces a range of products from waxes to light olefins, a critical monomer for chemical industries.

The use of cobalt catalysts is limited as they promote the production of waxes. The cobalt catalyst is capable of reabsorbing C_2-C_4 products produced at high-activity sites, thereby raising the length of the hydrocarbon chain, and causing a reduction in the hydrogenation reaction. Waxes are then

specifically converted to produce high-quality end products such as diesel, while olefins are most required in the chemical industry. Compared to cobalt catalysts, iron catalysts are currently of great interest, due to their high reactivity. The only catalysts thought to be able to attain superior selectivity to C_2-C_4 hydrocarbons are iron catalysts (Shafer et al., 2019). In the chemical industry, the C_2-C_4 hydrocarbons are utilized as raw materials to create a variety of polymers. Many researchers' aim to design a catalyst with a large surface area. This is typically accomplished by adding support material while a catalyst is being prepared.

Table 2.1: The relationship between active metals and F-TS product distribution

Active metal	**Ni**	**Fe**	**Co**	**Ru**
Price	++++	+	+++	+++++
Fischer-Tropsch activity	+	+	+++	+++++
Hydrogenation activity	+++++	+	+++	+++

+ Active

2.4 The effect of the support

The main purpose of the support, sometimes referred to as the carrier, is to keep the active components' surface area high (Choi et al., 2017). Supports disperse the active component to reduce the loss of catalytic activity by acting as stable surfaces.

2.4.1 The use of supported iron catalysts in F-TS

The various support materials that are used to enhance the catalytic properties of iron catalysts are displayed in Table 2.2. Activated carbon (AC), silicon carbide (SiC), graphite (G), silicon dioxide (SiO_2), and alumina (Al_2O_3) are some examples of these support materials. The results in Table 2.2 show that the performance of iron catalysts has been impacted differently by the type of support used. Of all the iron catalysts in Table 2.2, the graphite-supported iron catalyst exhibited the highest selectivity to C_{5+} of 75.3%. However, the catalysts showed a lower performance of 28.4% CO conversion and 22.9% C_2-C_4 selectivity (Li et al., 2016). The catalysts with zeolites (H-ZSM-5 and Na-ZSM-5) showed less performance in CO conversion and C_{5+} than all catalysts in Table 2.2. These catalysts showed 14.4% CO conversion and 11.5% C_{5+} selectivity. On the other hand,

the catalyst supported with Na-ZSM-5 demonstrated poor performance of 7.3% CO conversion and 11.5% C_{5+} selectivity (Liu et al., 2020). These supported catalysts can be improved by changing the catalyst preparation method. The ion exchange and incipient wetness impregnation method used may not be convenient for the preparation of these supported catalysts. The iron catalysts supported with silicon carbide (FeSiC) showed less performance with 15.5% CO conversion, 20.7% C_2-C_4 and 38.1% C_{5+} selectivity (Zhao et al., 2018). The selectivity of this catalyst can be further improved either by changing the preparation method or using a different support. The iron catalyst (KFeSi) prepared using the spray-drying and co-precipitation method showed better performance by producing 78.74% C_5-C_{11} hydrocarbon selectivity. However, the catalyst showed less performance with 44.9% CO conversion and 16.25% C_2-C_4 selectivity (Cheng et al., 2016).

Enhancing the catalyst activity is necessary to achieve high C_5-C_{11} hydrocarbons selectivity. The catalyst supported with carbon (FeC@C) performed less by showing 20.9% C_5-C_{11} selectivity (Zhao et al., 2018). The carbon support is not suitable for producing high selectivity to C_2-C_4 and C_5-C_{11} hydrocarbons. Although other catalysts presented in Table 2.2 showed good CO conversion and C_5-C_{11} selectivity, the selectivities demonstrated are still relatively low. From the results shown in Table 2.2, more work needs to be done to improve the supports' ability to convert CO and increase their selectivity toward high-molecular-weight hydrocarbons (C_2-C_4 and C_{5+}). To improve the iron catalyst activity and selectivity, different promoters are added.

Table 2.2: Other studies based on the use of supported iron catalysts for F-TS

Catalysts	Preparation method	H_2/CO	Temperature (°C)	Pressure (MPa)	CO conversion (%)	C_2-C_4 Selectivity (C-%mol)	C_{5+} Selectivity (C-%mol)	Reference
FeSi	Co-precipitation and spray-drying	2	260	1.5	21.01	33.97	48.64	Cheng et al., 2016
SrFeSi		2	260	1.5	20.38	20.15	67.87	
KFeSi		2	260	1.5	42.90	16.25	78.74	
FeC@C	Pyrolysis and wetness impregnation	1	340	1	73.2	30.6	20.9	Zhao et al., 2018
FeOx/AC		1	340	1	42.1	18.8	46.4	
FeSiC		1	340	1	15.5	20.7	38.1	

Table 2.2: Continued

Catalysts	Preparation method	H_2/CO	Temperature (°C)	Pressure (MPa)	CO conversion (%)	C_2-C_4 Selectivity (C-%mol)	C_{5+} Selectivity (C-%mol)	Reference
100Fe/100G	Co-precipitation and wetness impregnation	1	260	2	44.9	44.9	55.4	Li et al., 2016
100Fe/100G/5K		1	260	2	28.4	22.9	75.3	
5Fe/100H-ZSM-5	Ion exchange and incipient wetness impregnation	2	300	2.1	14.4	30.2	11.7	Liu et al., 2020
5Fe/100Na-ZSM-5		2	300	2.1	7.3	27.8	11.5	

2.5 The effect of promoters

By altering the surface characteristics of a catalyst, a promoter is a metal that is added in smaller quantities to boost the catalysts activity and selectivity (Barrios et al., 2020; Zhang et al., 2022). Alkali metals are the main substances that promote iron catalysts.

2.6 The role of promoters in F-TS product distribution

The three widely used promoters for iron catalysts are manganese (Mn), copper (Cu), and Potassium (K). The potassium promoter releases electrons to the iron metal, increasing CO adsorption and decreasing H_2 adsorption. As a result, the selectivity of hydrocarbons (C_2-C_4 and C_{5+}) increases (Zhang et al., 2015). Additionally, potassium decreases the selectivity of CH_4 (methane). Zhang et al. (2015) achieved 28% C_{5+} selectivity and 91% conversion of CO using the bare iron catalyst (Fe_2O_3), however, when they utilized the iron promoted with potassium, the CO conversion increased to 97% while the C_{5+} selectivity increased to 48% (Zhang et al., 2015). The authors discovered that incorporation K to the iron catalyst enhances both C_{5+} hydrocarbon selectivity and conversion of CO. Copper is one of the important promoters and it usually added to facilitate the reduction of iron or activation with carbon monoxide to form iron carbide which is the active phase for F-TS. Copper also plays a role to increase the chain growth and produce C_{5+} hydrocarbons' (Barrios et al., 2020). Zhang et al. (2016) discovered that employing the promoted ($FeMnO_2$) catalyst greatly enhanced the C_{5+} selectivity, increasing it from 44.6% to 66.6%. It was discovered that manganese considerably accelerated the dissociation of CO. Additionally, the C_1 hydrocarbon selectivity dropped from 16.8% to 8.9% (Zhang et al., 2016).

2.7 The use of unsupported iron catalysts in F-TS

These catalysts are usually synthesized in large quantities, or in bulk. Various preparation methods, supports, and promoters have been used in numerous attempts to improve the catalytic characteristics of unsupported iron catalysts. Table 2.3 demonstrates that most unsupported iron catalysts are promoted by various promoters to increase their selectivity and CO conversion. However, high loading of the promoters added to the catalyst has disadvantages, even though they can increase the iron catalyst's selectivity. According to Li et al. (2014), when a promoter's loading increased from 0.7% to 2.8%, the CO conversion and selectivity also increased. However, when a promoter's loading was further increased to 3.5%, conversion of CO and selectivity of hydrocarbons decreased, as shown in Table 2.3 (Li et al., 2014). Furthermore, the results in Table 2.3 demonstrated that when the silver (Ag) loading was increased from 0.6% to 1.3%, the CO conversion decreased while C_2-C_4 and C_{5+} hydrocarbons increased.

In a study conducted by Zhang et al. (2015), the authors reported that the addition of the zinc promoter to iron catalysts resulted in a high CO conversion of 98.3%. However, the drawbacks

were that the catalyst showed low selectivity of 18.1% C_2-C_4 and 29.9% C_{5+} hydrocarbons, respectively (Zhang et al., 2015). The catalysts promoted with zinc showed poor performance in terms of selectivity to C_2-C_4 and C_{5+} hydrocarbons as compared to iron catalysts promoted with sodium, manganese, and potassium promoters under similar conditions of the F-TS reaction and similar synthesis method (Zhang et al., 2015). Moreover, increasing the potassium loading increased C_2-C_4 and C_{5+} hydrocarbons selectivity, however, the decrease in CO conversion was a disadvantage as shown in Table 2.3 (Pendyala et al., 2014). The overall selectivity characteristics of the unsupported catalysts in Table 2.3 can be improved. The common challenge usually encountered by catalysts used in F-TS is the loss of activity, which reduces their performance in F-TS. There is a need to enhance the stability of unsupported iron catalysts to ensure the catalysts can withstand F-TS conditions and demonstrate good performance. This study aims to address this gap.

An essential step in F-TS is deciding a suitable preparation method that will generate a catalyst with characteristics that can lead to good catalytic sites on the catalysts surface (Buthelezi et al., 2024). There are numerous ways to create iron catalysts, and the performance of the catalysts varies depending on the synthesis method used.

Table 2.3: Promoted, unsupported iron catalysts for F-TS

Catalysts	Preparation method	H_2/CO	Temperature (°C)	Pressure (MPa)	CO conversion (%)	C_2-C_4 Selectivity(C-%)	C_{5+} Selectivity(C-%)	Reference
100Fe/4Cu/2Mg	Microemulsion	1	270-310	1.7	62.3	38.7	50.4	Zamani, 2015
100Fe/ 33Mn/0.7Na	Co-precipitation and spray-drying	2	325	3.5	91.4	3.6	32.6	Li et al., 2014
100Fe/ 33Mn/1.4Na		2	325	3.5	94.5	4.8	36.9	
100Fe/ 33Mn/2.1Na		2	325	3.5	95.8	5.3	37.8	
100Fe/ 33Mn/2.8Na		2	325	3.5	96.2	7.6	32.4	
100Fe/ 33Mn/3.5Na		2	325	3.5	93.3	6.3	35.9	
100Fe/ 0.1Na	Co-precipitation	2	320	1.5	40.09	6.2	45.8	Gholami et al., 2022
100Fe	One-pot solvothermal	1	280	2.0	80.1	38.5	16.8	Zhang et al., 2015
100Fe/0.6Ag		1	280	2.0	73.0	41.0	23.1	
100Fe/0.9Ag		1	280	2.0	71.4	43.0	24.3	
100Fe/1.3Ag		1	280	2.0	74.1	35.8	22.6	

Table 2.3: Continued

Catalysts	Preparation method	H_2/CO	Temperature (°C)	Pressure (MPa)	CO conversion (%)	C_2-C_4 Selectivity(C-%)	C_{5+} Selectivity(C-%)	Reference
Fe	One-pot solvothermal	1	280	2.0	91.0	19.3	28.0	
Fe/Na		1	280	2.0	93.2	23.3	47.8	Zhang et al., 2015
Fe/K		1	280	2.0	97.1	22.1	41.3	
Fe/Zn		1	280	2.0	98.3	18.1	29.9	
Fe/Mn		1	280	2.0	37.4	34.1	28.6	
100Fe	Co-precipitation	0.7	270	1.3	59.0	25.1	68.7	Pendyala et al., 2014
100Fe/0.5K		0.7	270	1.3	57.3	23.1	71.7	
100Fe/1.0K		0.7	270	1.3	55.6	20.3	75.2	
100Fe/2.0K		0.7	270	1.3	56.1	12.5	84.5	
100Fe	Co-precipitation	3	350	2.0	90.04	46.94	20.56	Zhao et al., 2018
Fe/Zn= 1/1		3	350	2.0	95.09	53.32	13.26	

2.8 Effect of catalyst synthesis method on catalytic activity

Due to precipitation creating multiple active sites, it typically yields the best-performing iron catalysts in F-TS. The precipitation method accelerates the mass production of catalysts and yields high-surface-area catalysts (Cheng et al., 2015). The final synthesized catalyst's particle size and surface area, which dictate its F-TS activity and selectivity, can be greatly impacted by manufacturing processes.

2.8.1 The effect of catalyst synthesis method on iron catalysts' selectivity in F-TS

Arsalanfar et al. (2014) investigated how the various methods of catalyst preparation affected the Fe-Co-Mn catalysts' activity. The catalysts were synthesized using various preparation methods, including co-precipitation, incipient wetness impregnation, dry impregnation, and sol-gel methods. All the prepared catalysts were then evaluated for CO hydrogenation via F-TS using identical operating conditions. The authors discovered that the catalysts showed different CO conversions and product selectivity, and that the preparation technique influences catalytic performance as shown in Figure 2.2. The catalyst synthesized using the co-precipitation method demonstrated superior catalytic activity, with high selectivity to C_2-C_4 hydrocarbons (Arsalanfar et al., 2014). The overall results in Figure 2.2 show low selectivity for high molecular weight hydrocarbons (C_2-C_4 and C_{5+}).

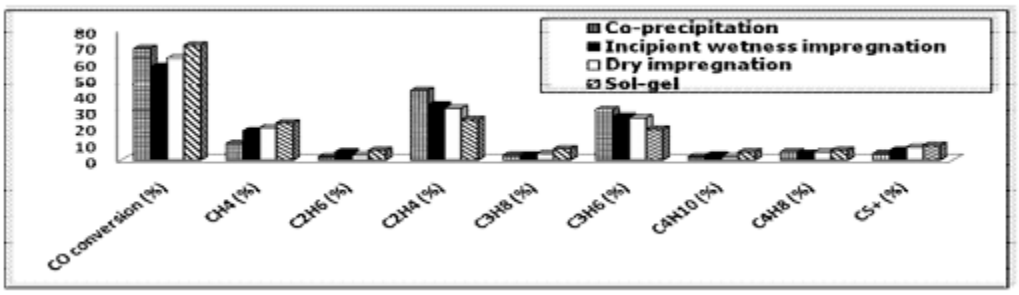

Figure 2.2: The effect of synthesis method on the catalytic performance, reprinted with permission from (Arsalanfar et al., 2014)

Table 2.4 further shows the F-TS performance of iron catalysts prepared using various methods. Compared to all other methods in Table 2.4, sol-gel auto combustion combined with the carbothermal method exhibited superior C_2-C_4 selectivity of 33.8% and 41.3% C_5-C_{11} hydrocarbon

selectivity (Xue et al., 2018). The overall results in Table 2.4 show that all the iron catalysts prepared by various preparation methods are not selective enough to produce high selectivity to C_2-C_4 and C_5-C_{11} hydrocarbons. According to Table 2.6, other studies revealed that the spray-drying technique has the potential to enhance the activity and selectivity of iron catalysts (Lin et al., 2021; Aghamohammadi et al., 2019).

Table 2.4: The effect of various preparation techniques on hydrocarbons selectivity

Catalysts	Conditions	Preparation method	C_2-C_4 Selectivity (C-%mol)	C_5-C_{11} Selectivity (C-%mol)	Reference
100Fe/4Cu/4K/6Zn	T=280°C,	Co-precipitation	23.5	15.6	Mai et al., 2015
100Fe/4Cu/4K/6Zn	P=2.5 MPa and H_2/CO=0.77	Impregnation	27.3	13.8	
FeCuK/Al_2O_3	T=300°C, P=1.0 MPa and H_2/CO= 2	Co-precipitation and impregnation	37.4	48.5	Kang et al., 2011
FeCuK/SiO_2			27.1	58.7	
K/FeCuAlO_X			30.9	59.2	
K/FeO_X			25.9	66.6	
5 Mn/ 10Fe_2O_3	T=270°C, P=10 bar and H_2/CO= 2	Impregnation and Microwave	47.7	22.8	Mohiuddin, 2011
5 Mn/ 100Fe_2O_3		Impregnation	43.8	21.5	
100Fe-0.3G	T=240°C, P=20 bar and H_2/CO= 2	Sol-gel Auto combustion combined carbothermal	33.8	41.3	Xue et al., 2018

2.9 Spray-drying

One established process for turning liquids, suspensions, or emulsions into solid products is spray drying (Nandiyanto and Okuyama, 2011). Feeding a liquid stream that is continuously divided into tiny droplets, a solution, suspension, or emulsion is the basis of the spray-drying technique. A carrier gas carries the produced droplets into the drying chamber, where they solidify into particles in order to remove the solvent using heat and mass transfer. A fine powder is then collected after

these particles are separated using a separation unit, usually a moist cyclone. Due to its effectiveness, speedy particle production, few material preparation procedures, and tunable morphology, spray-drying has attracted a lot of interest (Nandiyanto and Okuyama, 2011). Across a range of industries, spray-drying has been utilized to produce a variety of products, including chemicals, biochemicals, medicines, sensors and catalysts (Arias, 2021). The preparation of iron catalysts will be conducted in this study using the spray-drying method. In the procedure, atomization, droplet-to-particle conversion, and particle collection are the three steps in sample preparation, as illustrated in Figure 2.2. The pressure, feed flow rate, input and output temperatures are the spray drying parameters (Nandiyanto and Okuyama, 2011).

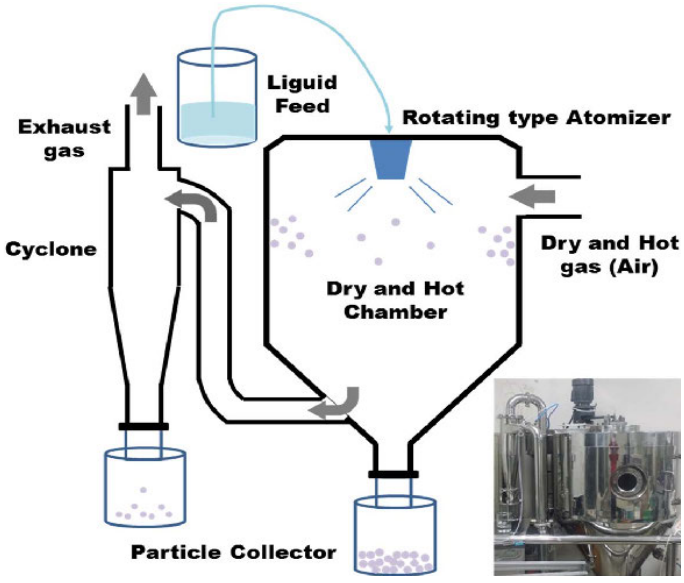

Figure 2.3: The spray drying technology, reprinted with permission from (Nandiyanto and Okuyama, 2011)

2.10 Mechanism of spray-drying

2.10.1 Atomization

A decrease in surface tension allows the feed solution to atomize into tiny droplets, which initiates the spray-drying process. This step is crucial for the next steps, particularly when the drying chamber is exposed. The heat transfers between the heated drying gas and liquid particles are maximized, when the solution is divided into multiple droplets because this increases their surface

area. This produces the perfect conditions for the evaporation process, which is vital to the development of desiccated particles (Szczap and Jacobs, 2023). The phenomenon of liquid breakdown serves as the foundation for the fundamental physical principle that controls the atomization transformation process.

2.10.2 Droplet-to-particle conversion

In the spray-drying mechanism, the atomization step is conducted by the change from droplets to particles. The spray contact with the air and the dried droplets are two significant steps that characterize this stage. As a result, the droplets' solvent content is eliminated, turning them into desiccated particles (Nandiyanto and Okuyama, 2011).

2.10.3 Collection of particles

Once the process of converting droplets into particles is accomplished, the necessity arises to gather the dried powder. The dried particles and drying gas are isolated during the process. The separation process typically consists of two distinct steps, referred to as main and intermediate separation. During the main separation step, the particles with the highest density settle at the conical bottom of the drying chamber and are then recovered. During the intermediate separation step, the tiny particles also known as the finest particles are moved to external devices and isolated from the moist air. (Santos et al., 2018). The use of spray drying enables the production of spherical materials from a slurry solution, resulting in the formation of powders with uniform sizes. The spray-dried catalysts are highly valued in fluidized bed reactors due to their spherical shape, exceptional hardness, resistance to attrition, and consistent size. The advantage of employing a spray drying method lies in the ability to control the particle size by manipulating several factors such as the conditions, slurry concentration, flow rate, and pressure (Santos et al., 2018).

2.11 Operational factors influencing the morphology of spray-dried products

The effect of process variables on particle shape, include the length of time particles stay in the drying chamber, the atomization process, and its conditions. It is difficult to make general judgments about feed parameters, such as concentration, temperature, and feed aeration level, and drying air temperature (Nuzzo et al., 2015). This is caused by the unique drying properties of many materials in addition to an insufficiency of data in literature (Gorge et al., 2023). There is also a challenge in classifying morphological events in terms of dryer operation because the particles

produced during drying are primarily physical and chemical (Gorge et al., 2023). Under specific drying conditions, the particles could swell, or break based on stress or pressure characteristics or lack of pores in the formed particle. The optimization of the parameters can be conducted successfully depending on the kind of material to be spray-dried and the powder required as shown in Table 2.5 (Gorge et al., 2023; Saadatkhah et al., 2017). Various studies have examined the use of the spray-drying process to create iron catalysts for the F-TS, the findings are displayed in Table 2.7.

Table 2.5: The relationship between the spray-dried powder temperature and feed concentration (Saadatkhah et al., 2017)

Increase drying temperature	**Increase in slurry concentration**
Decrease drying time	Decreases surface irregularities
Increases particle size	Increases particle size
Decreases bulk density	Reduces thermal degradation
Increases particle vacuolation	Increases bulk density
	Decreases particle vacuolation

2.11.1 Spray-dried iron catalysts application in F-TS

The advancement of abrasion-resistant catalysts through the utilization of spray-drying innovation has attracted a lot of attention lately, as it enhances catalytic properties such as stability. Most of the catalysts in F-TS deactivate easily (loss of catalyst activity), and are unable to withstand F-TS conditions, and their performance decreases. The spray-drying technique has potential to enhance the activity of the catalyst. The stability of a spray-dried catalyst (100Fe/4.4Cu/3.5K/21SiO_2) was investigated by Lin et al. (2021) in a SBCR. The authors reported that all catalysts showed a small deactivation rate at 200 h reaction time. The iron catalyst (100Fe/4.4Cu/3.5K/21SiO_2) showed less deactivation compared to other catalysts, and it was found that as the silicon loading increases, the deactivation decreases, as shown in Table 2.6 (Lin et al., 2021). These results indicate that the catalysts prepared by spray-drying are stable under F-TS conditions as compared to other preparation methods.

Table 2.6: The stability of the catalysts prepared by spray-drying under F-TS conditions

Catalysts	Conditions	Preparation method	Deactivation rate (%/h)	Reference
100Fe/4.4Cu/3.5K/12.5% SiO_2	T=265 °C, P=2.3 MPa and H_2/CO=2	Co-precipitation and spray-drying	0.55	Lin et al., 2021
100Fe/4.4Cu/3.5K/15.0% SiO_2			0.42	
100Fe/4.4Cu/3.5K/17.5% SiO_2			0.24	
100Fe/4.4Cu/3.5K/21.0% SiO_2			0.13	

Table 2.7 lists several studies on the preparation of iron catalysts for F-TS using the spray-drying technique. According to the results in Table 2.7, iron catalysts synthesized by various methods, including precipitation and impregnation methods, easily undergo attrition, which decreases their performance in F-TS. The spray-drying technique has shown the potential to improve iron catalysts' performance in F-TS. In a study reported by Chen et al. (2022), a high selectivity of 93.6% for C_5-C_{11} hydrocarbons was obtained using the spray-dried iron catalyst (Fe_2O_3) compared to the other catalysts. However, the catalyst produced a high selectivity of C_1 (Chen et al., 2022). The catalyst properties require improvement to decrease C_1 because industries need a catalyst that produces low C_1 and high C_5-C_{11} or C_{5+} hydrocarbons. Enhancing the selectivity properties of iron catalysts is still necessary.

In another study reported by Guo et al. (2016), iron catalysts that show high selectivity characteristics (low C_1 and high C_5-C_{11} or C_{5+} hydrocarbons) were synthesized using the spray-drying and co-precipitation methods. All the catalysts showed low selectivity of C_1 less than 4% and high selectivity of C_5-C_{11} hydrocarbons greater than 80%. The catalyst Fe/Cu/K/13 SiO_2 demonstrated superior performance over the other catalysts (Table 2.7) with low selectivities of 2.3% to C_1 and high C_5-C_{11} of 86.8%. However, the drawback was that the catalysts showed CO conversion that was less than 62% (Guao et al., 2016). The catalyst 100Fe/3.5Cu/1.90K/10.28SiO_2 prepared by Li et al. (2022) showed good selectivity. A 89.0% CO conversion, 3.2% C_1, and 73.1% C_5-C_{11} hydrocarbons selectivity were obtained, respectively (Li et al., 2012). The obtained results show potential for the use of a spray-drying and co-precipitation method to prepare iron catalysts with high selectivity. The catalysts reported by Li et al. (2018) and Zhang et al. (2012) showed

poor performance as they produced high C_1 and low CO conversion. These catalysts are likely to be affected by attrition which likely decreased their F-TS performance.

Table 2.7: The effect of spray-dying on the selectivity of iron-based catalysts

Catalysts	Conditions	Preparation method	CO conversion (C-%)	C_1 Selectivity (C-% mol)	C_5-C_{11} Selectivity (C-% mol)	Reference
100Fe/3.55Cu/1.90K/10.28SiO_2	T=270°C, P=2.3MPa and H_2/CO=3	Co-precipitation, spray-drying, and impregnation	89.0	3.2	73.1	Li et al., 2022
100Fe/3.76Cu/2.04K/11.33SiO_2/0.14Cl			53.9	4.5	66.4	
100Fe/3.53Cu/1.85K/10.33SiO_2/1.00Cl			31.1	4.2	78.4	
Fe/SiO_2	T=270°C, P=1.5MPa and H_2/CO=0.67	Co-precipitation, spray-drying, and impregnation	29.06	9.07	61.12	Zhang et al., 2012
Fe-Zr/SiO_2			26.31	7.88	66.39	
Fe-K/SiO_2			54.48	6.63	71.56	
2SrFeSi	T=260°C, P=1.5 MPa and H_2/CO= 2.0	Co-precipitation and spray-drying	19.26	11.98	67.87	Li et al., 2018
4SrFeSi			20.08	9.68	72.98	
6SrFeSi			23.71	8.83	74.71	
10SrFeSi			66.37	16.66	39.65	
15SrFeSi			89.60	15.83	47.44	
Fe-Mn-K-SiO_2	T=265°C, P=0.65MPa and H_2/CO= 1.2	Co-precipitation and spray-drying	42.56	11.40	39.46	Ding et al., 2013
Fe_2O_3	T=270°C, P=2 MPa and H_2/CO= 3.5	Co-precipitation and spray-drying	67.9	10.2	93.6	Chen et al., 2022
Fe/Cu/K/0SiO_2	T=235°C, P=2.3 MPa and H_2/CO= 1.5	Co-precipitation and spray-drying	60.5	3.5	83.9	Guo et al., 2016
Fe/Cu/3.5K/5SiO_2			51.2	3.2	84.2	
Fe/Cu/K/8SiO_2			52.0	2.5	85.7	
Fe/Cu/K/13 SiO_2			51.0	2.3	86.8	
Fe/Cu/K/15 SiO_2			53.6	2.5	86.3	

2.12 Attrition of catalysts

Attrition is the process by which solid fragments or fine particles of a catalyst are created after colliding with the reactor walls. There are two types of attrition that catalysts can undergo during deactivation, physical or chemical attrition (Lin et al., 2021).

2.12.1 Improving the attrition resistance of iron

Literature suggests that a variety of factors, including phase transformation, carburization, silicon dioxide type and concentration, size, and shape of the particles formed during F-TS are significant in determining the attrition strength of iron catalysts in the process. Most industrial catalysts are spherical in shape, and this shape is achieved by spray-drying iron catalysts to increase their attrition resistance (Burk et al., 2004). The ASTM and Jet Cup are the most well-known and frequently utilized techniques for measuring the attrition resistance of the catalysts. These techniques, which are currently in use in industry, were compared and shown to yield measured and trustworthy results (Kukade et al., 2016). The high fines lost (wt%) per hour mean that catalysts have less attrition resistance, and the smaller fines lost (wt%) per hour indicate that catalysts have more attrition resistance (Buthelezi et al., 2024).

Catalysts produced through spray-drying are typically employed in slurry bubble column reactors (SBCRs) or stirred tank reactors (STRs). Nevertheless, there are challenges involved in using a slurry bubble column reactor, such as the difficulty of separating catalyst from wax. The catalyst becomes more difficult to separate from wax when it fragments during F-TS into particles smaller than 10 μm in diameter, and this causes catalyst deactivation (Lin et al., 2021). The main discovery from earlier research is that the unsupported iron catalysts prepared using precipitation methods readily break down into smaller particles from the reactor in F-TS (Burk et al., 2004; Zhao et al., 2018). Highly stable iron catalysts under F-TS conditions are required for the industrial application (Gao et al., 2020).

Lin et al. (2012) reported attrition studies of an iron F-T catalyst (Fe-Cu-K-SiO_2) used in a pilot-scale stirred tank reactor under F-T reaction conditions. The iron catalyst was prepared using the spray-drying method, and the attrition resistance test was performed using the ASTM method. The results showed that after 408 h of reaction in a STR, the particle size gets reduced due to attrition. The authors reported an increase in the fraction of particles less than 10 μm, which was 18.25% and 30.11%, respectively. The catalysts underwent more severe attrition, which was caused by the breakage of small and large particles (Lin et al., 2012). Based on the results presented in Table 2.8, the use of spray-drying shows potential to improve attrition resistance of iron catalysts. The spray-drying technique and co-precipitation method are mostly used to improve the attrition resistance of iron catalysts. Furthermore, most of the studies are focused on adding various amounts of silicon dioxide (SiO_2) to the iron catalysts to improve their attrition resistance. It was found that high amounts of silicon dioxide improve attrition resistance (Lin et al., 2021).

In a study reported by Lin et al. (2021), the authors used the spray-drying method to prepare high attrition resistance and stable iron catalysts for the F-TS. The study showed that with an increase in silica content (from 12.5% to 21% SiO_2), the attrition resistance and reactive stability of the catalysts were enhanced, and the deactivation of the catalyst was reduced (Lin et al., 2021). Although the addition of silicon dioxide shows potential to improve attrition resistance, according to Lin et al. (2021), their drawbacks was that the catalysts activity declined due to inhibition of further reduction of the catalysts. The results in Table 2.8 show that Guo et al. (2016) prepared iron catalysts with good attrition resistance using the spray drying and co-precipitation methods. All the catalysts showed attrition loss that is less than 5%, indicating that the spray-dried iron catalyst sufficient for use in SBCR. The iron catalyst with 13% SiO_2 showed improved attrition resistance, with the lowest attrition loss of 1.89% (Guo et al., 2016). However, their drawbacks were that the catalysts experience activity decline at high silicon dioxide loading (13% SiO_2 and 15% SiO_2).

Another study reported by Duvenhage et al. (2014) showed the highest attrition resistance of iron catalysts compared to all other studies presented in Table 2.8. The catalyst (100Fe/5Cu/4.7K/ 32%SiO_2) with Fe_2O_3 content of 0.72% produced an attrition loss of 0.28%. The catalyst (100Fe/5Cu/4.7K/32%SiO_2) containing 49% Fe_2O_3 showed high attrition resistance with the lowest attrition loss of 0.12% (Duvenhage et al., 2014). The results obtained from the study

indicate the potential of the co-precipitation and spray-drying methods to prepare more attrition resistance iron catalysts. However, the stability of the catalyst needs to be further improved before they can be utilized at industry. Other preparation methods, such as sol-gel, show a potential to produce high-attrition resistance iron catalysts, as shown in Table 2.8. Zhang et al. (2021) investigated the effect of alumina content on the attrition resistance of iron catalysts. The iron-based catalysts increased with an increase of alumina content, which was attributed to the enhanced interaction between the active component (iron) and alumina. The addition of alumina contributed to increasing the attrition resistance as compared to the iron catalyst (Fe-0%Al) without alumina, which showed less attrition resistance (Zhang et al., 2021).

Table 2.8: Measurements of attrition-resistance of iron catalysts studies

Catalysts	Preparation method	Attrition Test method	Time (h)	Attrition loss rate (wt%/h)	Reference
Fe/Cu/K/0SiO_2	Co-precipitation and spray-drying	ASTM	5	4.14	Guao et al., 2016
Fe/Cu/3.5K/5SiO_2			5	3.11	
Fe/Cu/K/8SiO_2			5	2.55	
Fe/Cu/K/13 SiO_2			5	1.89	
Fe/Cu/K/15SiO_2			5	3.01	
100Fe/4.4Cu/3.5K/12.5SiO_2	Co-precipitation and spray-drying	ASTM	5	9.8	Lin et al., 2021
100Fe/4.4Cu/3.5K/15.0SiO_2			5	7.2	
100Fe/4.4Cu/3.5K/17.5SiO_2			5	6.2	
100Fe/4.4Cu/3.5K/21.0 SiO_2			5	5.2	
100Fe/5Cu/4.7K/32SiO_2 with 0.72% Fe_2O_3	Co-precipitation and spray-drying	ASTM	1	0.28	Duvenhage et al., 2014
100Fe/5Cu/4.7K/ 32SiO_2 with 49% Fe_2O_3			2	0.12	
Fe-60Al	Sol-gel	ASTM	4	2.05	Zhang et al., 2021
Fe-50Al			4	2.94	
Fe-40Al			4	3.78	
Fe-30Al			4	8.53	
Fe-20Al			4	31.0	
Fe-0Al			4	35.0	

2.13 Influence of operating conditions

The distribution products are affected by reaction parameters such as temperature and pressure, gas hourly space velocity, and H_2/CO. The identification criteria of the products, such as alcohols, olefins, naphtha, diesel, or wax compounds, determine the choice of reaction conditions and catalyst type (Todic et al., 2016). The impact of altering the process conditions on the distribution of F-TS products is displayed in Table 2.9.

Table 2.9: The relationship between F-TS activity and product selectivity (Todic et al., 2016)

Parameter	**F-TS Product selectivity and conversion**				
Increase in parameter	**CO conversion**	**CH_4 selectivity**	**C_{5+} selectivity**	**Paraffin**	**Olefins**
Temperature	↑	↑	↓	↓	↑
Pressure	↑	↓	↑	↓	↑
H_2/CO	↑	↑	↓	↑	↓
Space velocity	↓	↑	↓	↓	↑

↑ = increase, ↓= decrease

2.13.1 The effect of reaction conditions on the F-TS process

A study by Todic et al. (2016) in which an iron catalyst was used to investigate the effect of temperature on the selectivity of hydrocarbons showed that as the reaction temperature increased, methane (CH_4) and C_2-C_4 selectivity increases (Figure 2.4), while C_{5+} selectivity decreases with increase in Temperature (Todic et al., 2016). Their results were consistent with literature studies in Table 2.9.

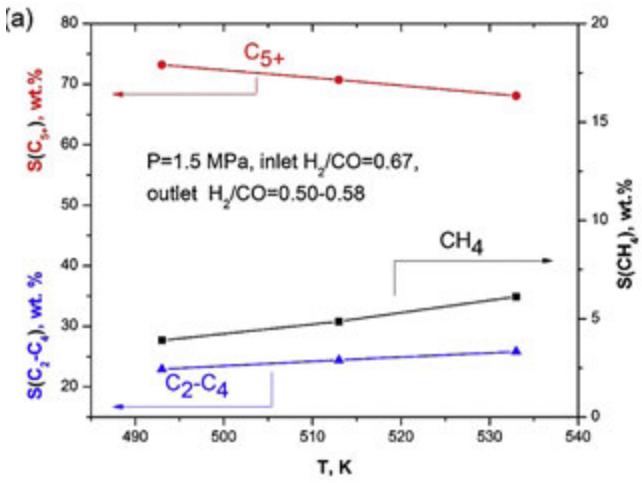

Figure 2.4: Effect of temperature on F-TS selectivity, reprinted with permission from (Todic et al., 2016)

Table 2.9 illustrates how C_{5+} selectivity and conversion of CO increase with increasing pressure. Savostyanov et al. (2015) reported that increasing the pressure to 6 MPa improved the conversion of CO and C_{5+}. Todic et al. (2016) investigated how hydrocarbons were affected by pressure. A range of total pressures, from 1.5 to 2.5 MPa, were used for the study. The findings shown in Figure 2.5 illustrate that as total pressure increased, C_{5+} selectivity increased while selectivity toward light products (methane and C_2-C_4) decreased (Todic et al., 2016).

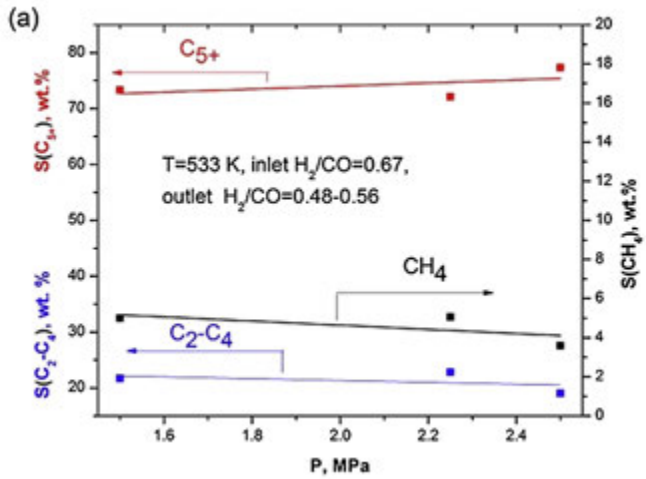

Figure 2.5: The effect of pressure on F-TS selectivity, reprinted with permission from (Todic et al., 2016)

Todic et al. (2014) investigated the effects of increasing the H_2/CO ratio on product selectivity using the Fe-Cu-K/SiO_2 catalyst. They discovered that increasing the H_2/CO ratio resulted an increase in CH_4, and a decrease in C_{5+} selectivity. Another study by Todic et al. (2016) investigated the effect of increasing the H_2/CO ratio on product selectivity. The results in Figure 2.6 illustrate that as the H_2/CO ratio increases, C_{5+} selectivity decreases, while the selectivity of light products (CH_4 and C_2-C_4) increases (Todic et al., 2016).

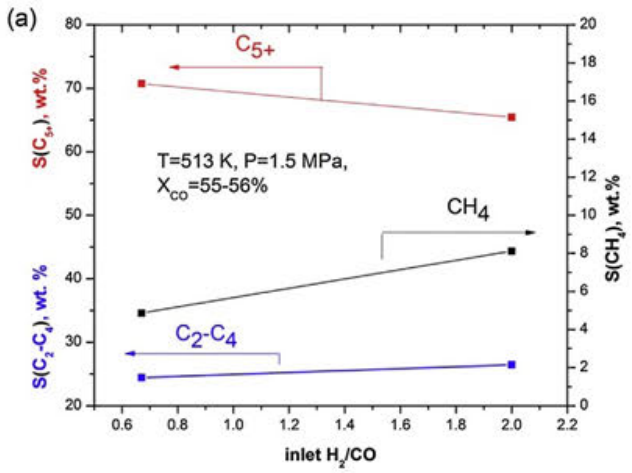

Figure 2.6: The effect of H_2/CO feed ratio on F-TS selectivity, reprinted with permission from (Todic et al., 2016)

2.13.2 Processes for the Fischer-Tropsch Synthesis

Commercial iron F-TS is conducted under high pressure and temperature. The two primary operating modes that are currently in use are high-temperature and low-temperature F-TS, which are dependent on the regime in which the procedure is implemented. In both operating modes, a pressure of 25 to 50 bar is applied (Saeidi et al., 2014).

2.13.2.1 Low Temperature F-TS (LTFT)

The average temperature in low-temperature F-TS mode is between 200 °C and 240 °C. Precipitated iron and cobalt catalysts are employed. This temperature range is used to produce linear waxes with a high molecular weight. The fixed bed and slurry bed reactors are utilized (Chun et al., 2020; Apolinar-Hernández et al., 2024).

2.13.2.2 High-Temperature F-TS (HTFT)

The typical temperature range in the high-temperature F-TS mode is between 300 °C and 350 °C. Catalysts are made of fused iron. Since cobalt catalysts have a high selectivity for methane formation, it is not ideal to use them at this temperature. Low-molecular-weight gaseous products such as olefins, paraffin, and gasoline are created in this temperature range. The main advantage of HTFT over LTFT is the lack of a liquid phase encircling the catalyst particles during the process (Chew et al., 2016). There is a variation in product distribution for the LTFF and HTFT processes as shown in Table 2.10.

Table 2.10: Product distributions for the LTFT and HTFT processes (Chabot et al., 2015)

LTFT	HTFT	Products (wt. %)
4	7	C_1
4	24	C_2-C_4 Olefins
4	6	C_2-C_4 Paraffins
18	36	Gasoline
19	12	Middle Distillate
48	9	Heavy Oils or Waxes
3	6	Oxygenates

2.14 Reactors in F-TS

Three types of reactors are used for F-TS, viz, fixed bed reactors, fluidized bed reactors, and slurry bed reactors (Chabot et al., 2015). These reactors differ primarily in how they handle the catalysts and reactants as explained in Figure 2.7, 2.8 and 2.9. Table 2.11 distinguishes these reactors in terms of products formed, activity, catalysts used, pressure, and temperature.

Table 2.11: Advantages and disadvantages of the types of reactors used in F-TS (Jacobs and Davis, 2016)

Ease of regeneration	Activity maintenance	Products	Catalyst	Pressure	Temperature	Operating Conditions
Very good	Fair	Light olefin	Co	N/A	190-260 °C	Slurry bed
Very good	Fair-Good	C_1-C_{15} and alpha-olefins	Fe	25 bar	300-350 °C	Fluidized bed
Poor	Good	Heavy hydrocarbon	Fe	20-30 bar	220-260 °C	Fixed bed

2.14.1 Fixed bed nuclear reactor (FBNR)

A fixed-bed reactor is a cylindrical tube that is filled with pellets of catalyst, allowing reactants to pass through and transform into products. A fixed-bed reactor usually has a downward flow. Low-pressure drops and reactor temperature control for exothermic reactions are the disadvantages of fixed-bed reactors (Mahura et al., 2019). Nuclear fixed bed reactor is the example of a fixed bed reactor as shown in Figure 2.7.

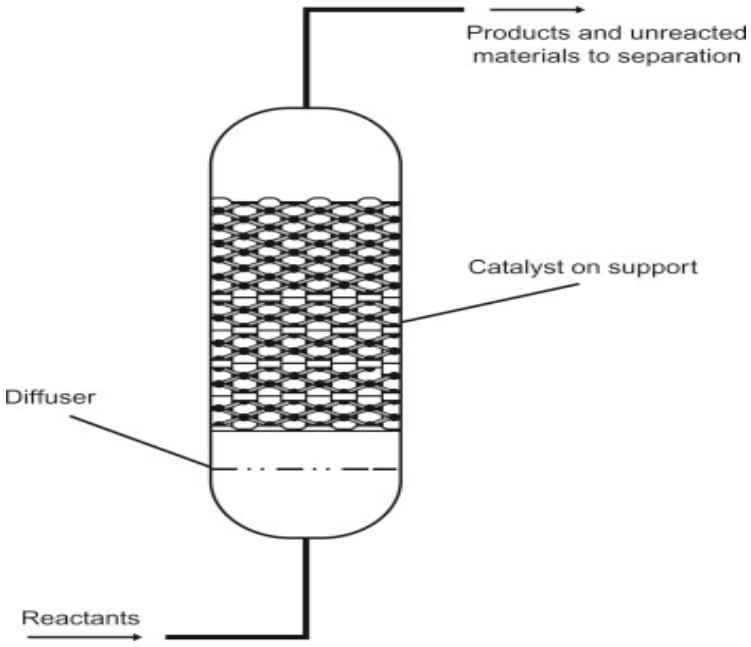

Figure 2.7: Fixed bed reactor, reprinted with permission from (Zhu, 2013)

2.14.2 Fluidized bed reactor (FBR)

Chemical processes involving multiple phases are typically conducted via fluidization. Little catalyst particles are suspended by the fluid as part of the reactor's upward motion as shown in Figure 2.8. Usually, the fluid is a gas that flows at a high enough rate to mix the catalyst particles inside the reactor without removing them. The reactor's bottom is where the reactants enter. This reactor's disadvantage is that there is a chance some catalyst powder will leak out on top (Chun et al., 2020).

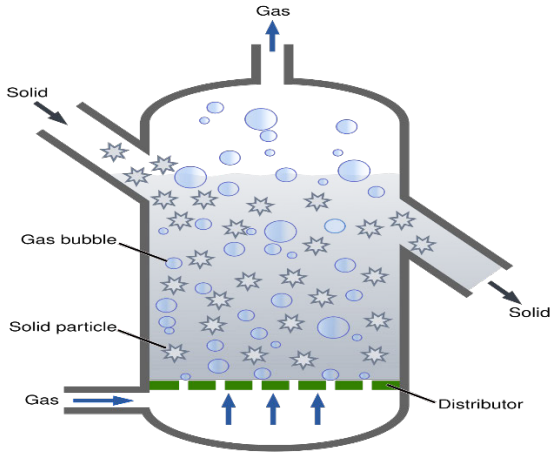

Figure 2.8: Fluidized bed reactor, reprinted with permission from (Mahura et al., 2019)

2.14.3 Slurry bed reactor (SBR)

To address certain shortcomings related to both fixed bed and fluidized bed reactors, a slurry bed reactor was developed (Meng et al., 2022). Slurry bed reactors have several benefits, including the ability to use a low H_2/CO syngas ratio, the liquid phase ability to efficiently remove reaction heat and control reaction temperature, high reactor and catalyst productivity, optimal conditions for catalyst regeneration, ease of construction, and low investment costs (Meng et al., 2022). F-TS has superior heat removal because it involves highly exothermic reactions. The reactor is preferred over other reactors used for F-TS reactions due to its simplicity in the regeneration and catalyst supply processes, its ability to regulate temperature well, and its ease of construction. The reactor's top is where the reactants enter. Catalyst particles with a size between 10 and 100 µm are typically permitted to be used in the reactor. The stir feature of this reactor ensures that the catalyst particles

and the reactor have good contact, and this is essential to obtain a good catalytic performance (Meng et al., 2022). The example of a slurry bed reactor is shown in Figure 2.8.

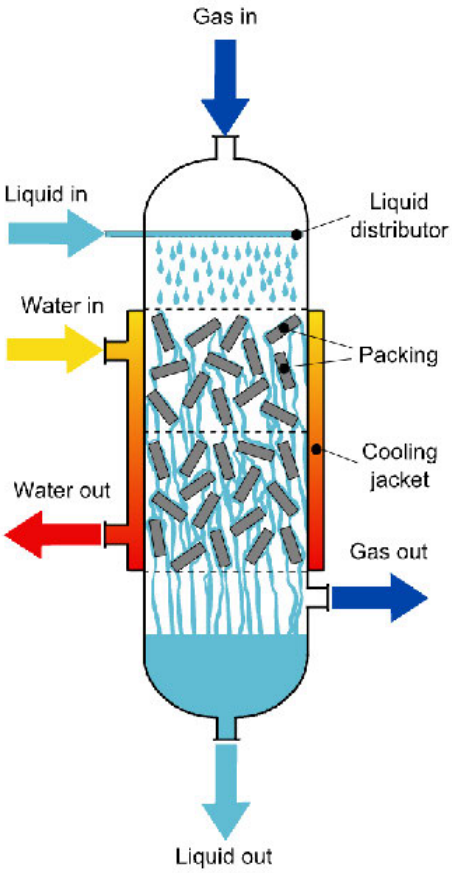

Figure 2.9: Slurry bed reactor, reprinted with permission from (Yun, 2023)

References

Anandharamakrishnan, C. 2015. Spray Drying Techniques for Food Ingredient Encapsulation (Book Review). John Wiley & Sons. *Chemical Engineering,* 77: 89-93.

Aghamohammadia, S, Hagigah, M.E. and Brahimi, A. A. 2019. Pathways in particle assembly by ultrasound-assisted spray-drying of kaolin/SAPO-34 as a fluidized bed catalyst for methanol to light olefins**.** *Ultrasonics – Sonochemistry,* 53: 237-239.

Arias, A.M. 2021. Spray-dried metal catalysts with tunable properties for fuel synthesis applications. PhD Thesis, Clausthal University of Technology.

Arsalanfara, A., Mirzaei, A.A., Bozorgzadehc, H.R. and Samimi, A. 2014. A Review of Fischer-Tropsch Synthesis on the Cobalt Based Catalysts*. Physical Chemistry Research*, 2(2): 179-201.

Apolinar-Hernández, J. E., Bertoli, S. L., Riella, H. G., Soares, C. and Padoin, N. 2024. An Overview of Low-Temperature Fischer–Tropsch Synthesis: Market Conditions, Raw Materials, Reactors, Scale-Up, Process Intensification, Mechanisms, and Outlook. *Energy & Fuels*, 38 (1): 1-28.

Bukur, D. B., Carreto-Vazquez, V., Pham, H. N. and Datye, A. K. 2004. Attrition properties of precipitated iron Fischer–Tropsch catalysts. *Applied Catalysis A: General*, 266 (1): 41-48.

Buthelezi, A.S., Tucker, C.L., Herees, H.J., Shozi, M.L., van de Bovenkamp, H.H. 2024. Fischer-Tropsch Synthesis using promoted, unsupported, supported, bimetallic and spray-dried iron catalysts: A review. *Results in Chemistry*,101623.

Barrios, A.J., Gu, B., Luo, Y., Peron, D.V., Chernaviskii, A.P., Virginie, M., Wojcieszak, R., Thybaut, J.W., Ordomsky, V.V. and Khodakov, A.Y. 2020. *Applied Catalysis B: Environmental*, 119028.

Choi, Y. H., Jang, Y. J., Park, H., Kim, W. Y., Lee, Y. H. and Choi, S. H. 2017. Carbon dioxide Fischer-Tropsch Synthesis: A new path to carbon-neutral fuels. *Applied Catalysis B: Environment*, 202: 605–610.

Chabot, G., Guilet, R., Cognet, P. and Gourdon, C. 2015. A mathematical modelling of catalytic milli-fixed bed reactor for Fischer-Tropsch Synthesis: Influence of tube diameter on Fischer-Tropsch Synthesis selectivity and thermal behavior. *Chemical Engineering Science*, 127: 72-83.

Chang, H., Cheng, M., Lin, Q., Zhu, J., Yijun, L. and Men Z. 2021. Effects of binder addition process parameters on physical, chemical, and catalytic performance of Fischer-Tropsch Synthesis catalyst. *Journal of China Coal Society*, 46(10): 3350-3356.

Chen, J., Zhao, Q., Han, X., Lin, J., Li, Z. Huang, S. and Ma, X. 2022. Extremely Low CO/H_2 Ratio Activation of a Precipitated Iron Catalyst for Enhanced Fischer-Tropsch Synthesis Performance. *Energy Fuels*, 36: 5384-5392.

Chen, W., Kimpel, T.F., Song, Y., Chiang, F.K., Zijlstra, B., Pestman, R., Wang, P. and Hensen, E.J.M. 2018. Influence of Carbon Deposits on the Cobalt-Catalyzed Fischer−Tropsch Reaction: Evidence of a Two-Site Reaction Model. *American Chemical Society,* 8 (2):1580-1590.

Cheng, K., Virginie, M., Ordomsky, V.V., Cordier, C., Chernavskii, P.A., Ivantsov, M.I., Paul, S., Wang, Y. and Khodakov, A.Y. 2015. Pore size effects in high-temperature Fischer–Tropsch Synthesis over supported iron catalysts. *Journal of Catalysis*, 328: 139–150.

Chew, L.W., Wei, X., Duddler, H., Weide, P. Ruland, H., Muhler M. 2016. On the role of the stability of functional groups in multi-walled carbon nanotubes applied as support in iron-based high-temperature Fischer-Tropsch Synthesis. *Catalysis Today*, 270: 85-92.

Chun, D.H., Rhim, G.B., Youn, M.H., Deviana, D. Lee, J.E., Park, J.C. and Jeong, H. 2020. Brief review of precipitated iron-based catalysts for low-temperature Fischer-Tropsch Synthesis. *Topics in Catalysis,* 63: 793-809.

Ding, M., Yang, Y., Li, Y., Wang, T., Ma, L. and Wu, C. 2013. Impact of H_2/CO ratios on phase and performance of Mn-modified Iron-based Fischer-Tropsch Synthesis catalyst. *Applied Energy*, 112: 1241-1246.

Gao, X., Zhigang, W., Ashok, J. and Kawi, S. 2020. A comprehensive review of anti-cocking, anti-poisoning, and anti-sintering catalysts for biomass tar reforming reaction. *Chemical Engineering Science,* 10: 65-67.

Gholami, Z., Gholami, F., Tisler, Z., Hubacek, J., Tomas, M., Baciak, M. and Vakili, M. 2022. Production of Light Olefins via Fischer-Tropsch Synthesis Process Using Iron-Based Catalysts. A review. *Catalysts*, 12(2): 174.

Goerge, S., Thomas, A., Kumar, M.V.P. and Komdod, A.S. 2023. Impact of processing parameters on the quality attributes of spray-dried powders: a review. *European Food Research and Technology,* 249(2): 241-257.

Guo, X., Lu, Y., Wu, P., Zhang, K., Liu, Q. and Luo, M. 2016. The effect of SiO_2 particle size on iron-based F-T synthesis catalysts. *Chinese Journal of Chemical Engineering,* 24(7): 937-943.

Iris, C. T. H. and Bert, M. Weckhuysen. 2021. The active phase in cobalt-based Fischer-Tropsch Synthesis. *Chemistry Catalysis*, 1(2): 339–363.

Jacobs, G., and Davis, B.H. 2016. Reactor approaches for Fischer-Tropsch Synthesis. *Multiphase Catalytic Reactors: Theory, Design, Manufacturing, and Applications*, 5: 269-294.

James, O.O., Chowdhurry, B., Mesubi, M.A. and Maity, S. 2012. Reflections on the chemistry of the Fischer-Tropsch Synthesis. Royal society of chemistry. *Royal Society of Chemistry Advances*,10: 25-33.

Kang, S.H., Bae, J.W., Cheon, J.Y., Lee, Y.J., Ha K.S., Jun, K.W., Lee, D.H. and Kim, B.W.2011. Catalytic performance of iron-based Fischer-Tropsch catalyst in fixed-bed and bubbling fluidized-bed reactor. *Applied Catalysis B: Environmental*, 103(2): 169-180.

Kukade, S., Kumar, P., Rao, P.V.C. and Choudary, N.V. 2016. Comparative study of attrition measurements of commercial FCC catalysts by ASTM fluidized bed and jet cup test methods. *Powder Technology,* 301: 427-477.

Li, C., Sayaka, I., Chisato, F. and Fujimo, K. 2016. Development of high-performance graphite-supported iron catalyst for Fischer-Tropsch Synthesis. *Applied Catalysis A: General*, 509: 123-129.

Li, J., Cheng, X., Zhang, C., Dong, W., Yong, Y. and Li, Y. 2016. Comparative study of iron-based Fischer-Tropsch Synthesis catalysts promoted with strontium or potassium. *Catalysis Letters*, 146: 2574-2584.

Li, J., Hou, Y., Song, Z., Liu, C., Dong, W., Zhang, C., Yang, Y. and Li, Y. 2018. Chemical and structural effects of strontium on iron-based Fischer-Tropsch Synthesis catalyst. *Molecular Catalysis*, 449: 1-7.

Li, J.B., Ma, H.F., Zhang, H.T., Sun, Q.W., Ying, Y.W. and Fang, D.Y. 2014. Sodium promoter on the iron-based catalyst for direct catalytic synthesis of light alkenes from syngas. *Fuel Processing Technology,* 125:119–124.

Li, W., Zhang X., Wang, T., Zhang, X., Wei, L., Lin, Q., Lv, Y. and Men, Z. 2022. The effect of chlorine modification of precipitated iron catalysts on their Fischer-Tropsch Synthesis properties. *Catalysts,* 12(8): 812-815.

Lin, Q., Cheng, M., Zhang, K., Li, W., Wu, P., Cheng, H., Lv, Y., Men, Z. 2021. Development of an Iron-based Fischer-Tropsch Catalyst with high attrition resistance and stability for industrial application. *Catalysts,* 11(8): 908.

Lin, T.J., Meng, X. and Shi, L. 2012. Attrition studies of an iron Fischer-Tropsch catalyst used in a pilot scale stirred tank slurry reactor. *Industrial & Engineering Chemistry Research*, 51(40): 13123-13131.

Liu, R., Ma, Z, Sears, J.D., Juneau, M., Neidig, M.L. and Porosoff, M.D. 2020. Identifying correlations in Fischer-Tropsch Synthesis and CO_2 hydrogenation over Fe-based ZSM-5 catalyst. *Journal of CO_2 Utilization,* 41: 101290.

Mahura, E., Rakereng, J. Rapoo, O. and Danha, G. 2019. Effect of the operation parameters on the Fischer-Tropsch Synthesis process using different reactors. *Procedia manufacturing,* 35: 349-355.

Mai, K., Elder, T., Groom, L.H., Spivey, J.J. 2015. Fe-based Fischer-Tropsch Synthesis of biomass-derived syngas: Effect of synthesis method. *Catalysis Communications,* 65: 76-80.

Meng, F. and Nawaz, M.A. 2022. Review of slurry bed rectors for carbon one chemistry. *Advances in Slurry Technology,* 12: 44-47.

Mohiuddin, E. 2011.The effect of microwave heating on manganese-promoted iron-based Fischer-Tropsch catalysts. MSc Thesis, University of the Witwatersrand.

Nandiyanto, A.B.D and Okuyama K. 2011. Progress in developing spray-drying methods to produce controlled morphology particles: From the nanometer to sub-micrometer size ranges. *Advanced Powder Technology,* 22(1): 1-19.

Nuzzo, M., Fureby, A.M. and Sloth, J. 2015. Surface Composition and morphology of particles dried individually and by spray drying. *Drying technology*, 33(6): 67-73.

Pendyala, V.R.R., Graham, U.M., Jacobs, G., Hamdeh, H.H., Davis, B.H. 2014. Fischer–Tropsch Synthesis: Morphology, Phase Transformation, and Carbon-Layer Growth of Iron-Based Catalysts. *ChemCatChem*, 6(7): 1952–1960.

Saadatkhah, N., Rigamonti, M.G., Boffito, D.C., Li, H. and Gregory, S. 2017. Spray dried SiO_2 WO_3/TiO_2 and SiO_2 vanadium pyrophosphate core-shell catalysts. *Powder Technology*, 316: 434-440.

Saeidi, S., Amiri, M.T.A., Amin, N.A.S. and Rahimpour, M.R. 2014. Progress in reactors for high temperature Fischer-Tropsch process: determination place of intensifier reactor perspective. *International Journal of Chemical Reactor Engineering*, 12(1): 639-664.

Savostyanov, I, V., Dorokhov, G.V., Makaryan, A, I. and Sedov, V.I. 2015. Slurry reactor system with inertial separation for Fischer-Tropsch Synthesis and another three-phase hydrogenation process. *The Canadian Journal of Chemical Engineering*, 94(3): 518-523.

Shafer, W.D., Gnanamani, M.K., Graham, U.M., Yang, J., Masuku, C.M., Jacobs, G., Davis, B.H. 2019. Fischer–Tropsch: Product Selectivity–The Fingerprint of Synthetic Fuels. *Catalysts,* 9(3): 259-262.

Szczap, J.P. and Jacobs, I.C. 2023. Atomization and spray drying processes. In: *Microencapsulation in the Food Industry*. 2nd ed. Elsevier, 59-71.

Teimouri, Z., Abatzoglou, N. and Dalai, A.K. 2021. Dalai. Kinetics and Selectivity Study of Fischer–Tropsch Synthesis to C_{5+} hydrocarbons: a review. *Catalysts,* 11(3): 330.

Todic, B., Nowicki, L., Nikacevic, N. and Bukur, D.B. 2016. Fischer-Tropsch Synthesis product selectivity over an industrial iron-based catalyst: Effect of process conditions. *Catalysis Today*, 261: 28-39.

Van Santen, R.A., Markvoort, A.J., Filot, I.A.W., Ghouri, M.M. and Hensen, E.J.M. 2013. Mechanism and microkinetics of the Fischer-Tropsch reaction. *Physical Chemistry and Chemical Physics*, 15(40): 17038-17063.

Xue, Y.Y., Zhai, Y.L., Chen, Z., Zhang, J.Q., Sun, J., Abbas, M., Chen, Y. and Chen, J.G. 2018. Sol-Gel Autocombustion Combined Carbothermal Synthesis of Iron-based Catalysts for Fischer-Tropsch Reaction. *ChemCatChem*, 10(4): 831-836.

Yun, 2023. Research on fluid dynamics behavior monitoring systems based on slurry bed reactor. *Highlights in Science, Engineering and Technology*, 35: 63-64.

Zamani, Y. 2015. Fischer-Tropsch synthesis over nano-sized iron-based catalysts. Investigation of Promoter and Temperature Effects on Product Distribution. *Petroleum and Coal*, 57: 71-75.

Zhang, H., Ma, H., Zhang, H., Ying, W. and Fang, D. 2012. Effects of Zr and K Promoters on Precipitated Iron-Based Catalysts for Fischer-Tropsch Synthesis. *Catalysis Letters*, 142: 131-137.

Zhang, H., Zhang, H., Qian, W., Wu, X., Ma, H., Sun, Q. and Ying, W. 2022. Sodium-modified Fe-Mn microsphere catalyst for Fischer–Tropsch Synthesis of light olefins. *Catalysis Today,* 389: 199–207.

Zhang, K., Miao, P., Zhang, H. Wang, Y., Wang, G., Zhu, X. and Li, C. 2021. Research on ethylbenzene dehydration over the Fe-Al-based catalysts in a circulating fluidized-bed unit. *Journal of the Taiwan Institute of Chemical Engineers,* 128: 55-63.

Zhang, Y., Ma, L., Wang, T. and Li, X. 2015. Synthesis of Ag-promoted porous Fe_3O_4 microspheres with a tunable pore size as catalysts for Fischer–Tropsch production of lower olefins. *Catalysis Communications*, 64: 32-36.

Zhang, Y., Ma, L., Wang, T. and Li, X. 2016. MnO_2-coated Fe_2O_3 spindles are designed to produce C_{5+} hydrocarbons in Fischer–Tropsch synthesis. *Fuel*, 177: 197–205.

Zhang, Y., Maa, L., Tua, J., Wanga, T. and Li, X. 2015. One-pot synthesis of promoted porous iron-based microspheres and its Fischer–Tropsch performance. *Applied Catalysis A: General,* 499: 139–145.

Zhao, M., Cuia, Y., Sunb, J., and Zhan, Q. 2018. Modified iron catalyst for direct synthesis of light olefin from syngas. *Catalysis Today*, 316: 142-148.

Zhao, X., Lv, S., Wang, L., Li, L., Wang, G, Zhang, Y. and Li, J. 2018. Comparison of preparation methods of iron-based catalysts for enhancing Fischer-Tropsch Synthesis performance. *Molecular Catalysis,* 499: 99-105.

Zhu, X., 2013. A study of radial heat transfers in fixed bed Fischer-Tropsch synthesis reactors (Doctoral dissertation). University of Witwatersrand.

CHAPTER 3: EXPERIMENTAL METHODS

Synthesis methods (co-precipitation, impregnation and spray-drying) used to prepare the iron-based catalysts are discussed. Catalysts were characterized using a variety of techniques, which are described in detail. These techniques included X-ray fluorescence (XRF), X-ray diffraction (XRD), Brunauer-emmett-teller (BET) Analysis, scanning electron microscopy (SEM), and Thermogravimetric analysis (TGA). A detailed explanation is given for both the attrition test method and the catalyst testing method for Fischer-Tropsch Synthesis.

3.1 Chemical and Materials

Every chemical used in this study, including Fe $(NO_3)_3.9H_2O$ (>98%), Cu $(NO_3)_2.3H_2O$ (>99.5%), Na_2CO_3 (>99.5%), K_2CO_3 (99.5%), $C_6H_5CH_3$ (99.8%), $C_6H_4(CH_3)_2$ (97%), and CH_3CH_2OH (>98%), were purchased from Sigma-Aldrich in Germany. Distilled water was used for the preparation of solutions. The materials purchased were used without further purification.

3.2 Catalysts preparation

3.2.1 Preparation of the α-Fe_2O_3 catalyst

The catalyst was synthesized using the co-precipitation method. 25.0 g of Fe $(NO_3)_3.9H_2O$ was dissolved in 100 mL of distilled water. The solution was precipitated with sodium carbonate solution (25.0 g in 100 mL of water) by adding drops while vigorously stirred. The solution was then heated to 70 °C. A pH of 7 was achieved by filtering and washing the resultant precipitate with distilled water. The catalyst was calcined in air at 500 °C for 6 hours at a heating rate of 5 °C/min after being dried overnight at 100 °C (Xu et al., 2014).

3.2.2 Preparation of K/Cu/Fe catalyst by impregnation method

The catalyst was synthesized using the co-precipitation and impregnation methods. 25.0 g of Fe $(NO_3)_3.9H_2O$ and 1.5 g of Cu $(NO_3)_2.3H_2O$) were dissolved in 100 mL of distilled water. The solution was precipitated with sodium carbonate solution (25.0 g in 100 mL of water) by adding drops while vigorously stirred and heated to 70 °C. A pH of 7 was achieved by filtering and washing the resultant precipitate with distilled water. The precipitate was then dried at 100 °C overnight. 0.21 g of K_2CO_3 and dried precipitate (Cu/Fe) were dissolved in 200 mL of deionized water and the solution was stirred for 2 hours. The solution was then rotatory evaporated at 110

°C to remove the solvent. The catalyst was calcined in air at 500 °C for 6 hours at a heating rate of 5 °C/min after being dried overnight at 100 °C (Xu et al., 2014). Atomic ratios of K: Fe = 0.05 and Cu: Fe = 0.10 were achieved.

3.2.3 Preparation of the spray dried iron catalyst (0.367 M K/Cu/Fe spray-dried at 200 °C)

The spray-dried catalyst was synthesized using the co-precipitation method and the spray-drying technique. 25.0 g of Fe $(NO_3)_3.9H_2O$ and 1.5 g of Cu $(NO_3)_2.3H_2O$) were dissolved in 100 mL of distilled water. The solution was precipitated with a sodium carbonate solution (25.0 g in 100 mL of water) by adding drops while vigorously stirred and heated to 70 °C. A pH of 7 was achieved by filtering and washing the resultant precipitate with distilled water. 200 mL of deionized water was then added and approximately 0.21 g of K_2CO_3 were added to the cake to form a slurry solution which was spray-dried at 200 °C. The catalyst was further dried overnight at 100 °C and calcined in air at 500 °C for 6 hours at a heating rate of 5 °C per minute (Xu et al., 2014; Lin et al., 2021). Atomic ratios of K: Fe = 0.05 and Cu: Fe = 0.10 were achieved. The diagram that summarizes the spray-dried iron catalysts' preparation process is displayed in Figure 3.1.

The aspirator was set to 0.71%, and the speed of the pump to 0.07% during the spray-drying of the catalysts. To increase the particle size of the catalysts, a slurry solution for each catalyst was optimized by varying temperatures between 140 °C and 200 °C and concentrations of the iron precursor [Fe^{3+}] between 0.367 M and 1.101 M as shown in Table 3.2.

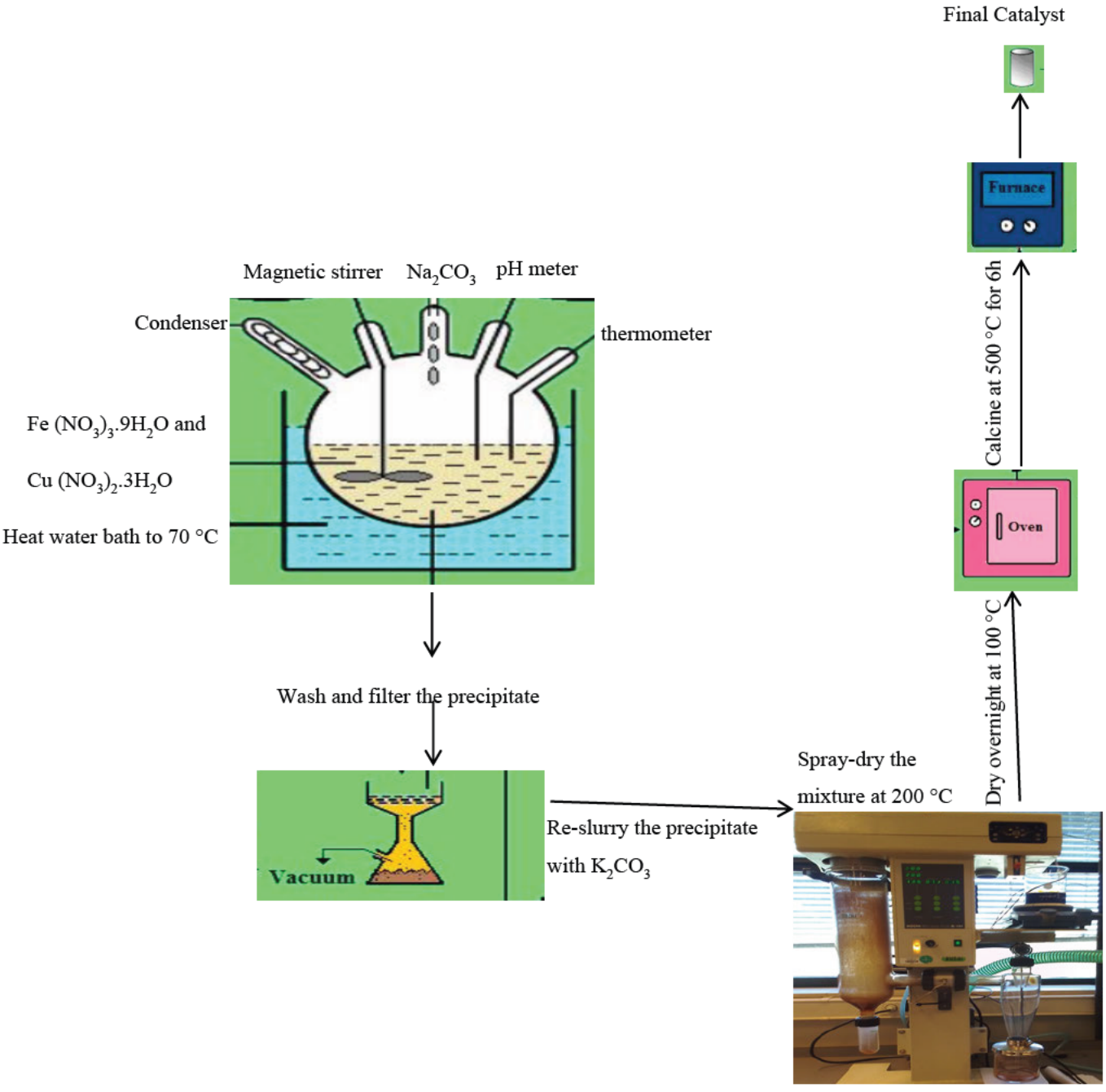

Figure 3.1: Summary of the preparation method of iron catalysts

The amounts of the precursors of iron catalysts used in the procedure (3.2) was calculated as shown in Table 3.1. Na_2CO_3 (sodium carbonate) was chosen and used as a precipitating agent in the co-precipitation method and removed by washing the formed precipitate with water. Cu (copper) and K (potassium) were selected and used as promoters.

Table 3.1: Calculated amount of the precursor salts used for the preparation of the catalysts

Precursor	Mass of precursor (g)	Promoter	Calculated mass of promoter (g) per 100 g Fe
$Fe(NO_3)_3.9H_2O$	25		
$Cu(NO_3)_2.3H_2O$	1.5	Cu	0.1
Na_2CO_3	25		
K_2CO_3	0.21	K	0.05

3.3 Optimization of spray-drying conditions

The two parameters, such as temperature and slurry concentration of iron catalysts, were varied to investigate the effect of changing spray-drying conditions on the attrition resistance, surface area, and morphology (size and shape) of the iron catalysts. The aspirator and speed of the pump were kept constant. The range of each parameter is listed in Table 3.2. The seven spray-dried samples were enough to conduct the investigation.

Table 3.2: The optimization of spray-drying parameters for the preparation of iron catalysts

Catalysts	Spray-dying conditions		
	Temperature (°C)	Aspirator (%)	Speed of the pump (%)
0.367 M K/Cu/Fe	140	0.71	0.07
0.734 M K/Cu/Fe	140	0.71	0.07
1.101 M K/Cu/Fe	140	0.71	0.07
1.101 M K/Cu/Fe	155	0.71	0.07
0.367 M K/Cu/Fe	200	0.71	0.07
0.734 M K/Cu/Fe	200	0.71	0.07
1.101 M K/Cu/Fe	200	0.71	0.07

3.4 Catalyst characterization

3.4.1 X-ray fluorescence

Using a PANalytical Epsilon 3XLE instrument, X-ray fluorescence (XRF) was used to perform the elemental analysis. Typically, samples were transferred to a plastic cup and assuming that the elements are in their oxide form, the amounts of each element were calculated (Pour, 2023).

3.4.2 X-ray diffraction

Using a Cu-K α radiation source (λ = 1.584 Å, generated at 40 Kv and 40 mA), a Bruker D8 Advance X-ray diffractometer was used to perform powder XRD. The scan range used was 10–80° (Pour, 2023).

3.4.3 Scanning Electron Microscopy

The elemental composition was ascertained by combining SEM with energy-dispersive (EDS). The LEO1450 scanning electron microscope was used to capture the images. The samples were coated with gold using a Polaron SC sputter coater before images were taken.

3.4.4 Brunauer-Emmet-Teller analysis

A micromeritics ASAP 2420 was used to measure the physisorption of nitrogen at -196 °C. The samples were degassed in a vacuum for ten hours at 350 °C before analysis. The specific surface area was measured using the BET model, and the pore size distribution on the physisorption curve was computed using the Barret-Joyner-Halenda (BJH) model (Pour, 2023; Yin, 2017).

3.4.5 Thermogravimetric analysis

A TGA/DSC STAR^e system (METTLER TO LEDO) was used to perform thermogravimetric analysis, with nitrogen serving as the purge gas and a heating rate of 10 °C /min. Prior to analysis, the samples were weighed on a balance and then put into a 70 µl aluminum oxide crucible. The TGA apparatus's balance was used to suspend the crucible, and then the furnace was raised to cover the balance. The temperature of the TGA was set to ramp from 25 °C to 800 °C while air atmosphere (O_2) was flowing through it.

3.5 Catalytic testing

The performance of the catalysts was evaluated using a slurry bed reactor shown in Figure 3.2. In each experimental run, a quantity of 40 g of wax was precisely measured and subsequently melted in a beaker placed on a hot plate. Following this, 1 g of the catalyst was thoroughly mixed with molten wax as it was stirred at 900 RPM within the reactor. Before conducting the F-TS tests, the catalysts were reduced at H_2/CO = 2:1 syngas, 265 °C, 20 bar, and a gas hourly space velocity of 4000 mL/(g-cat·h) for a duration of 20 hours. Once the reduction was complete, the temperature of the reactor was adjusted to 260 °C for the F-TS reaction. The liquid products generated during the reaction were collected in both a cold trap and a hot trap, respectively. The gaseous products' selectivity and the conversion of CO were obtained using a gas chromatograph. The gaseous products (N_2, CO, CO_2 and CH_4) were analyzed using a thermal conductivity detector and the hydrocarbons (C_1 to C_5) were assessed using a flame ionization detector (Lin et al., 2021).

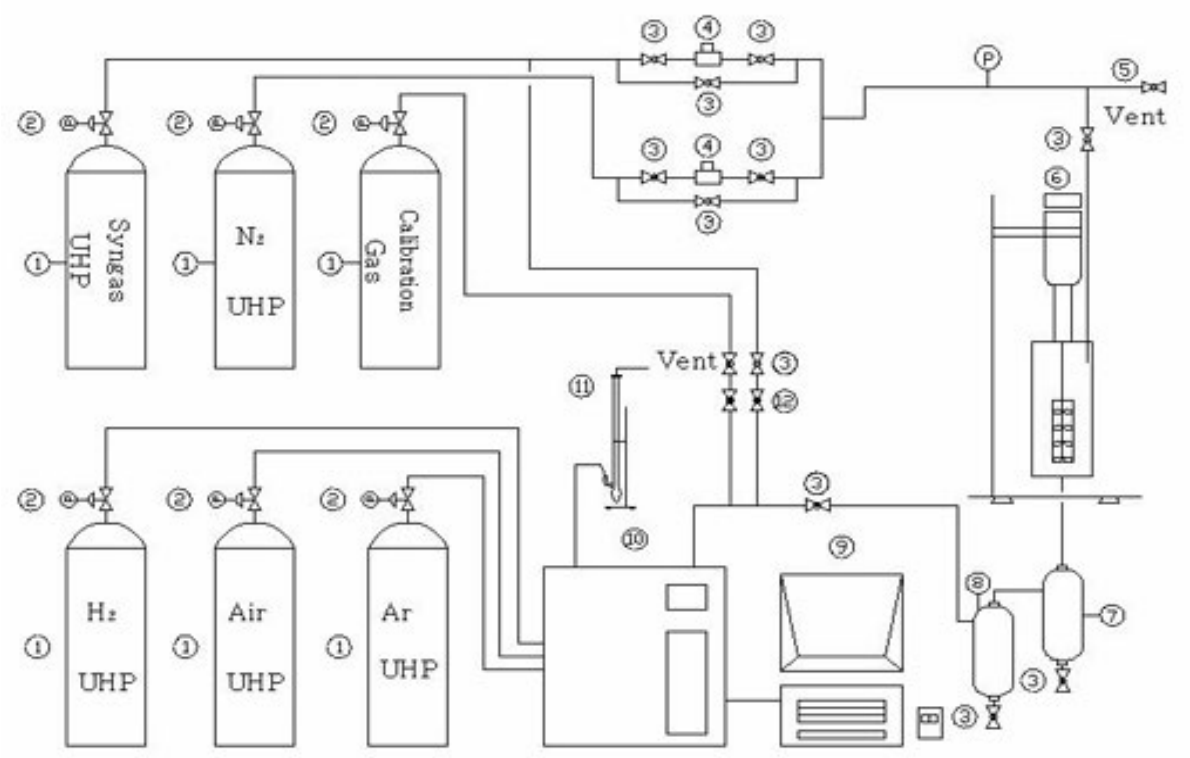

No. tags: (1). gas cylinders; (2). controllers; (3). closed valves; (4). mass flow regulators; (5). outlet valve; (6). constant stirring tank reactor; (7). wax trap; (8). liquid trap; (9). Collection of data; (10). gas chromatograph; (11). Flow meter; (12). no return valve

Figure 3.2: Similar type of slurry bed reactor (SBR) used for catalyst testing, reprinted with permission from (Lu, 2021)

3.6 Attrition resistance test

As illustrated in Figure 3.3, the ASTM D5757 method was used to evaluate the iron catalysts' attrition rate. In a fluidized bed setting, 5 g of each sample was loaded into the attrition tube at room temperature for one hour at a flow rate of 8 L/min and an atmospheric pressure of 6 bar. A thimble filter placed at the ASTM chamber's exit was used to collect the smaller particles. The weight percentage of lost particles of smaller size were calculated by dividing the weight of the collected particles of smaller size by the weight of the sample loaded to the attrition tube (Duvenhage et al., 2014).

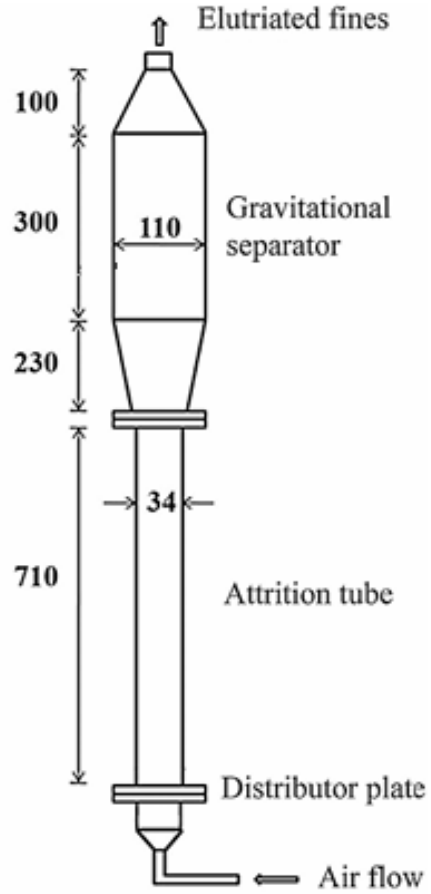

Figure 3.3: Apparatus designed according to the accredited standard method of testing materials (ASTM) used for measuring the attrition resistance of the iron catalysts, reprinted with permission from (Kukade et al., 2016)

References

Duvenhage, D.J., Schmidt, C. and Wright, W.H. 2014. Precipitated iron Fischer-Tropsch catalyst manufacturing: Impact of Hematite. *Journal of Material Science*, 49: 2810-2823.

Lu, X., 2011.Fischer-Tropsch synthesis: towards understanding. PhD thesis. University Witwatersrand.

Pour, Z. A. 2023. Synthesis and Catalytic Application of Macroscopic Zeolite Beads with Hierarchical Porosity. PhD Thesis, University of Groningen.

Xu, K., Sun, B., Lin, J., Wen, W., Pei, Y., Yan, S., Qiao, M., Zhang, X., Zong, B. 2014. Iron carbide as a low-temperature Fischer-Tropsch Synthesis catalyst. *Nature Communications*, 5(1): 57-83.

Yin, W. 2017. Catalytic hydrotreatment of pyrolysis liquids and fractions: Catalyst Development and Process Studies. PhD Thesis, University of Groningen.

CHAPTER 4: RESULTS AND DISCUSSION

4.1 Characterization

4.1.1 X-ray fluorescence

The elemental composition of the catalysts was determined using XRF assuming that the elements are in their oxide form. The results obtained are summarized in Table 4.1. The composition of the catalysts observed from the XRF corresponds to the values in the synthesis solutions, with values slightly higher and lower in some cases. The results show that the co-precipitation, impregnation and spray-drying technique were efficient for the preparation of the iron catalysts.

Table 4.1: Elemental composition of the catalysts

		Loading of metal oxides observed from the XRF (wt%)		
Catalysts	**Loadings of metal oxides (wt%)**	**K_2O**	**CuO**	**Fe_2O_3**
α-Fe_2O_3	99.6%Fe_2O_3	-	-	99.3
0.367 M K/Cu/Fe spray-dried @ 200 °C	5%K_2O/10%CuO/85% Fe_2O_3	4.4	8.8	84.5
K/Cu/Fe	5%K_2O/10%CuO/85% Fe_2O_3	4.2	8.9	89.2

4.1.2 X-ray Diffraction

XRD was used to evaluate the catalysts phase composition. Figure 4.1 shows the XRD patterns of the catalysts after the reaction (recovered or spent catalysts). After catalysts testing, the materials were dissolved in a hot xylene, filtered to separate them from wax and calcined at 500 ° C to further remove wax, xylene and other organic compounds. The catalysts were then characterized by XRD and three phases of iron were observed from, which are Fe_2O_3, Fe_3O_4, and χ-Fe_5C_2. The results of the spent catalysts were interpreted by comparing with the ones from literature studies. The Fe_2O_3 appeared 2θ = 24.2°, 33.23°, 35.7°, 49.5°, 54.2°, 62.5°, and 64.0° while Fe_3O_4 phase appeared at 2θ = 30.4° and 57.1° and the χ-Fe_5C_2 phase appeared at 2θ = 40.9° and 44.3° (Ge et al., 2019; Ouyang et al., 2015).

In comparing the XRD patterns of 0.367 M K/Cu/Fe spray-dried @ 200 °C recovered and α-Fe_2O_3 recovered catalysts, they both underwent phase change to produce Fe_3O_4 and χ-Fe_5C_2 phases. The difference is that the 0.367 M K/Cu/Fe spray-dried @ 200 °C underwent more phase change

because there are few diffraction peaks of Fe_2O_3 observed from the XRD, meaning that the Fe_2O_3 phase in the catalyst was mostly transformed into other phases of iron. In the α-Fe_2O_3 recovered catalyst, there are more of the diffraction peaks of Fe_2O_3 phase observed from the XRD, meaning that the catalyst underwent less phase change. Phases changes in the catalyst contribute to the chemical attrition. These results confirm that the α-Fe_2O_3 recovered catalyst is more chemically attrition resistant as compared to the 0.367 M K/Cu/Fe spray-dried @ 200 °C recovered catalyst. The average crystallite sizes of the catalysts were calculated using the Debye–Scherrer equation:

$$D_{Scherrer} = \frac{K\lambda}{\beta cos\theta} \qquad \text{Equation 4.1}$$

Where $D_{Scherrer}$ is the average crystallite size, λ is the wavelength of the X-ray radiation (λ = 0.154056 nm), K is the Scherrer constant (K = 0.89), β is the corrected band broadening (full width at half maximum) (FWHM), and θ is the diffraction angle (Deng et al., 2013).

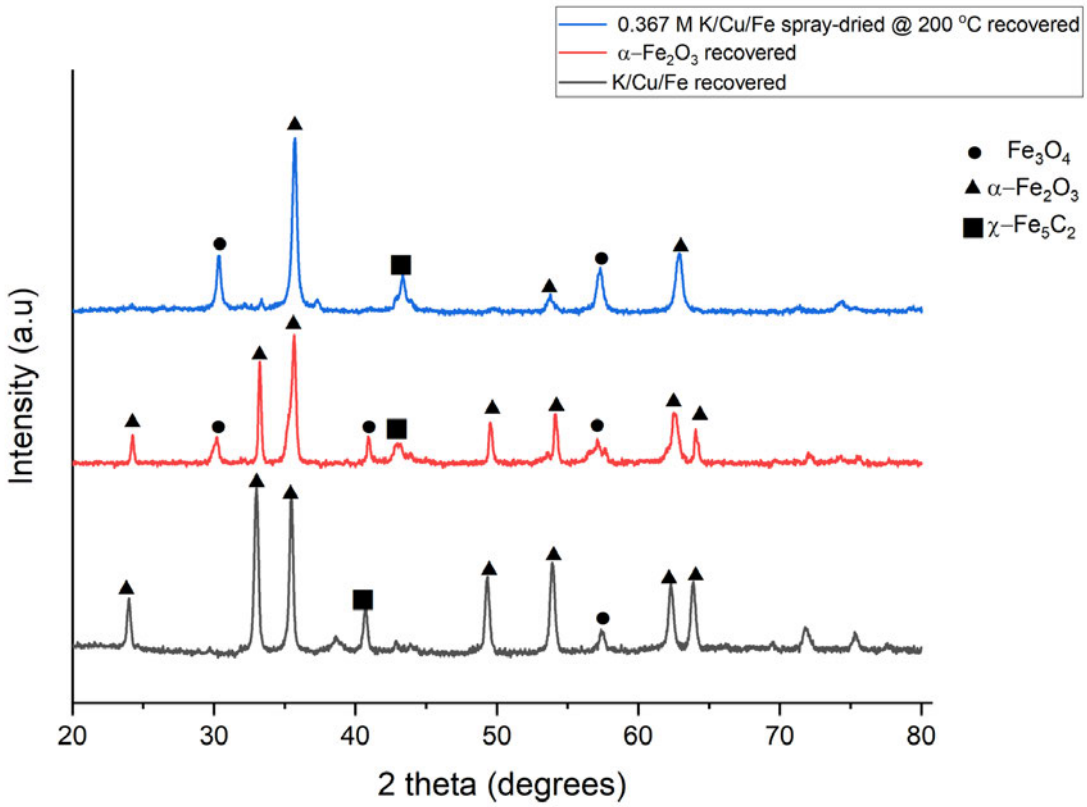

Figure 4.1: XRD patterns of iron catalysts after the F-TS reaction (spent catalysts), α-Fe_2O_3 recovered, K/Cu/Fe recovered and 0.367 M K/Cu/Fe spray-dried @ 200 °C recovered catalysts

Table 4.2 further shows the information obtained from Figure 4.1 by displaying the crystallite size and the degree of crystallinity observed for the iron catalysts. The 0.367 M K/Cu/Fe spray-dried at 200 °C catalyst showed a high degree of crystallinity of 55% and small crystallite size of 5.08 nm. The spray-drying technology produces high crystalline materials due to the rapid evaporation and subsequent cooling of droplets, which promotes the formation of ordered crystal structures. This is the reason for the 0.367 M K/Cu/Fe spray-dried at 200 °C catalyst showing high degree of crystallinity (Das and Langrish, 2012). The degree of crystallinity obtained in this study is less than the one obtainedin literature, which is 72%. It should be noted that in literature, a different type of spray-drying technique (pilot-scale spray dryer) and conditions, were used, while a mini spray dryer was used in this study. On the other hand, the K/Cu/Fe and α-Fe_2O_3 catalysts showed low and roughly a similar degree of crystallinity of 34% and 30%. Although the degree of crystallinity displayed by these catalysts was low, they showed high crystallite sizes of 8.56 nm and 9.32 nm. The smaller the crystallite size, the higher the degree of crystallinity, whereas the

larger the crystallite sizes, the lower the degree of crystallinity, as shown in Table 4.2. This could be attributed to factors such as surface energy. Compared to bigger crystallites, smaller ones contain more high-surface-energy atoms per unit volume. The surface atoms had an increased ability to arrange themselves in a more ordered, crystalline form as a result of the enhanced surface energy of the small crystallites (Nandiyanto et al., 2023).

Table 4.2: The summary of XRD average crystallite size and degree of crystallinity for the catalysts

Catalysts	Average crystallite size (nm)	Degree of crystallinity (%)
α-Fe_2O_3	9.32	30
0.367 M K/Cu/Fe spray-dried @ 200 °C	5.08	55
K/Cu/Fe	8.56	34

4.1.3 Brunauer-Emmet-Teller analysis

BET was used to determine the surface area of the catalysts, pore volume and pore size. According to the results in Table 4.3, the spray-dried iron catalyst exhibited a high surface area, smaller pore volume, and pore size of 39 m^2/g, 0.16 cm^3/g, and 13.2 nm, respectively, as compared to other catalysts. This shows that the use of the spray-drying technique improves the surface area of iron catalysts. Although the addition of promoters increases both activity and selectivity of a catalyst, they can produce particles that block the pores of a catalyst. This pore blocking reduces the surface area accessible for adsorption and reaction (Milburn, 1996). The addition of the potassium promoter decreased the pore volume of both K/Cu/Fe and 0.367 M K/Cu/Fe spray-dried @ 200 °C. The presence of alkali or alkaline-earth metals appears to impede crystallization during heating. The α-Fe_2O_3 catalyst exhibited the second highest surface area, with a high pore volume and pore size of 26 m^2/g, 0.18 cm^3/g and 23.8 nm. The pore size, pore volume, and surface area of the K/Cu/Fe catalyst are 22.8 nm, 0.16 cm^3/g, and 25 m^2/g, respectively. The results show that the measurement of attrition resistance affected the physical properties of the catalysts. It was observed that there was a change in the physical properties of iron catalysts after they were tested for attrition resistance and characterized using BET. All the iron catalysts showed an increase in surface area, pore volume, and pore size as compared to the original catalysts. This could be

attributed to the fragmentation of the particles. The particles break down as they collide with the walls of the ASTM apparatus during the physical attrition test, and this resulted in an increase in surface area, pore volume, and pore size.

Table 4.3: The physical properties of the catalysts

Catalysts	Surface area (m^2/g) before attrition	Surface area (m^2/g) after attrition	Pore volume (cm^3/g) before attrition	Pore volume (cm^3/g) after attrition	Pore size (nm) before attrition	Pore size (nm) after attrition
α-Fe_2O_3	26	30	0.18	0.22	23.8	24.9
0.367 M K/Cu/Fe spray-dried @ 200 °C	39	40	0.16	0.20	13.2	22.6
K/Cu/Fe	25	28	0.16	0.20	22.8	31.5

Figure 4.2 shows the BET N_2 adsorption and desorption isotherms of the catalysts. Based on the hysteresis loop in the relative pressure region around (P/Po= 0.68-0.90) indicated that all the catalysts exhibit type IV curves as shown in Figure 4.2. Additionally, the catalysts displayed comparable pores based on the same hysteresis loops. An H_1-type hysteresis loop, which is typical of cylindrical pores, was present in all the catalysts. Furthermore, there is a slight difference in the shape from Figure 4.2 which may be ascribed to the quantity of the gas adsorbed.

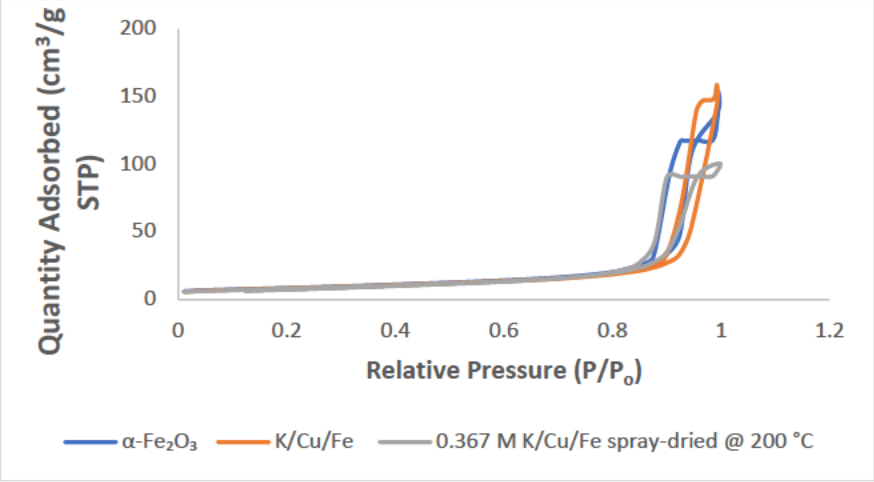

Figure 4.2: N_2 Adsorption-desorption isotherms for the α-Fe_2O_3, K/Cu/Fe and 0.367 M K/Cu/Fe spray-dried @ 200 °C catalysts

4.1.4 Scanning Electron Microscopy

The image J software was used to calculate the particle size from the SEM images. Figure 4.3 (A) shows that the spray-dried catalyst (0.367 M K/Cu/Fe spray-dried at 200 °C) consists of particles that are spherical in shape, with approximately 1-2 µm in size, making the catalyst not suitable for the industrial application where a 100 µm particle size is typical (Okwonna et al., 2019). On the other hand, Figures 4.3 (A) and (B) show that α-Fe_2O_3 and K/Cu/Fe catalysts consist of small spherical shaped particles with a size that is approximately 0.2 µm. It can be observed that the surface looks rough where the 0.367 M K/Cu/Fe spray-dried at 200 °C catalyst particles are placed, and this is because the catalyst showed a high surface area of 39 m^2/g as compared to the other catalysts as shown by the BET results in Table 4.3. Materials with high surface area due to their porous structure might be visible as having a rough surface with many pores (Ali et al., 2023).

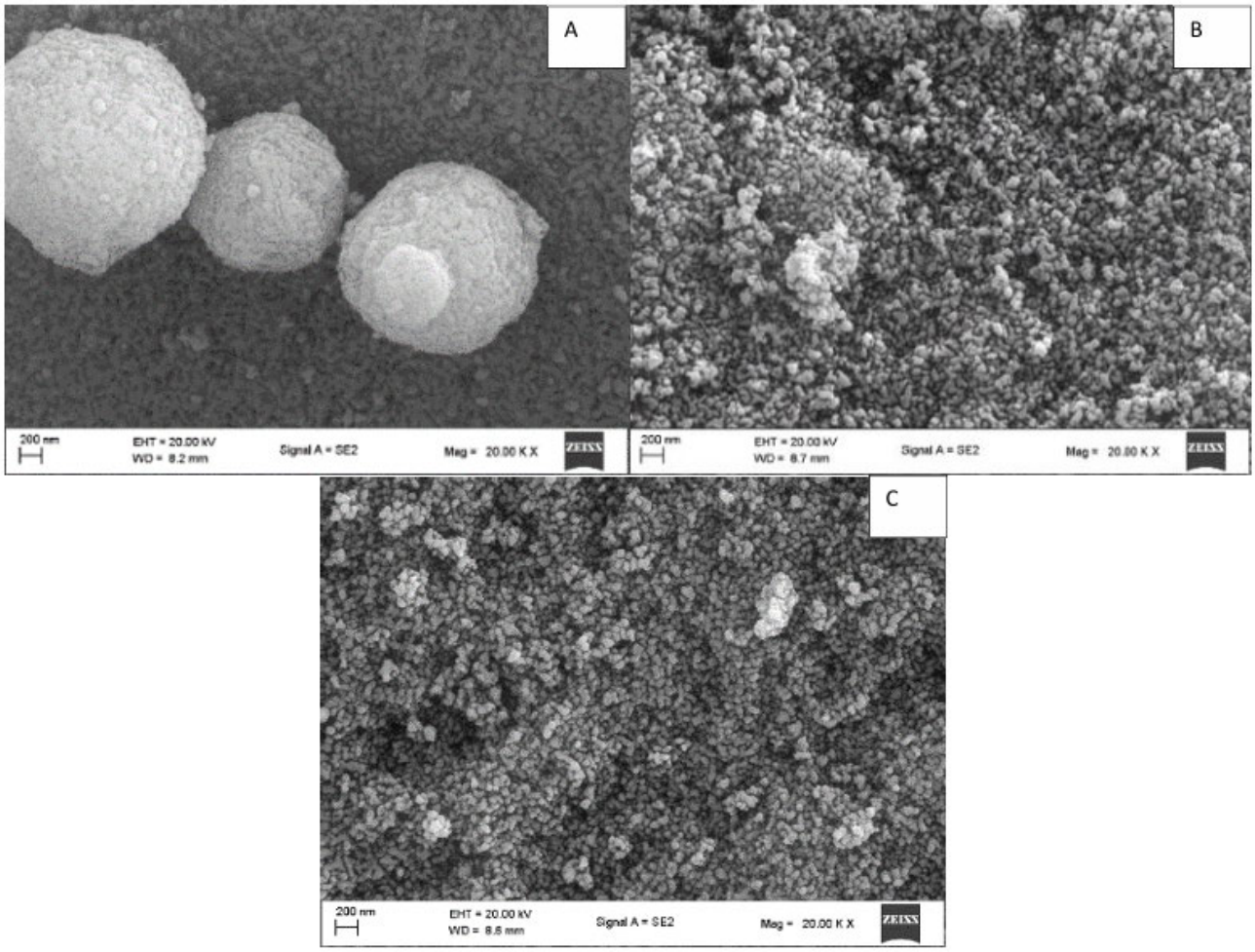

Figure 4.3: SEM images of (A) 0.367 M K/Cu/Fe spray-dried @ 200 °C, (B) α-Fe_2O_3 and (C) K/Cu/Fe iron catalysts

Adeyiga (2003) freported that the distribution of each element in the catalysts helps to get a better understanding of the factors influencing attrition resistance (Adeyiga, 2003). SEM-EDS analysis showed that the 0.367 M K/Cu/Fe spray-dried @ 200 °C and K/Cu/Fe catalysts are composed of Fe, Cu, K, O, and C elements, as shown in Figure 4.4. The results of elemental mapping in Figure 4.5 further confirm that the α-Fe_2O_3 and other catalysts show Fe, Cu, K, O, and C elements. Carbon is an impurity that was found present in all the catalysts, which is likely from the CO_2 which was confirmed on the TGA results. Furthermore, all the elements, including Fe, Cu, K, O, and C, were found to be uniformly distributed throughout the catalyst particles, indicating that a homogeneous composition was achieved from the catalysts, as shown in Figure 4.5.

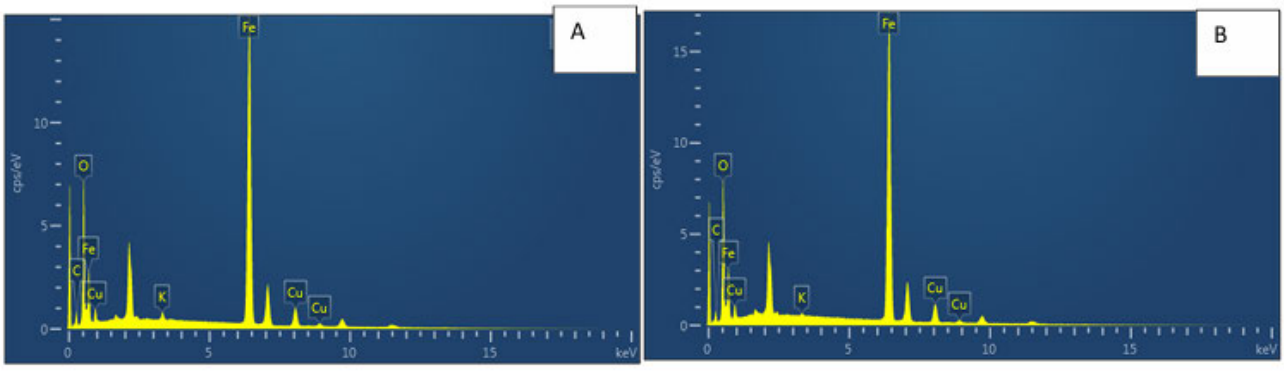

Figure 4.4: SEM-EDS analysis of (A) 0.367 M K/Cu/Fe spray-dried @ 200 °C and (B) K/Cu/Fe iron catalysts

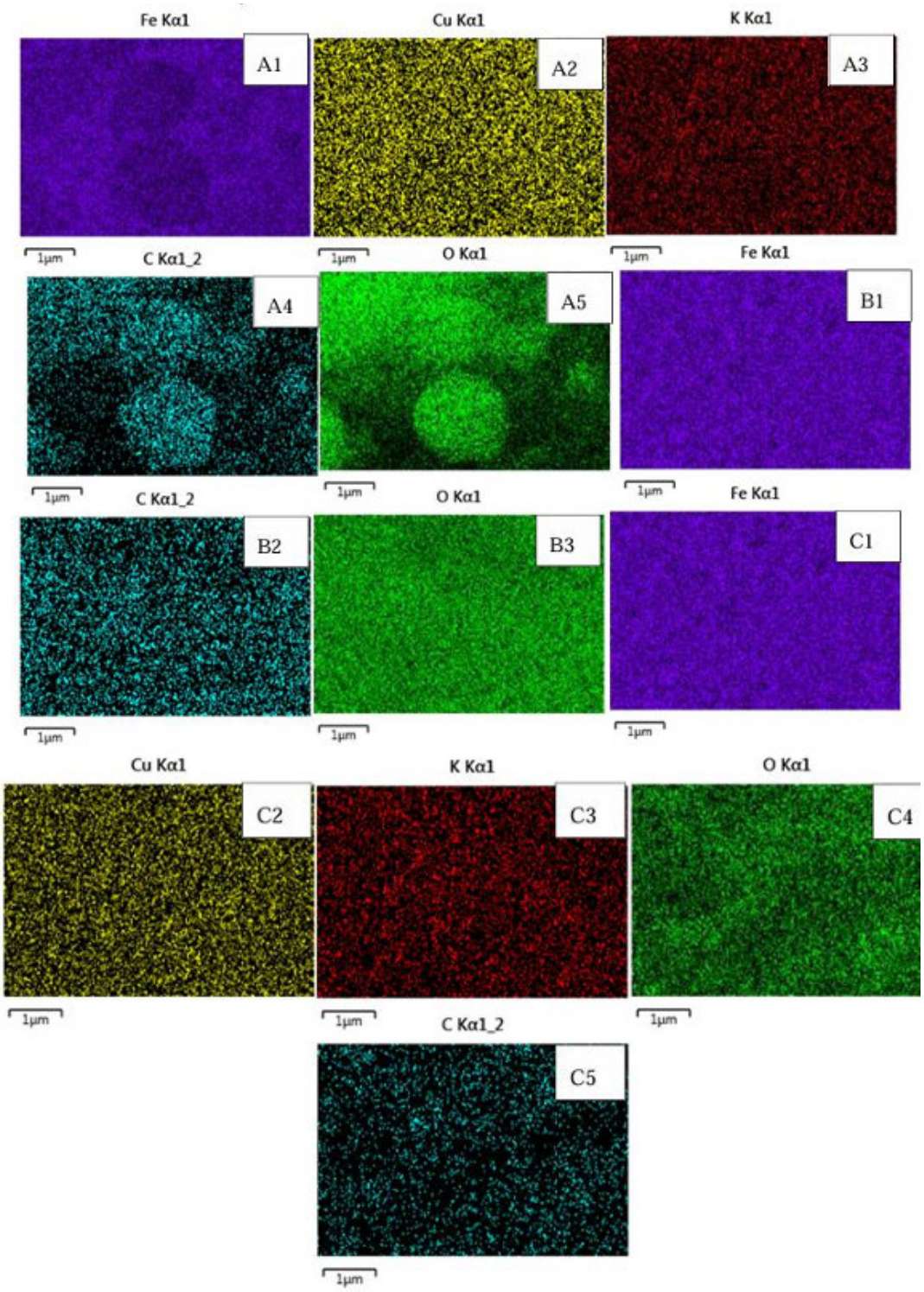

Figure 4.5: Elemental mapping analysis of (A1-A5) 0.367 M K/Cu/Fe spray-dried @ 200 °C, (B1-B3) α-Fe_2O_3 and (C1-C5) K/Cu/Fe iron catalysts

4.1.5 Attrition resistance measurements

The attrition resistance measurement of the iron catalysts was performed using the ASTM method. Table 4.4 shows the mass of the catalysts loaded into the attrition tube for measurements. The catalysts were then subjected to a pressure of 6 bars, and after 1 hour, the mass of the fines was collected, and the iron catalysts were recovered from the attrition tube. The attrition resistance of the catalysts was calculated based on the percentage of the fines lost after 1 hour using the formula below. The results obtained are shown in Table 4.5. Equation 4.2 was used to calculate the attrition loss of the iron catalysts.

$$Wt\% = m_1\text{-}m_0/ms \times 100 \qquad \text{Equation 4.2}$$

Where ms is the mass of the catalyst added to the attrition tube and m_0 is the mass of the empty fines collection assembly and m_1 is the mass of the fine particles collected per hour.

A higher rate of attrition indicates that the catalyst has less attrition resistance, while a smaller rate indicates that the catalysts have more attrition resistance. The catalysts can either undergo physical or chemical attrition. The α-Fe_2O_3 catalyst was found to be both physically and chemically attrition resistant as compared to 0.367 M K/Cu/Fe spray-dried at 200 °C catalyst. The results of the spent catalysts (recovered catalysts) from the XRD showed that the α-Fe_2O_3 recovered catalyst is more chemically attrition resistant since there was less phase change occurred, while the 0.367 M K/Cu/Fe spray-dried at 200 °C catalyst was found to be less chemically attrition resistant because more phase change was observed. The phase change causes internal stress within the catalyst particles, weakening them and leading to spalling or cracking and this causes a decrease of catalytic activity as a results of chemical attrition (Adeyiga, 2003). The results from Table 4.5 were obtained from physical attrition tests.

The order for the increase in attrition resistance according to the results in Table 4.5 is as follows; α-Fe_2O_3 >K/Cu/Fe>0.367 M K/Cu/Fe spray-dried at 200 °C. The attrition resistance of 0.367 M K/Cu/Fe spray-dried at 200 °C catalyst is 15 times worse than that of α-Fe_2O_3 catalyst. This could be attributed to the low mechanical strength and small particle size of 0.367 M K/Cu/Fe spray-dried at 200 °C. The catalyst particles fragmented easily during the physical attrition test and produces more fines, as shown in Table 4.4. Zhao et al. (2015) also obtained similar results in the unsupported iron catalyst. The authors reported that the large surface area of the unsupported iron

catalyst easily collapsed. Silicon dioxide (SiO_2) support was added to improve the structural strength of iron catalyst and prevent it from collapsing, which then improved the attrition resistance of iron catalyst (Zhao et al., 2015). The spray-drying technique is known to produce particles with excellent hardness and attrition resistance (Lin et al., 2021). The use of a smaller spray dryer was not suitable for producing iron catalysts that are more attrition resistant. As a result, a large spray dryer with convenient conditions to produce more attrition resistance iron catalysts is recommended.

Table 4.4: Attrition resistance measurements

Catalysts	Mass of the catalyst loaded (g)	Pressure (bar)	Mass of the fines collected (g)	Mass of the catalyst recovered (g)
α-Fe_2O_3	5.0062	6	0.1097	4.8627
0.367 M K/Cu/Fe spray-dried @ 200 °C	5.0048	6	1.5159	3.4219
K/Cu/Fe	5.0087	6	0.3823	4.5924

Table 4.5: The calculated attrition resistance results obtained from the ASTM test method

Catalysts	Rate of attrition loss (wt%/h)
α-Fe_2O_3	2.2
0.367 M K/Cu/Fe spray-dried @ 200 °C	30.3
K/Cu/Fe	7.6

4.1.6 Thermogravimetric analysis

The mass loss of the catalysts as a function of temperature was measured using TGA, the analysis was done in an air (O_2) atmosphere, and results are shown in Figure 4.6. The α-Fe_2O_3 catalyst showed a single mass loss step, while the K/Cu/Fe and 0.367 M K/Cu/Fe spray-dried at 200 °C exhibited two steps for mass loss. The first weight loss step occurred at approximately 100 °C in all the catalysts. The mass loss was 0.98%, 1.5%, and 8% for α-Fe_2O_3, K/Cu/Fe, and 0.367 M K/Cu/Fe spray-dried iron catalysts, respectively. This loss of weight indicates the removal of water existing on the surface (or in the pores) of the catalysts. The 0.367 M K/Cu/Fe spray-dried catalyst

at 200 °C showed high weight loss, meaning it had high moisture or humidity as compared to other catalysts. This could be ascribed to calcination temperature of 500 °C for 6 hours not being sufficient to calcine the spray-dried catalyst properly.

The graph in Figure 4.6 shows that the weight (%) increases as the temperature increases until reaching 800 °C for the α-Fe_2O_3 catalyst. The weight gain after 200 °C could be attributed to a change in the oxidation state of Fe from +3 to +2 as α-Fe_2O_3 oxidized to Fe_3O_4 in the presence oxygen gas (O_2), during the analysis because the TGA analysis was conducted in an air (O_2) atmosphere (Guduru and Mohanty, 2012; Motchelaho, 2011). The second mass loss occurred at temperatures between 570 °C to 700 °C for the K/Cu/Fe and 0.367 M K/Cu/Fe spray-dried at 200 °C catalysts. This mass loss could be due to the formation CO_2 according to equation 4.3. The presence of both carbon and oxygen was detected on SEM-EDS in Figure 4.4 and elemental mapping in Figure 4.5 and this confirm that CO_2 was produced at 570 °C to 700 °C on the K/Cu/Fe and 0.367 M K/Cu/Fe spray-dried at 200 °C catalysts. The mass loss obtained from the second step was 0.5% for K/Cu/Fe and 1% for 0.367 M K/Cu/Fe spray-dried at 200 °C catalysts.

$2Fe_2O_3 + 3C \rightarrow 3CO_2 + 4Fe$ Equation 4.3

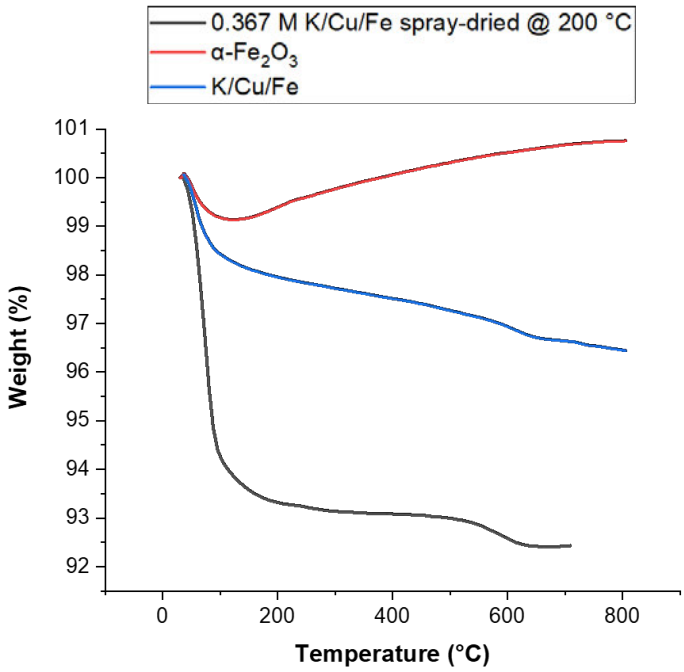

Figure 4.6: TGA of iron catalysts, α-Fe_2O_3, K/Cu/Fe, and 0.367 M K/Cu/Fe spray-dried @ 200 °C catalysts.

4.2 Effect of optimizing spray-drying parameters on the catalysts' physical and chemical properties

4.2.1 X-ray fluorescence

The elemental composition of the optimized spray-dried iron catalysts was determined using XRF assuming that the elements are in their oxide form. The results obtained are shown in Table 4.6. The composition of the catalysts observed from the XRF corresponds to the values in the synthesis solutions, with values slightly higher and lower in some cases. The results show that the co-precipitation and spray-drying techniques were efficient for the preparation of iron catalysts.

Table 4.6: Elemental composition of the optimized spray-dried catalysts

		Loading of metal oxides observed from the XRF (wt%)			
Catalysts	**Loading of metal oxides (wt%)**	**K_2O**	**CuO**	**Fe_2O_3**	**Na_2O**
0.367 M K/Cu/Fe spray-dried @ 140°C	5%K_2O/10%CuO/85%Fe_2O_3	4.7	8.5	86.5	-
0.734 M K/Cu/Fe spray-dried @ 140°C	5%K_2O/10%CuO/85%Fe_2O_3	4.5	8.7	86.9	-
1.101 M K/Cu/Fe spray-dried @ 140°C	5%K_2O/10%CuO/85%Fe_2O_3	4.8	8.9	87.9	-
1.101 M K/Cu/Fe spray-dried @ 155°C	5%K_2O/10%CuO/85%Fe_2O_3	4.5	8.9	85.5	-
0.367 M K/Cu/Fe spray-dried @ 200°C	5%K_2O/10%CuO/85%Fe_2O_3	4.4	8.5	84.9	-
0.734 M K/Cu/Fe spray-dried @ 200°C	5%K_2O/10%CuO/85%Fe_2O_3	4.9	8.4	83.4	4.7
1.101 M K/Cu/Fe spray-dried @ 200°C	5%K_2O/10%CuO/85%Fe_2O_3	4.8	8.9	87.1	2.6

4.2.2 X-ray Diffraction

Figure 4.7 exhibits XRD patterns of the optimized spray-dried catalysts that were prepared at different slurry concentrations of the precursors [Fe^{3+}] (0.367, 0.734, and 1.101 M) and temperatures of 140 °C, 155 °C, and 200 °C. The results show that all the optimized spray-dried iron catalysts exhibit a similar characteristic XRD pattern of the hematite (α-Fe_2O_3) phase composition. The hematite phase α-Fe_2O_3 appeared at the diffraction peaks of 2θ = 24.2°, 33.23°,

35.7°, 40.9°, 49.5°, 54.2°, 57.7°, 62.5°, and 64.0°. None of the catalysts showed diffraction patterns corresponding to CuO, suggesting that iron oxide (α-Fe_2O_3) makes up a large portion of the bulk phase and other metals are dispersed in the lattice (Wen et al., 2022). The average crystallite sizes of the catalysts were calculated by applying the Debye-Scherrer formula which was used in Figure 4.1. Furthermore, the optimized spray-dried catalysts prepared with a concentration of 0.734 M and temperatures of 140 °C and 200 °C showed a high degree of crystallinity of 58% as compared to all catalysts as shown in Table 4.8. This could be attributed to the high-surface-energy of the crystallite size shown by these catalysts. The surface atoms had an increased ability to arrange themselves in a more ordered, crystalline form as a result of the enhanced surface energy of the small crystallites (Nandiyanto et al., 2023).

As the temperature and concentration increased, the average crystallite size of the catalysts also increased, and this was due to the enhancement in the density of nucleation centers in the synthesized catalysts (Table 4.7) (Lassoued et al., 2017). These results are consistent with results reported by Lassoued et al. (2017), who observed an increase in crystallite size as precursor [Fe^{3+}] concentration increased. The authors optimized iron catalysts by increasing the range of these concentrations [Fe^{3+}] = 0.05, 0.1, 0.2 and 0.4 M and observed an increase in crystallite size from 21 to 82 nm (Lassoued et al., 2017).

Table 4.7: Effect of concentration and temperature on the crystallite size of iron catalysts

Catalysts reported by Lassoued et al., 2017	Average crystallite size (nm) reported by Lassoued et al., 2017	Catalysts from this study	Average crystallite size (nm) from this study
α-Fe_2O_3 with [Fe^{3+}] = 0.05 M	21	0.367 M K/Cu/Fe spray-dried @ 140 °C	3.75
α-Fe_2O_3 with [Fe^{3+}] = 0.1	39	0.367 M K/Cu/Fe spray-dried @ 200 °C	5.08
α-Fe_2O_3 with [Fe^{3+}] = 0.2	56	0.734 M K/Cu/Fe spray-dried @ 200 °C	6.69
α-Fe_2O_3 with [Fe^{3+}] =0.4	82	1.101 M K/Cu/Fe spray-dried @ 200 °C	10.33

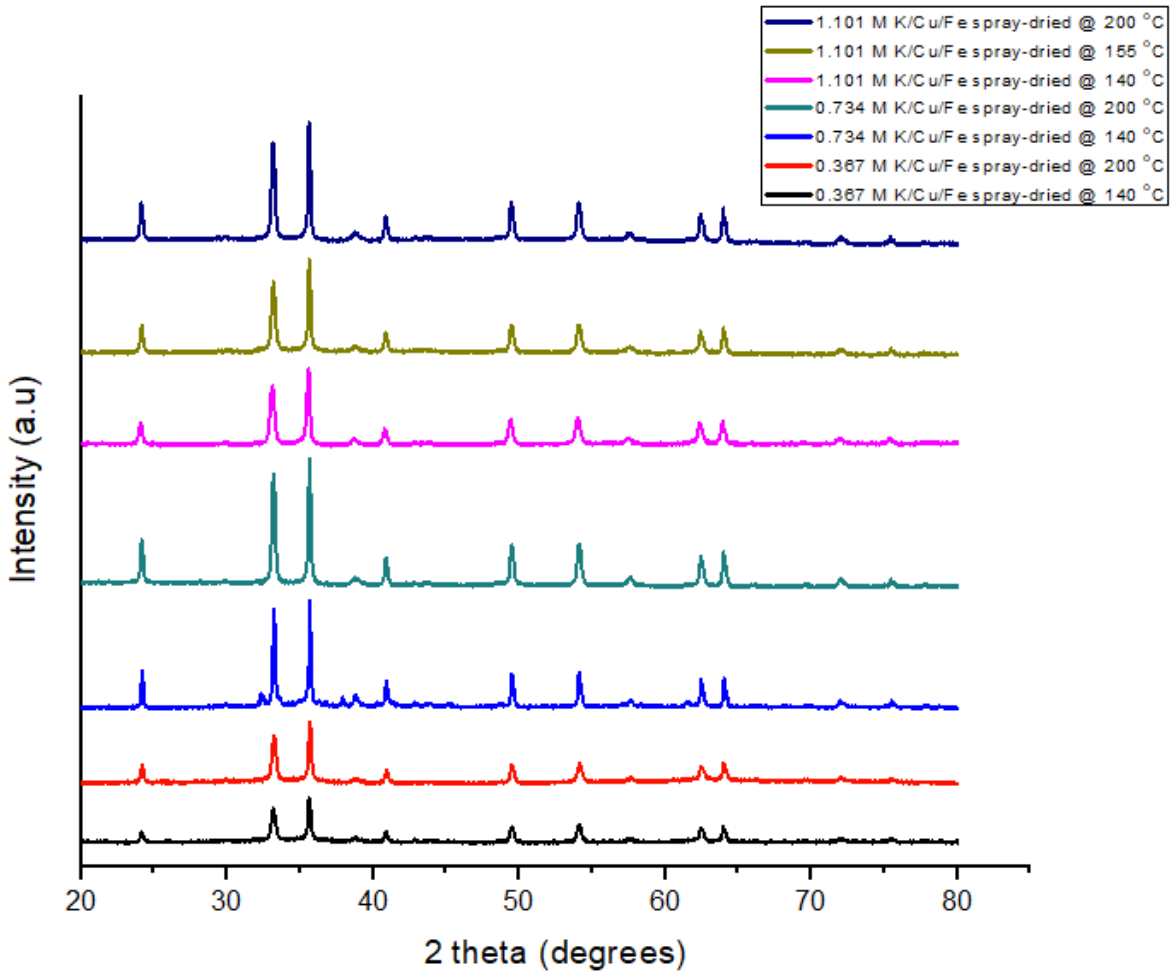

Figure 4.7: The XRD patterns of the optimized iron catalysts, 0.367 M K/Cu/Fe spray-dried @ 140 °C, 0.734 M K/Cu/Fe spray-dried @ 140 °C, 1.101 M K/Cu/Fe spray-dried @ 140 °C, 1.101 M K/Cu/Fe spray-dried @ 155 °C, 0.367 M K/Cu/Fe spray-dried @ 200 °C, 0.734 M K/Cu/Fe spray-dried @ 200 °C and 1.101 M K/Cu/Fe spray-dried @ 200 °C catalysts

4.2.3 Brunauer-Emmet-Teller analysis

The surface area, pore volume, and pore size of the catalysts were determined using BET. The spray-dried catalysts were optimized by varying parameters, including temperature and slurry concentration of the precursor [Fe^{3+}]. The results in Table 4.8 show that changing slurry concentration and temperature affects the physical properties of the catalysts. Increasing the slurry

concentration decreases the surface area and pore volume of the spray-dried iron catalysts. The catalysts prepared at a small concentration of 0.367 M show a high surface area as compared to the ones prepared at a high concentration, which showed a low surface area and pore volume. The results show that increasing temperature affects the pore size of the spray-dried catalysts. The catalysts prepared at 140 °C showed a large pore size as compared to the catalysts prepared at 155 °C and 200 °C. This could be attributed to the formation of larger, dense structures and agglomeration of particles in spray-dried catalysts prepared at a high temperature, and this led to a decrease in their pore size. The results obtained from SEM in Figure 4.9 showed that the catalysts prepared at a high temperature formed a cluster of particles, which decreased the defined spherical shape.

Table 4.8: The physical properties of optimized spray-dried catalysts

Catalysts	Surface Area (m^2/g)	Pore Volume (cm^3/g)	Pore size (nm)	Average Crystallite size (nm)	Degree of Crystallinity (%)
0.367 M K/Cu/Fe spray-dried @ 140 °C	33	0.20	20.9	3.75	30
0.734 M K/Cu/Fe spray-dried @ 140 °C	24	0.15	20.7	6.32	58
1.101 M K/Cu/Fe spray-dried @ 140 °C	20	0.14	23.4	6.36	56
1.101 M K/Cu/Fe spray-dried @ 155 °C	27	0.16	19.4	14.12	49
0.367 M K/Cu/Fe spray-dried @ 200 °C	39	0.16	13.2	5.08	55
0.734 M K/Cu/Fe spray-dried @ 200 °C	25	0.14	15.3	6.69	58
1.101 M K/Cu/Fe spray-dried @ 200 °C	23	0.13	19.4	10.33	40

Figure 4.8 displays the catalysts' N_2 adsorption-desorption isotherms. Following nitrogen uptake, no noticeable increase in any of the catalysts was observed, only at a relative pressure, P/Po= 0-0.82. An increase was observed when the relative pressure (P/Po) was beyond 0.82 according to the results (Han et al., 2019).

The findings in Figure 4.8 demonstrate that all the iron catalysts, including 0.367 M K/Cu/Fe spray-dried at 140 °C, 0.734 M K/Cu/Fe spray-dried at 140 °C, 1.101 M K/Cu/Fe spray-dried at 140 °C, 0.367 M K/Cu/Fe spray-dried at 200 °C ,0.734 M K/Cu/Fe spray-dried at 200 °C, and 1.101 M K/Cu/Fe spray-dried at 155 °C, exhibit type IV of Brunauer's classification isotherms

with H_1- type hysteresis loop at a relative pressure (P/Po = 0.65-0.95), which is typical of hexagonal mesoporous materials with cylindrical channels (Housaindokht and Pour, 2012; Han et al., 2019).

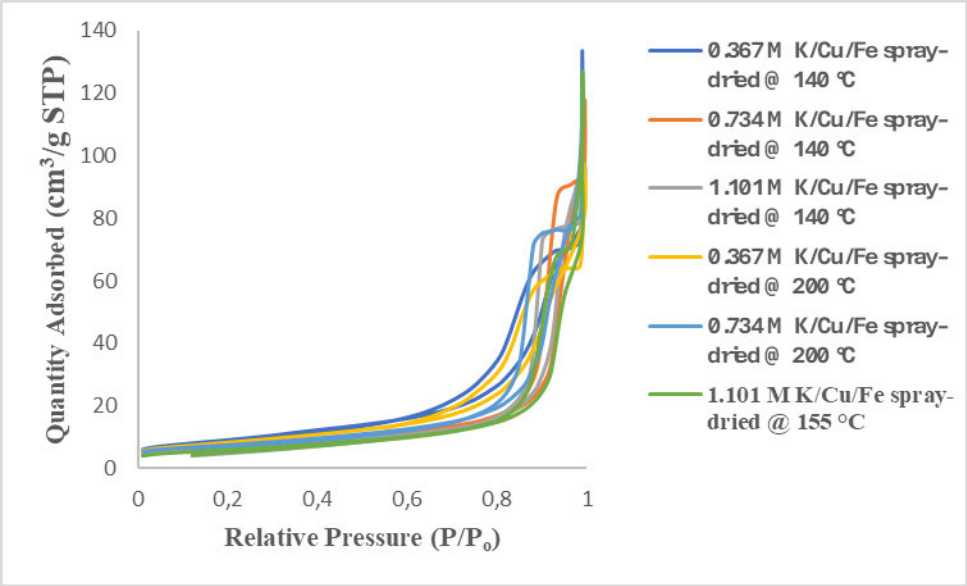

Figure 4.8: N_2 Adsorption-desorption isotherms for 0.367 M K/Cu/Fe spray-dried @ 140 °C, 0.734 M K/Cu/Fe spray-dried @ 140 °C, 1.101 M K/Cu/Fe spray-dried @ 140 °C, 0.367 M K/Cu/Fe spray-dried @ 200 °C, 0.734 M K/Cu/Fe spray-dried @ 200 °C and 1.101 M K/Cu/Fe spray-dried @ 155 °C catalysts.

4.2.4 Scanning Electron Microscopy

Figure 4.9 shows that all the optimized spray-dried catalysts consist of particles that are spherical in shape. The image J software was used to calculate the particle size from the SEM images. In comparison to Figure 4.9 (A) to (B), where the temperature was 140 °C and the concentration was increased from 0.367 M to 0.734 M, the size of the catalyst particles increased from approximately 1–2 µm to 1–10 µm. Increasing the concentration further, the size did not increase significantly, however, the particles appeared to clump together into a cluster, and the spherical shape was less defined. In comparison to Figure 4.9 (A) to (D), where the temperature of the slurry was increased from 140 °C to 200 °C at a concentration of 0.367 M, there is also an increase in the size of the particles, approximately from 1–2 µm to 1–5 µm. Increasing the slurry concentration to 0.734 M, as shown in Figure 4.9 (E), the size of the particles increases even further to 10 µm. Increasing the slurry concentration to 1.101 M resulted in the size of 10 µm, however, an evident clustering of

particles, which decreased the defined spherical shape. The decrease of the defined spherical shape reduced the pore size of the catalysts as observed from the BET results in Table 4.6.

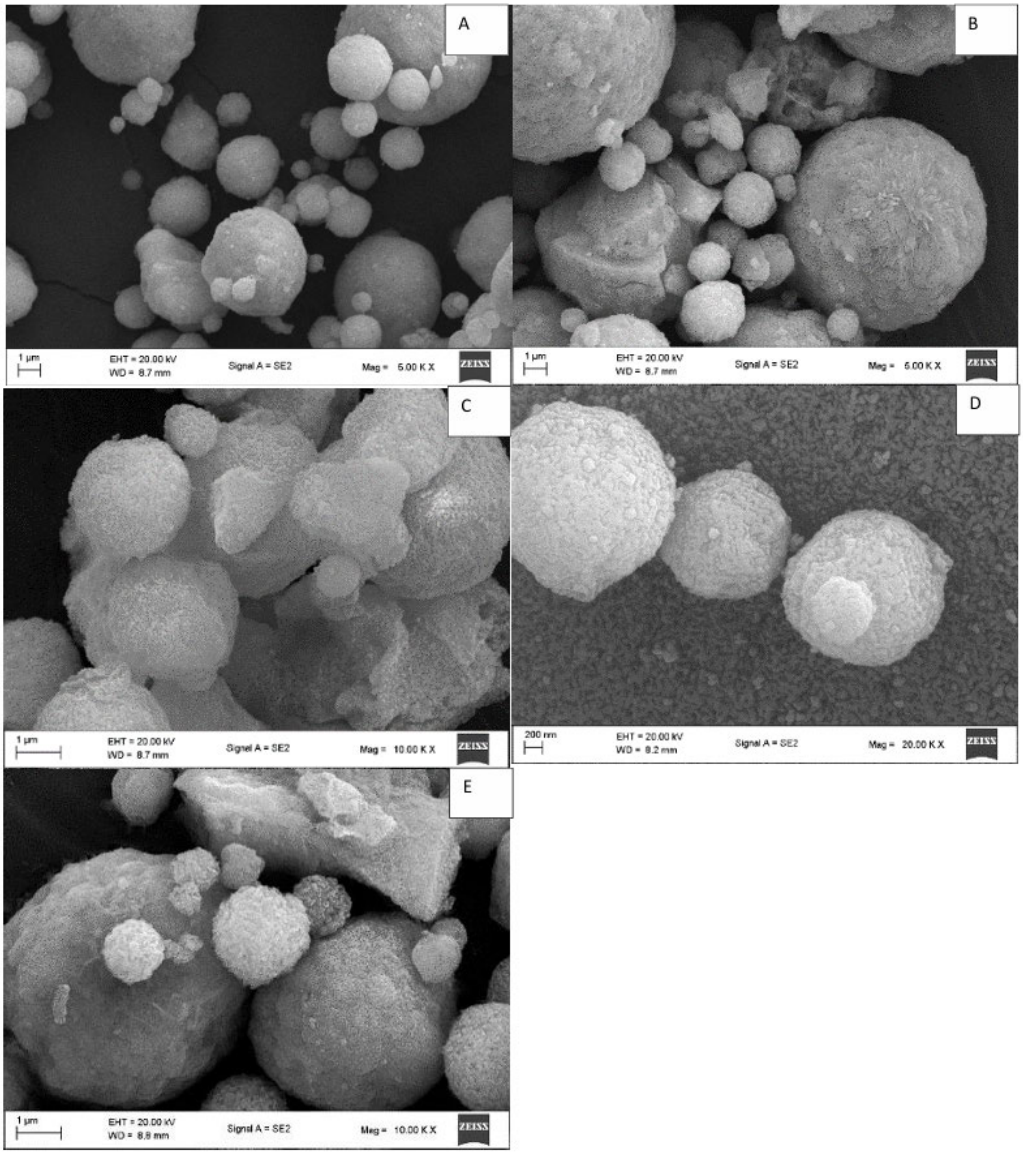

Figure 4.9: SEM images of (A) 0.367 M K/Cu/Fe spray-dried @ 140 °C, (B) 0.734 M K/Cu/Fe spray-dried @ 140 °C, (C) 1.101 M K/Cu/Fe spray-dried @ 140 °C, (D) 0.367 M K/Cu/Fe spray-dried @ 200 °C and (E) 0.734 M K/Cu/Fe spray-dried @ 200 °C catalysts.

SEM-EDS analysis showed that the 0.367 M K/Cu/Fe spray-dried @ 140 °C and the 0.734 M K/Cu/Fe spray-dried @ 200 °C catalysts are composed of Fe, Cu, K, O, and C elements, as shown in Figure 4.10. All the other optimized spray-dried catalysts showed similar elements as compared to the catalysts shown in Figure 4.10. However, 0.734 M K/Cu/Fe spray-dried @ 200 °C and 1.101

M K/Cu/Fe spray-dried @ 155 °C catalysts showed the presence of the sodium (Na) element in addition to the Fe, Cu, K, O, and C elements. Sodium detected by SEM-EDS was also observed from the XRF results in Table 4.6 for both 0.734 M K/Cu/Fe spray-dried @ 200 °C and 1.101 M K/Cu/Fe spray-dried @ 155 °C catalysts. The results of elemental mapping in Figure 4.11 further confirm similar results obtained from the SEM-EDS in Figure 4.10. All the elements, including Fe, Cu, K, O, Na, and C, were found to be uniformly distributed throughout the optimized spray-dried catalyst particles, indicating that a homogeneous composition was achieved from the catalysts, as shown in Figure 4.11. All the other optimized spray-dried catalysts also showed the same results.

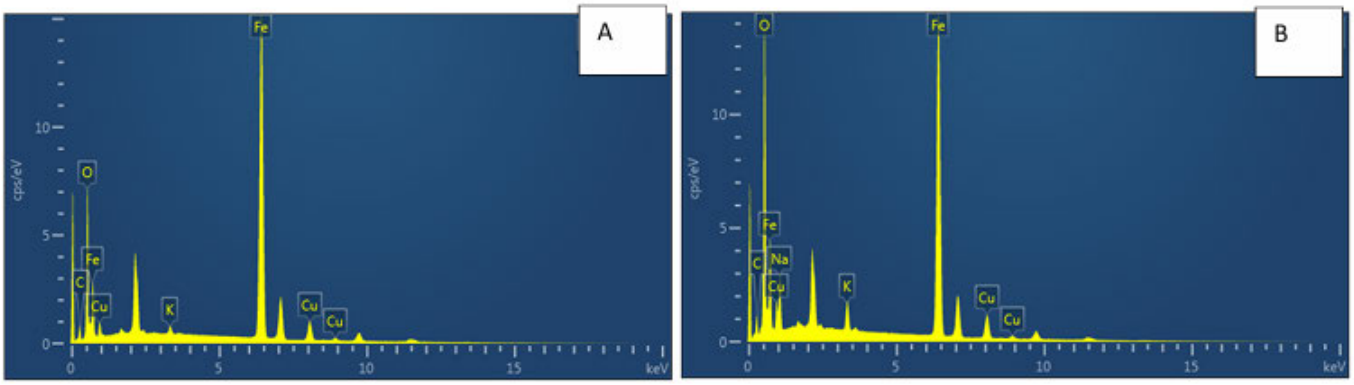

Figure 4.10: SEM-EDS analysis of (A) 0.367 M K/Cu/Fe spray-dried @ 140 °C, (B) 0.734 M K/Cu/Fe spray-dried @ 200 °C catalysts

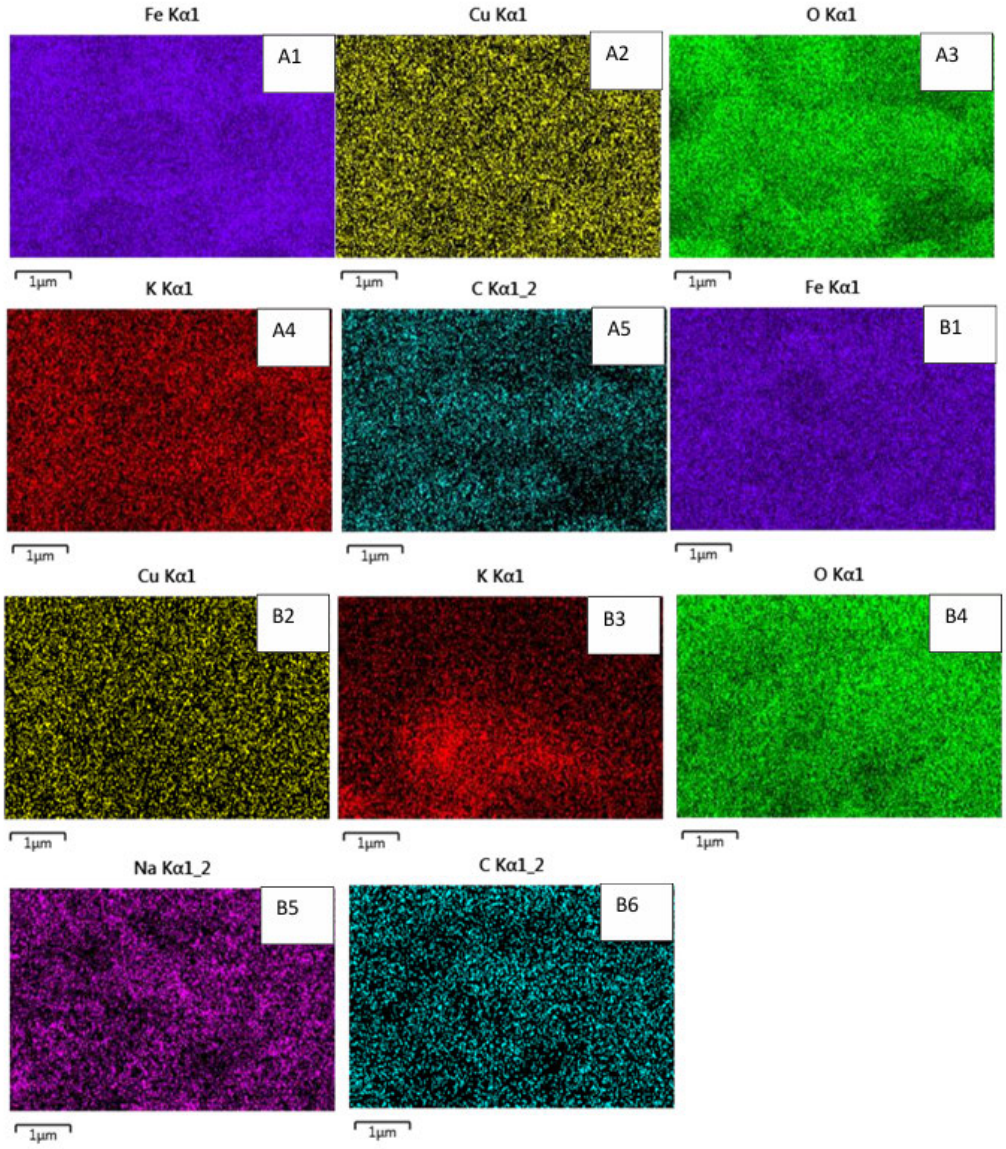

Figure 4.11: Elemental mapping analysis of (A1-A5) 0.367 M K/Cu/Fe spray-dried @ 140 °C, (B1-B6) 0.734 M K/Cu/Fe spray-dried @ 200 °C catalysts

4.2.5 Thermogravimetric analysis

TGA results of the optimized spray-dried iron catalysts are displayed in Figure 4.12. The TGA was conducted in an air (O_2) atmosphere. According to the results, the optimized spray-dried iron catalysts exhibited two steps for mass loss. The first weight-loss step occurred at 100 °C in the

catalysts. The mass loss was 6.3%, 3.5%, 3,5%, 6,5%, 6.5%, and 5.5% for 0.367 M K/Cu/Fe spray-dried at 140 °C, 0.734 M K/Cu/Fe spray-dried at 140 °C, 1.101 M K/Cu/Fe spray-dried at 140 °C, 0.367 M K/Cu/Fe spray-dried at 200 °C, 0.73 M K/Cu/Fe spray-dried at 200 °C, and 1.101 M K/Cu/Fe spray-dried at 155 °C iron catalysts respectively. This loss of weight indicated the removal of water existing on the surface (and in the pores) of the catalysts. The second mass loss occurred at temperatures between 570 °C and 700°C. This mass loss could be due to the formation CO_2 according to equation 4.3. The presence of both carbon and oxygen was detected on SEM-EDS results in Figure 4.10, and this confirms that CO_2 was formed at 570 °C to 700 °C on the spray-dried catalysts.

The second mass loss could also be due to the decomposition of leftover precursor sodium carbonate (Na_2CO_3) to produce sodium oxide and carbon dioxide gas. The Na_2O was observed from the XRF results in Table 4.6. The presence of sodium (Na) was also detected on the SEM-EDS of 0.734 M K/Cu/Fe spray-dried @ 200 °C and 1.101 M K/Cu/Fe spray-dried @ 155 °C catalysts, and this confirms that there was leftover Na_2CO_3 that decomposed. This meant that Na_2CO_3 was not completely removed from these catalysts in the washing step during the preparation and it decomposed at the temperature above 500 °C to produce sodium oxide and carbon dioxide gas. A mass loss of 1%, 1%, 2.75%, 1%, and 2.5% for 0.367 M K/Cu/Fe spray-dried at 140 °C, 0.734 M K/Cu/Fe spray-dried at 140 °C, 1.101 M K/Cu/Fe spray-dried at 140 °C, 0.367 M K/Cu/Fe spray-dried at 200 °C, and 1.101 M K/Cu/Fe spray-dried at 155 °C catalysts, respectively, was observed. The 0.734 M K/Cu/Fe spray-dried at 200 °C showed a high mass loss of 9% in the second step, meaning there was more Na_2CO_3 left-over or CO_2, and it decomposed at the temperature above 500 °C.

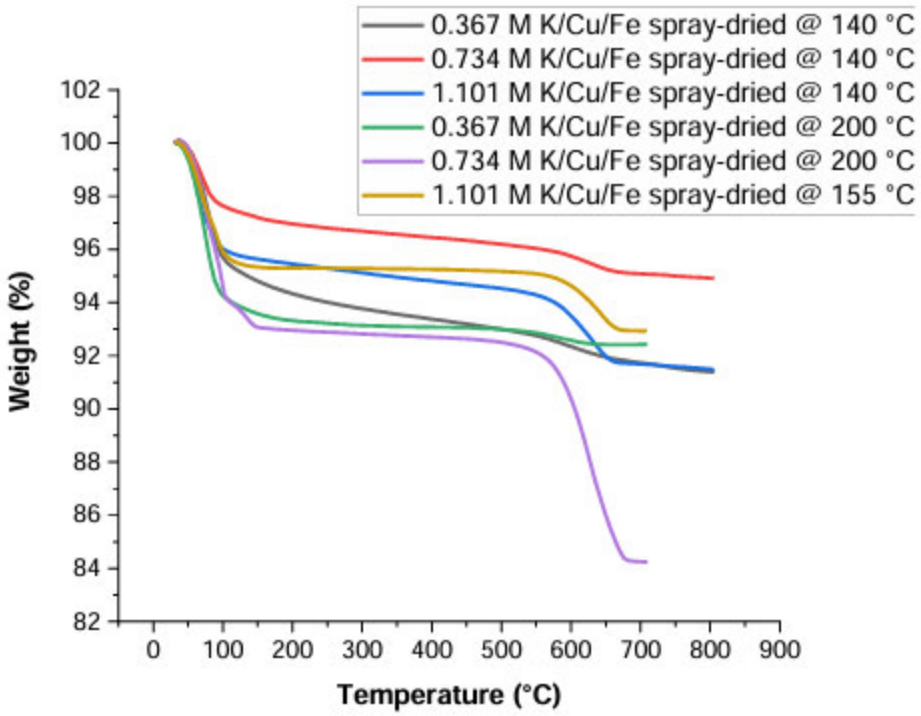

Figure 4.12: TGA of the optimized spray-dried iron catalysts, 0.367 M K/Cu/Fe spray-dried @ 140 °C, 0.734 M K/Cu/Fe spray-dried @ 140 °C, 1.101 M K/Cu/Fe spray-dried @ 140°C, 0.367 M K/Cu/Fe spray-dried @ 200 °C, 0.734 M K/Cu/Fe spray-dried @ 200 °C, and 1.101 M K/Cu/Fe spray-dried @155 °C catalysts

4.3 Catalytic Testing

4.3.1 F-TS product selectivity

The product selectivity results exhibited in Table 4.9 were obtained from the gas chromatography using a flame ionization detector (GC-FID) and thermal conductivity detector (GC-TCD). The results showed that the selectivity for C_1 to C_4 hydrocarbons was suppressed, whereas CO conversions and selectivity of (C_{5+}) hydrocarbons were enhanced in the K/Cu/Fe and 0.367 M K/Cu/Fe spray-dried at 200 °C catalysts. It was expected that the presence of copper and potassium from K/Cu/Fe and 0.367 M K/Cu/Fe spray-dried at 200 °C would favour a high selectivity of C_{5+} hydrocarbons, however, instead, the α-Fe_2O_3 catalyst was the one that showed a high C_{5+} selectivity of 60.9%. Literature has reported that the potassium promoter increases the CO conversions, C_{5+} selectivity, and decreases the C_1 selectivity (Zhang et al., 2018; Todic et al.,

2016). The potassium promoter gives electrons to the metal to increase the CO adsorption while decreasing that of H_2, which raises the selectivity of C_{5+} hydrocarbons, CO conversion and lowers methane (C_1) selectivity (Todic et al., 2016). However, copper is more effective at increasing the C_{5+} selectivity and improves the reduction of iron with CO to create the iron carbide (Fe/C) active phase for F-TS (Barrios et al., 2020). The increased CO conversion in Figure 4.13 illustrates this. For the K/Cu/Fe and 0.367 M K/Cu/Fe spray-dried at 200 °C catalysts, C_{5+} hydrocarbon selectivity decreased because the results were calculated with CO_2 included due to the carbon balance. When CO_2 was excluded in the calculation of C_{5+} selectivity, the carbon balance added up to above 100% and the promoted catalysts showed high C_{5+} selectivity of 94% while the α-Fe_2O_3 catalyst showed selectivity of 80%. The catalysts K/Cu/Fe and 0.367 M K/Cu/Fe spray-dried at 200 °C demonstrated high CO_2 selectivity of 43.3% and 42.2% respectively, which led to the production of C_{5+} hydrocarbons at 51.3% and 51.5% as shown in Table 4.9.

According to the results in Table 4.9, the K/Cu/Fe and 0.367 M K/Cu/Fe spray-dried at 200 °C catalysts showed poor performance with regards to the selectivity of C_2-C_4 hydrocarbons as compared to the K/Cu/Fe catalyst reported by Guo et al. (2016). The reported catalyst was prepared using a similar procedure of co-precipitation and spray-drying methods. The catalyst was evaluated at 235 °C, 2.3 MPa, GHSV= 3000 h^{-1}, H_2/CO=1.5 and 12.6% C_2-C_4 selectivity and 60.5% CO conversion was obtained. On the other hand, the catalysts used in this study showed low C_2-C_4 selectivity of 3.9% and 5.2% for the K/Cu/Fe and 0.367 M K/Cu/Fe spray-dried @ 200 °C catalysts, respectively. However, the α-Fe_2O_3 catalyst showed better C_2-C_4 selectivity of 13.5%, which is higher than the reported K/Cu/Fe catalyst in the literature. Furthermore, the α-Fe_2O_3 catalyst showed a slightly high olefin to paraffin ratio of 4.9 as compared to the K/Cu/Fe and 0.367 M K/Cu/Fe spray-dried at 200 °C catalysts, which produced 4.3 and 4.7 as shown in Table 4.9. This ratio meant that there was high hydrogenation activity on the surface of the α-Fe_2O_3. The trend for an increase in the olefin/paraffin ratio was as follows; K/Cu/Fe<0.367 M K/Cu/Fe spray-dried at 200 °C< α-Fe_2O_3 catalysts.

The catalysts were not selective enough to produce high C_2, C_3, and C_4 hydrocarbons, however, these were more selective to the higher molecular weight hydrocarbons (C_{5+}). The chromatograms from which the data was obtained show high peaks for the high molecular weight hydrocarbons for all the iron catalysts and low peaks towards C_2, C_3, and C_4 hydrocarbons. Another possibility

is that the catalysts were more selective to the secondary products, such as alcohols and other products produced by the side reactions (equation 2.4) from F-TS, instead of the (C_2, C_3, and C_4 hydrocarbons) products. The surface properties of the catalysts, such as basic or acidic sites, need to be studied and improved in order to modify the catalysts properties, to achieve selectivity to C_2, C_3, C_4 hydrocarbons, and C_4 olefins rather than the products produced by side reactions (equation 2.4). The C_2-C_4 hydrocarbons are needed in industry to produce polymers. Although the catalysts did not show good performance, the α-Fe_2O_3 catalyst showed better selectivity to CO_2, C_2, C_3, and C_4 (olefin/paraffin ratio) compared to all catalysts, as shown in Table 4.9. The good performance of the α-Fe_2O_3 catalyst could be attributed to it having more attrition resistance than all other catalysts, according to the attrition resistance results in Table 4.5. All the catalysts (α-Fe_2O_3, K/Cu/Fe, and 0.367 M K/Cu/Fe spray-dried at 200 °C) showed good selectivity characteristics (low methane and high selectivity C_{5+}) hydrocarbons as shown in Table 4.7. This could be attributed to the iron carbide (χ-Fe_5C_2) active phase or site which increased the chain growth and favored the production of C_{5+}) hydrocarbons while decreasing methane selectivity.

Table 4.9: F-TS performance results of the iron catalysts calculated including CO_2

Catalysts	CO conversion (%)	Selectivity (C-%)							C_4 (Olefin/Paraffin ratio)
		CO_2	C_1	C_2	C_3	C_4 Olefin	C_4 Paraffin	C_{5+}	
α-Fe_2O_3	60.4	23.0	2.6	4.2	5.4	3.3	0.7	60.9	4.9
K/Cu/Fe	74.4	43.3	1.6	1.5	1.5	0.8	0.2	51.3	4.3
0.367 M K/Cu/Fe spray-dried @ 200 °C	72.2	42.2	1.1	1.5	2.1	1.3	0.3	51.5	4.7

Reaction conditions: 260°C, 20 bar, H_2/CO= 2, GHSV= 5000h^{-1}, reaction period= 62 hours

4.3.2 Activity and reaction stability

The catalysts K/Cu/Fe and 0.367M K/Cu/Fe spray-dried at 200 °C catalysts show a high CO conversion as compared to the α-Fe_2O_3 catalyst. The addition of promoters has likely increased the CO conversion of the catalysts (Barrios et al., 2020). The catalytic conversion initially dropped from 100% conversion to between 60-80% in the first 28 h as shown in Figure 4.13. In this period, the catalysts may be restructuring, sintering, or undergoing attrition, which decreases the CO

conversion. After that, the catalysts were stable as they did not show long-term deactivation as the reaction progressed until they reached 72 h. For the K/Cu/Fe catalyst, the CO conversion decreased to from 100%-69% at 28 h as shown in Figure 4.13. The catalyst was highly active at the beginning of a reaction and loss its activity as the reaction proceeded (downward trend). After 28 hours, the conversion increased slightly (upward trend) to 72% and there the catalyst regained its activity and remained stable until reaching 72 hours. For the 0.367 M K/Cu/Fe spray-dried at 200 °C catalyst, the conversion decreased to 67% at 28 h, and after that, it increased to 72% and remained stable until reaching 72 h. These two catalysts showed similar activity in the CO conversion. The α-Fe_2O_3 catalyst gradually decreased to 51% at 16 h, increased slightly to 57% at 28 h, and after that, the catalyst remained stable until reaching 72 h as shown in Figure 4.13.

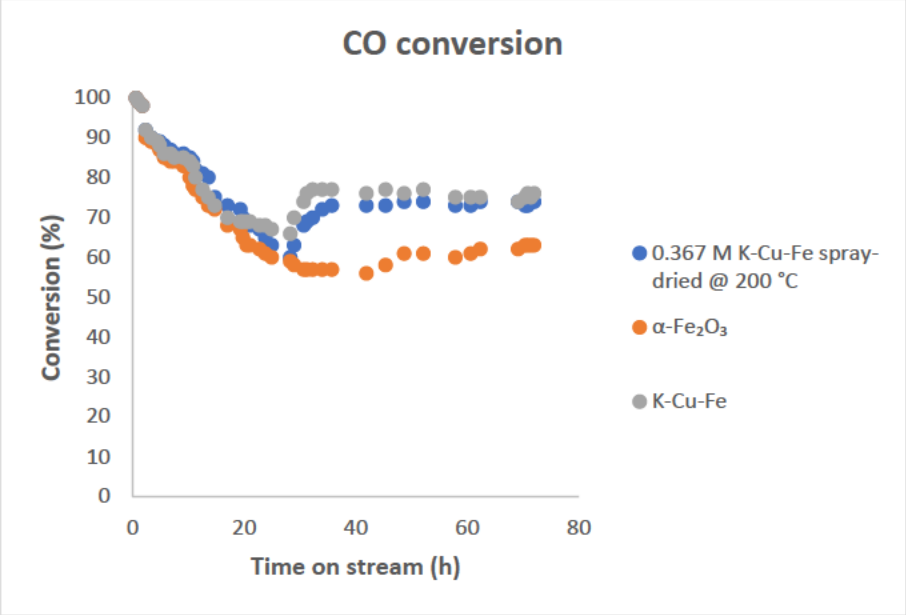

Figure 4.13: CO conversion for the α-Fe_2O_3, K/Cu/Fe and 0.367 M spray-dried at 200 °C catalysts with time on stream.

Figure 4.14 shows that the CO_2 selectivity was increasing during the reduction of iron catalysts with CO because the active phase (Fe_3O_4) responsible for CO_2 production via wager-gas shift reaction was still being formed in the first 20 h. As illustrated in Figure 4.14, the K/Cu/Fe and 0.367 M K/Cu/Fe spray-dried at 200 °C catalysts did not perform well since they produce more

CO_2 which is undesirable product in contrast to α-Fe_2O_3 catalyst. The water-gas shift reaction (WGS) is responsible for the high CO_2 selectivity. The presence of potassium is known to promote the water gas shift activity, which could be the reason for these two catalysts to produce high CO_2 selectivity (Wang, 2023). As the reaction progressed, the CO_2 selectivity decreased slightly and remained constant for the spray-dried catalyst until both catalysts reached 42% at 72 h. The α-Fe_2O_3 catalyst performed better by demonstrating low CO_2 selectivity, which is almost half the percentage obtained from the other two catalysts. This indicates that a mild or low water gas shift reaction occurred on this catalyst. The α-Fe_2O_3 catalyst started showing CO_2 selectivity of 20% at 20 h and increased slightly as the reaction proceeded, eventually reaching 23% at 72 h of the reaction.

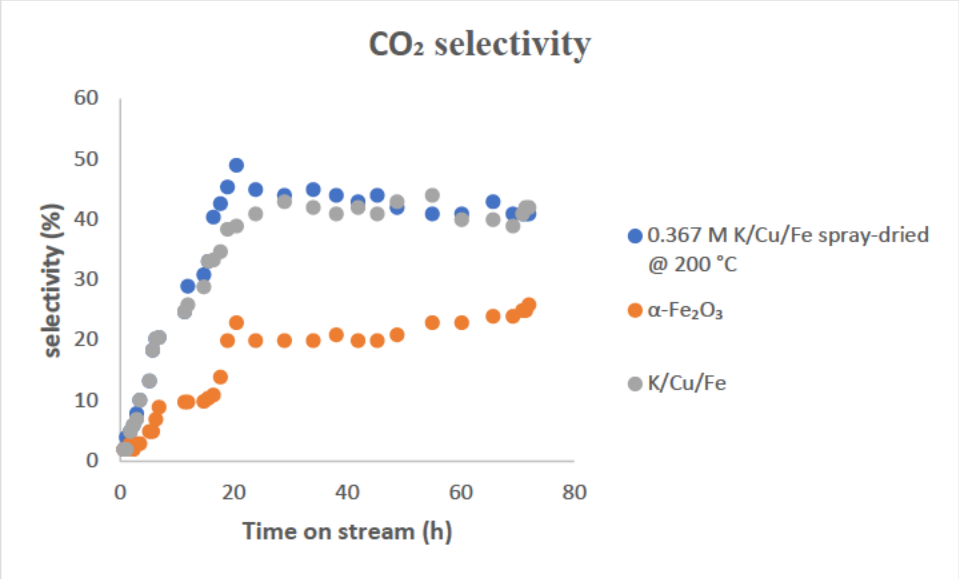

Figure 4.14: CO_2 selectivity profiles of the α-Fe_2O_3, K/Cu/Fe and 0.367 M spray-dried at 200 °C catalysts with time on stream.

The results in Figure 4.15 showed that there were no C_1 products formed during the reduction of the catalysts with CO from 0–20 h. This may be due to the catalysts still in an oxide form, which is not active to produce hydrocarbons in F-TS. After 20 h, the C_1 hydrocarbons were produced because the reduction period of the catalysts was completed and the active phase (χ-Fe_5C_2) was

formed, which is responsible for producing the hydrocarbons. Another reason could be that the H_2 flow was started or introduced to the reactor after 20 h, when the reduction of the catalysts or CO activation was completed. All the catalysts initially showed high selectivity for C_1 product at 21–28.3 h, and after that, the activity decreased as the reaction progressed due to catalytic deactivation and the catalysts remained stable until reaching 72 h.

Furthermore, the α-Fe_2O_3 catalyst started with 3% selectivity of C_1 at 21 h, and the selectivity decreased as the reaction proceeded, until reaching selectivity of 2.6% at 38 h as shown in Figure 4.15. After 38 h, the catalyst remained stable until reaching 72 h. The catalysts K/Cu/Fe and 0.367 M K/Cu/Fe spray-dried at 200 °C showed low selectivity of C_1 (methane) as expected. This meant that the addition of promoters, potassium and copper to the unsupported iron catalyst decreased methane selectivity (Tavares et al., 2022). The K/Cu/Fe catalyst started with a selectivity of 2% at 28.3 h, and the selectivity decreased slightly as the reaction progressed until reaching a selectivity of 1.3% at 39.7 h. After 39.7 h, the catalysts regained the activity and remained stable with a selectivity of 1.45% until reaching 72 h. Furthermore, 0.367 M K/Cu/Fe spray-dried at 200 °C catalyst started with a selectivity of 2% at 21 h and then decreased to a selectivity of 0.10% at 34 h. After 34 h, the catalyst regained the activity and remained stable until reaching a selectivity of 1.1% at 72 h.

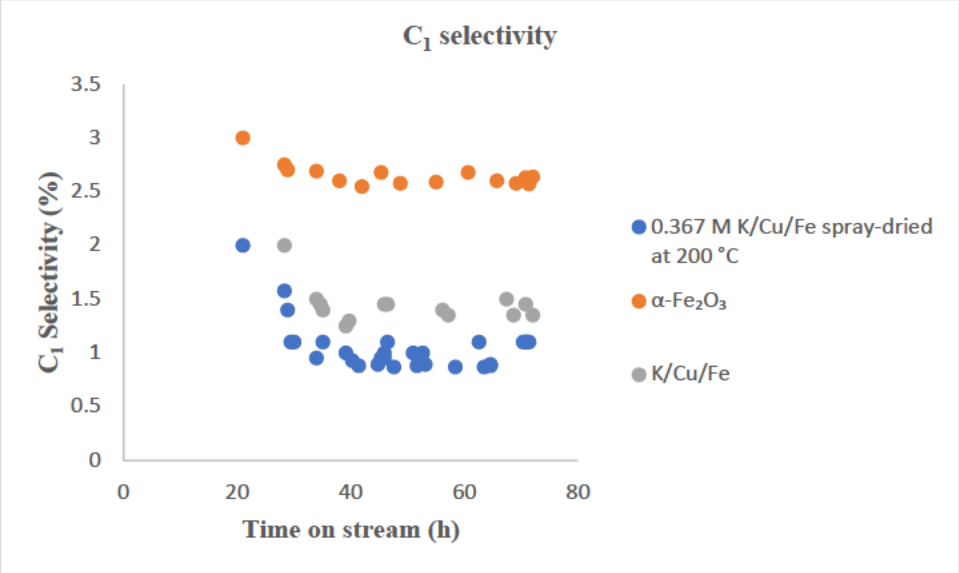

Figure 4.15: C_1 selectivity profiles of the α-Fe_2O_3, K/Cu/Fe and 0.367 M spray-dried at 200 °C catalysts with time on stream.

The results in Figure 4.16 showed that C_2 products were not formed during the reduction of the catalysts in the presence of CO from 0–20 h, which was also observed from Figure 4.15. The catalysts K/Cu/Fe and 0.367 M K/Cu/Fe spray-dried at 200 °C both showed high C_2 carbon selectivity as shown in Figure 4.16. The presence of the promoters' increases C_2 carbon selectivity (Todic et al., 2016). The catalysts initially showed high selectivity of 8.5% at 39 h and 7.6% at 28 h for K/Cu/Fe and 0.367 M K/Cu/Fe spray-dried at 200 °C catalysts, respectively. As the reaction proceeded, the selectivity decreased slightly due to catalytic deactivation, and the catalysts were stable after 45 h and maintained the stability until 72 h. The α-Fe_2O_3 catalyst showed low C_2 selectivity compared to the other two catalysts. The catalysts started with a selectivity of 4.1% at 16 h and slightly decreased as the reaction progressed due to loss of catalytic activity and remained stable after 20 h, reaching a selectivity of 3.5% at 72 h of the reaction.

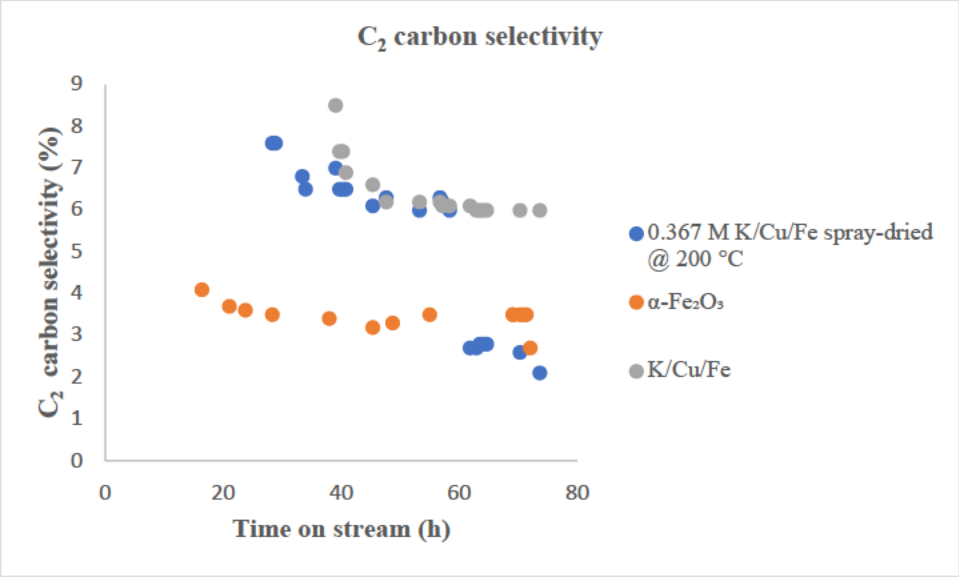

Figure 4.16: C_2 selectivity profiles of the α-Fe_2O_3, K/Cu/Fe and 0.367 M spray-dried at 200 °C catalysts with time on stream.

The selectivity profiles in Figure 4.17 shows that C_3 hydrocarbons were formed after 20 h where the active phase (χ-Fe_5C_2) was formed, and F-TS was occurring as observed from Figure 4.15 and

Figure 4.16. The α-Fe_2O_3 and K/Cu/Fe catalysts showed high selectivity for C_3 hydrocarbons. This can be attributed to a high activity of the active phase (χ-Fe_5C_2) in the catalysts, and this favoured the production of more C_3 hydrocarbons. The α-Fe_2O_3 catalyst started with 4.7% selectivity at 16 h and increased as the reaction proceeded, maintaining good stability and eventually reaching a selectivity of 5.3% at 72 h. The K/Cu/Fe catalyst started with a high selectivity of 4.6% at 40 h. A slight decreased to a selectivity of 4% was observed and the catalyst remained stable after 35 h as the reaction proceeded until reaching the 72 h of reaction. The 0.367 M K/Cu/Fe spray-dried at 200 °C catalyst showed lower C_3 carbon selectivity compared to the other catalysts. This could be ascribed to the active phase (χ-Fe_5C_2) being easily oxidized by water, which reduced the activity of the catalyst (Claeys et al., 2021). Catalysts deactivate when there is water present in the product stream, which lowers the amount of CO converted and the selectivity of hydrocarbons (James et al., 2012). The catalyst started with a selectivity of 3.5% at 28 h and then decreased gradually due to a loss of activity as the reaction progressed, until reaching a selectivity of 2.5% at 72 h.

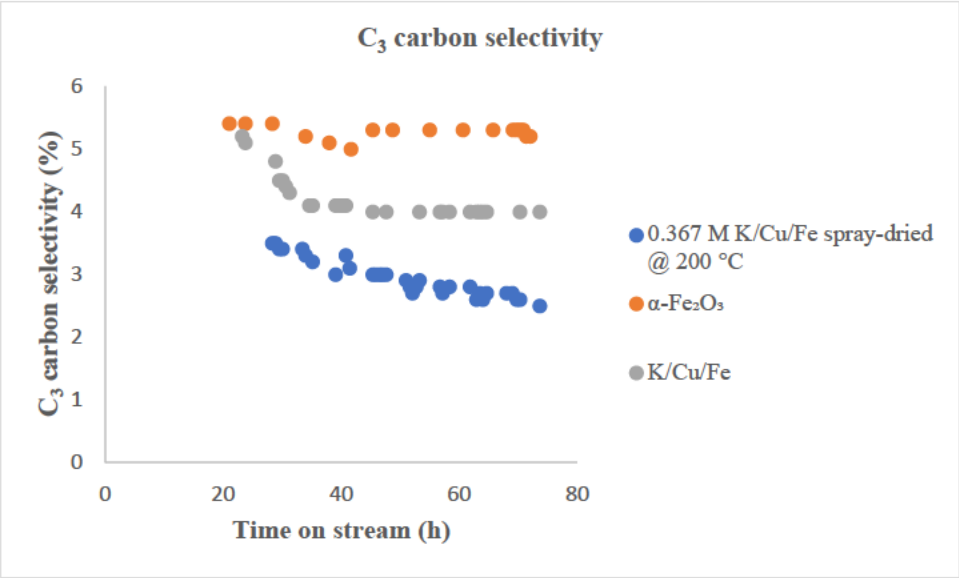

Figure 4.17: C_3 selectivity profile of the α-Fe_2O_3, K/Cu/Fe and 0.367 M spray-dried at 200 °C catalysts with time on stream.

CHAPTER 5: CONCLUSIONS AND RECOMMENDATIONS

Conclusions

This study aimed to develop high-surface-area and attrition-resistant iron catalysts for F-TS. The iron catalysts, α-Fe_2O_3, 0.367 M K/Cu/Fe spray-dried at 200 °C and K/Cu/Fe) were prepared using the co-precipitation, impregnation methods and spray-drying technology. The elemental composition of the catalysts corresponded to the target loading as observed from X-ray fluorescence results, signifying that the co-precipitation, impregnation and spray-dying methods were efficient for the preparation of iron catalysts. It was further revealed that iron catalysts, including the optimized spray-dried catalysts, exhibited similar XRD patterns of the hematite phase with the rhombohedral (hexagonal) structure of α-Fe_2O_3 and are crystalline in nature, as indicated by the sharp diffraction peaks from the X-ray diffraction. After testing, the catalysts showed other two phases of iron; Fe_3O_4, and χ-Fe_5C_2, as observed from the XRD.

The BET results showed that the 0.367 M K/Cu/Fe spray-dried at 200 °C catalyst has a high surface area of 39 m^2/g compared to 26 m^2/g and 25 m^2/g for α-Fe_2O_3 and K/Cu/Fe catalysts. The surface area, pore volume, and pore size of all the catalysts increased after the attrition resistance test. The BET results showed that the surface area of the of the optimized spray-dried catalysts decreases with increasing temperature and [Fe^{3+}] precursor slurry concentration. It was revealed that the α-Fe_2O_3 and K/Cu/Fe catalysts consisted of particles with a small and spherical shape that is approximately 0.2 μm. On the other hand, the 0.367 M K/Cu/Fe spray-dried catalyst at 200 °C consists of spherical-shaped particles with a size of approximately 1 to 2 μm, according to the results observed from the scanning electron microscopy. The optimized spray-dried catalysts SEM results showed that as the slurry concentration of [Fe^{3+}] precursor and temperature increased, the particle size increased. Increasing the concentration further did not result in an increase in the particle size, however, the particles appeared to clump together into a cluster, and the spherical shape was less defined.

The results from the physical attrition test obtained from the ASTM revealed the attrition resistance of 0.367 M K/Cu/Fe spray-dried at 200 °C catalyst is 15 times worse than that of α-Fe_2O_3 catalyst. The results from XRD also showed that α-Fe_2O_3 recovered catalyst is more chemically attrition

resistant as compared to the 0.367 M K/Cu/Fe spray-dried @ 200 °C recovered catalyst. The application of a small spray dryer forms catalysts with a high surface area and less attrition resistance. It is challenging to increase the particle size using a small spray dryer as it does not have convenient conditions to produce larger particles that are more attrition resistant.

In terms of the activity and selectivity of the catalysts on F-TS reaction, results from the F-TS reaction showed that the selectivity to C_1-C_4 hydrocarbons was suppressed, whereas CO conversions and selectivity to high hydrocarbons (C_{5+}) were enhanced using the K/Cu/Fe and 0.367 M K/Cu/Fe spray-dried at 200 °C catalysts. It was revealed that all the catalysts produced low selectivity of C_2-C_4 hydrocarbons. The catalysts are more selective to the C_{5+} hydrocarbons. All the catalysts including the α-Fe_2O_3, K/Cu/Fe and 0.367 M K/Cu/Fe spray-dried at 200 °C showed good selectivity characteristics (low methane (C_1) and high selectivity to C_{5+} hydrocarbons respectively). The reaction stability results in the conversion of CO, showed that the catalysts exhibited high activity initially, however, as the reaction proceeded, the conversion of CO decrease over time on stream due to loss of catalytic activity. The selectivity results showed that all catalysts initially showed high catalytic activity for the C_1, C_2, and C_3 products and their activity decreased over time as the reaction proceeded. The α-Fe_2O_3 catalyst showed high catalytic activity overall as compared to the other catalysts. The activity, selectivity of iron catalysts towards C_1-C_4 and C_{5+} hydrocarbons can be improved before the industrial application.

Recommendations and future work

Supports such as silica could be added to the spray-dried iron catalyst to improve attrition resistance. The iron catalyst with improved attrition resistance could be tested for F-TS using another type of reactor, such as a fixed-bed reactor, and the performance evaluated. The supports, such as carbon nanotubes and alumina, could be added to the iron catalysts to improve the activity and enhance catalyst stability and performance over long periods. The selectivity of iron catalysts could be improved by modifying the surface of the catalysts through hydrophobization and this will reduce CO_2 selectivity and improve hydrocarbon selectivity. The catalysts can be further characterized using in-situ XRD, TEM, TPR/TPO, Raman spectroscopy and Mössbauer spectroscopy. Several methods for measuring attrition resistance, including the Davison jet cup, hot attrition test, roller test, air jest test and ultrasonic test, can be used to further examine the

attrition resistance of the catalysts. A larger spray dryer will be used for future research to prepare iron catalysts that have large particle size of approximately 100 μm and are more attrition-resistant. The optimized spray-dried iron catalysts will be tested to investigate their performance in the F-TS reaction and attrition resistance tests.

References

Abebe, B. and Murthy, H.C.A. 2018. Iron oxide Nanomaterial: Synthesis, Characterization and Lead Removal. *Journal of Encapsulation and Adsorption Sciences*, 8 (04):195-209.

Ali, A., Zhang, N. and Santos, R. M. 2023. Mineral characterization using scanning electron microscopy (SEM): a review of the fundamentals, advancements, and research directions. *Applied Sciences*, 13(23), 12600.

Claeys, M., van Steen, E., Botha, T., Crous, R., Ferreira, A., Harilal., A., Moodley, D.J., Moodley, P., du Plessis, E. and Visage, K. 2021. Oxidation of Hägg carbide during high temperature Fischer-Tropsch Synthesis: Size-dependent. *American Chemical Society Catalysis*, 22 (11):13866–13879.

Deng, F., Luo, X., Li, K., Tu, X., Luo, S., Yang, L., Zhou, N. and Shu, H. 2013. The effect of vinyl-containing ionic liquid on the photocatalytic activity of iron-doped TiO_2, *Journal of Molecular Catalysis A*: *Chemical*, 366: 222-227.

Das, D. and Langrish, T. A. 2012. Combined crystallization and drying in a pilot-scale spray dryer. *Drying Technology*, 30(9):998-1007.

Ge, W., Gao, W., Zhu, J. and Li, Y. 2019. In situ synthesis of Hägg iron carbide (Fe_5C_2) nanoparticles with a high coercivity and saturation magnetization. *Journal of Alloys and Compounds*, 781: 1069-1073.

Guduru, R.K. and Mohanty, P.S. 2012. Corrosion of Metal–Oxide Systems. In *Corrosion Resistance*, 23:66-68.

Han, Z., Qian, W., Ma, H., Zhang, H., Sun, Q. and Ying, W. 2019. Effects of Sm on Fe-Mn catalysts for Fischer-Tropsch synthesis. *Royal Society of Chemistry advances,* 9 (55): 32240-32246.

Housaindokht, M.R. and Pour, A. N. 2012. Study the effect of HLB of surfactant on particle size distribution of hematite nanoparticles prepared via the reverse microemulsion. *Solid State Sciences,* 14:622-625.

Lassoued, A., Dkhil, B., Gadri, A. and Ammar, S. 2017. Control of the shape and size of iron oxide nanoparticles synthesized through the chemical precipitation method. *Results in Physics*, 7: 3007-3015.

Milburn, D. R., Chary, K. V. and Davis, B. H. 1996. Promoted iron Fischer-Tropsch catalysts: characterization by nitrogen sorption. *Applied Catalysis A: General*, 144:121-132.

Motchelaho, A.M.M., 2011. Iron and cobalt catalysts supported on carbon nanotubes for use in the fischer-tropsch synthesis. PhD Thesis. University of Witwatersrand, Johannesburg.

Nandiyanto, A. B. D., Zaen, R. and Oktiani, R. 2020. Correlation between crystallite size and photocatalytic performance of micrometer-sized monoclinic WO_3 particles. *Arabian Journal of Chemistry*, 13(1): 1283-1296.

Ouyang, W., Chen, E.C. and Wu, T.M. 2015.Thermal Stability and Magnetic Properties of Polyvinylidene Fluoride/Magnetite Nanocomposites, *Materials*, 8: 4553-4564.

Okwonna O, O., Otaraku I, J. and Oduola K, M. 2019. Prediction of the Catalyst Attrition Rate in an Industrial Fluid Catalytic Cracking Operation. *World Journal of Innovative Research*, 7:08-15.

Tavares, M., Westphalen, G., Araujo Ribeiro de Almeida, J.M., Romano, P.N. and Sousa-Aguiar, E.F. 2022. Modified Fischer-Tropsch Synthesis: A review of highly selective catalysts for yielding olefins and higher hydrocarbons. *Fronties in Nanotechnology*, 4: 978358.

Wang, C.G. 2023. A systematic theoretical study the active sites of potassium promoter on the activity of water-gas shift reaction over Pt (111). *Applied Surface Science*, 611: 155638.

Wang, Z., Skiles, S., Yang, F., Yan, Z. and Goodman, D.W. 2012. Particle size effects in Fischer–Tropsch Synthesis by cobalt. *Catalysis Today*, 181(1): 75–81.

Wen, R., Thiessen, J. and Jess, A. 2022. Catalytic behavior and in situ X-ray Diffraction of promoted iron catalysts for Fischer-Tropsch Synthesis. *Chemical Engineering and Technology,* 94 (11): 1756-1764.

Appendix

GC Information

Table 5.1: Parameters of the GC used

On-line GC	Agilent
Detector 1	FID
Column 1	Agilent CP7770 CP-Sil 5 CB
Dimensions	50 m x 320 µm x 1.2 µm
Temperature	350°C
Mode	Spitless
Carrier gas	He
Sample valve temperature	250°C
Initial Flow rate: 2 mL/min	2 mL/min
Pressure	14.177psi
Flow rate before run	4.2892 mL/min
Average Velocity	29.256 cm/sec
Product analysis	C1-C9
Detector 2	TCD
Column 2	Agilent CP7355 Pora BOND Q
Dimensions	50 m x 530 µm x 10 µm
	320°C
Mode	Spitless
Carrier gas	He
Sample valve temperature	250°C
Initial Flow rate	19.475 mL/min
Pressure	18.778 psi

Flow rate before run	4.2892 mL/min
Average Velocity	98.464 cm/sec
Product analysis	N_2, CO, CO_2 and H_2

Table 5.2: Summary of the compounds analyzed by the online GC

Compounds	**Tr: retention time (min)**
Ethene	3.461
Ethane	3.898
Propene	6.301
Propane	6.568
1-butene	8.365
Butane	8.942
Methane	10.846
H_2	10.04
CO_2	2.923
CO	11.065
N_2	10.416

The calculations below show how the quantity of the products was calculated.

$$n(i) = f(i)/N_2 \times \frac{A(i)_{GC-TCD}}{A(N2)_{GC-TCD}} \times n(N_2) \qquad \text{Equation 5.1}$$

$f(i)/N_2$ = compound specific response factor obtained by regular calibration

A (i) GC-TCD= Area of in GC-TCD trace for compound i

$n.(N_2)$ = molar flow rate of diluent N_2

The flow of volatile organic products was determined from the analysis of organic products compounds in the reactor effluent (using a GC-FID) and a molar flow rate of methane as a tie-compound.

$n(i) = f(i)\,FID \times \frac{A(i)_{GC-FID}}{A(CH4)_{GC-FID}} \times n(CH_4)$ Equation 5.2

f (i) FID = compound of specific response factor for compound I in an FID

A (i) GC-FID= Area of in GC-FID trace for compound i

$n(CH_4)$ = molar flow rate of tie-component CH_4 as determined using GC-TCD

The selectivity of F-TS products was determined using the FID (with methane as the tie component using integrated peak areas (Ai) according to the following equation).

$S_{C5+} = (1 - (\frac{AC1+AC2+AC3+AC4}{ACH4}).\ S_{CH4}).100$ C-%

Equation 2.13

Where S_{CH4}= selectivity towards CH_4 as defined above (C-%)

A_{C1}= integrated peak area of carbon number 1 etc.

S_{C5+}= carbon selectivity towards all hydrocarbon chains with 5 or more carbons (C-%)

$\text{Selectivity (i) (\%)} = \frac{niNi}{NCO,in - NCO,out} \times 100\%$ Equation 5.3

niNi= n, is the number of carbon atoms, N is the number of moles and i is the product i^{th}.

N CO, in = inlet flow of CO to the reactor

N CO, out = outlet flow of CO to the reactor

The percentage conversion of carbon monoxide was determined according to the following equation:

$\text{Conversion (CO)} = \frac{NCO,in - NCO,out}{NCO,in} \times 100\%$ Equation 5.4

n CO, in = inlet flow of CO to the reactor

n CO, out = outlet flow of CO to the reactor